Dynamical Structure and Evolution of Merger Remnants

Athanasia Tsatsi
Max-Planck-Institut für Astronomie

Heidelberg 2016

Dissertation in Astronomy
submitted to the
Combined Faculties of the Natural Sciences and Mathematics
of the Ruperto-Carola-University of Heidelberg, Germany,
for the degree of
Doctor of Natural Sciences

Put forward by
Athanasia Tsatsi
born in Athens, Greece

Oral examination: 21.12.2016

Dynamical Structure and Evolution of Merger Remnants

Athanasia Tsatsi
Max-Planck-Institut für Astronomie

Referees: Dr. Glenn van de Ven
Dr. Hubert Klahr

To my big sisters

Abstract

From the most massive stellar systems known to be the end products of mergers, such as early-type galaxies, to the less massive ones, such as nuclear star clusters, the recent improvements of integral-field-unit (IFU) spectroscopic surveys have revealed that their stellar dynamics are much more complex than previously thought. These new insights are expected to reflect the complex assembly and evolutionary processes that create them and are now pointing to the need for more realistic scenarios for their formation.

In the first part of this thesis, we study the connection between the present-day dynamical structure and the formation history of merger remnant early-type galaxies, by using mock observations extracted from merger simulations. We find that major mergers can account for the peculiar kinematic features that are often observed in early-type galaxies, such as kinematically decoupled cores, or prolate (long-axis) rotation. We find a new channel for the formation of kinematically decoupled cores, that can help towards explaining their observed prevalence in IFU surveys. Additionally, we present the discovery of prolate rotation in nine early-type galaxies from the CALIFA IFU Survey, adding a significant fraction to the observed cases of such galaxies that exist so far in the literature. We show that prolate rotators can be the end-products of major mergers.

In the second part, we address the role of mergers in the formation of Nuclear Star Clusters (NSCs), using simulations of consecutive infalls of globular clusters into the center of a galaxy. We find that NSCs resulting from this process show both morphological and kinematic properties that match the Milky Way NSC very well, including significant stellar rotation – a fact that has been attributed to gas infall so far.

In general, our results demonstrate that mergers can account for a variety of observed kinematic features in both early-type galaxies and NSCs and place constraints on the role of mergers in their complex assembly history.

Zusammenfassung

Die jüngsten Verbesserungen spektroskopischer Surveys mittels integraler Feldeinheiten (integral-field-units, IFU) haben enthüllt, dass die Dynamik der massivsten Sternsysteme, die als Endprodukt von Mergern bekannt sind, wie elliptische Galaxien, bis hin zu weniger massiven, wie den Kernsternhaufen (Nuclear star cluster, NSC), komplexer ist als bisher angenommen. Diese neuen Einsichten legen nahe, dass auch die Zusammensetzung und die Entwicklungsprozesse dieser Systeme komplex sind und verdeutlichen die Notwendigkeit für realisistischere Szenarien ihrer Bildung.
Im ersten Teil dieser Dissertation studieren wir die Verbindung zwischen den heutigen dynamischen Strukturen und der Entstehungsgeschichte von elliptischen Galaxien als Überreste von Mergern anhand von synthetischen Beobachtungen, die aus Simulationen kollidierender Galaxien erstellt werden. Wir stellen fest, dass massive Kollisionen für die speziellen kinematischen Eigenheiten, welche oft in elliptischen Galaxien beobachtetet werden, verantwortlich sind, wie beispielsweise den kinematisch entkoppelten Kernen oder entlang der Längsache gestreckte Rotation. Wir finden einen neuen Weg für die Entstehnung von kinematisch entkoppelten Kernen, die bei der Erklärung ihres Vorherrschens in IFU Surveys helfen können. Zusätzlich präsentieren wir die Entdeckung von gestreckten Rotationen in neun der elliptischen Galaxien des CALIFA IFU Surveys, welche einen signifikanten Anteil zu den bisher in der Literatur bekannten Fällen solcher Galaxien hinzufügt. Wir zeigen ebenso, dass gestreckte Rotationen das Endprodukt von massereichen Mergern sein können.
Im zweiten Teil besprechen wir die Rolle von Mergern bei der Entstehnung von NSCs anhand von Simulationen von aufeinanderfolgenden Einfällen von Kugelsternhaufen in das Zentrum einer Galaxie. Wir finden, dass NSCs, die in solchen Prozessen entstehen, sowohl morphologische als auch kinematische Eigenschaften aufweisen, die dem des Kernsternhaufens im Zentrum der Milchstraße sehr gut entsprechen, insbesondere auch der signifikanten Sternrotation - einem Fakt, der bisher dem Gaseinfall zugesprochen wurde.
Unsere Ergebnisse zeigen somit, dass Merger für eine Vielzahl von beobachteten kinematischen Besonderheiten sowohl in elliptischen Galaxien als auch in NSCs verantwortlich sind und präzisieren die Rolle von Mergern in ihren komplexen Entstehungsgeschichten.

Contents

Chapter 1

Introduction

One of the fundamental challenges in modern astrophysics is the understanding of the processes governing galaxy formation and evolution, both on large and small scales. From dwarfs, containing up to 10^9 stars, to giants of 10^{13} stars, galaxies show a wide range of masses, sizes, as well as morphological and dynamical properties. The most conspicuous characterization of a galaxy is based on its morphology. Galaxies can show complex morphological characteristics, such as spiral arms, coexisting with a stellar disk and central spheroidal (bulge) concentration [spiral galaxies], or even a bar-shaped central stellar component [barred spirals]. In other cases they contain a stellar disk with a dominant bulge component but without signs of spiral arms [lenticular galaxies], or even show an irregular and asymmetric morphology with no disk or bulge [irregular/peculiar galaxies]. Galaxies may also appear to have a simple, symmetric and featureless morphology of elliptical shape. Such systems characterized by a "regular" morphology are known as elliptical galaxies.

Which physical processes account for this diversity of galaxy shapes and morphologies? While addressing this issue, the simplistic assumption that a regular apparent morphology of a stellar system is equivalent to a simple dynamical structure was for long adopted. Recent observational developments have however changed this picture, as complex dynamical structures have been found to hide behind the shapes of simple systems.

Early-type galaxies (ETGs: ellipticals and lenticulars) are such an example, with their smooth and featureless morphology that was only recently proven to be associated with an unprecedented complex dynamical structure. This has led to a renewed interest on their formation and on the origin of this intricacy.

Even on smaller scales, galaxies may host systems whose origin and properties are still debated. Nuclear star clusters (NSCs) are one class of this kind of objects. NSCs are very massive and compact star clusters, whose detection in the centers of an increasing amount of galaxies of all morphological types has been allowed by recent observational advancements. These objects are especially interesting because their formation and evolution appears to be tightly connected to that of their host galaxy.

In parallel to observational advancements, the rapid progress of numerical simulations has brought new insights to our knowledge of galaxy formation and evolution. ETGs are now thought to be the end-products of an hierarchical galaxy merger process. NSCs may also be the remnants of mergers of globular clusters that infall to the center of a galaxy. There is little doubt that mergers occur,

however whether and how they can produce merger remnants that agree with observations is still an open question.

In this thesis we seek to address one fundamental question: *How does a merger origin reflect on the dynamical structure and evolution of a merger remnant?* In other words: in large stellar systems, such as early-type galaxies, or on smaller galactic scales, such as for nuclear star clusters, how can their merger origin explain their present-day, often complex and peculiar, dynamical structure? More specifically, we wish to address the following open questions:

1. Complex dynamical structures in early-type galaxies may be reflected in stellar motions in their central regions that appear kinematically decoupled from the motion of their main stellar body (kinematically decoupled components). Why are these features so commonly observed in ETGs? Are they the end-products of mergers, and if so, what are the physical processes that lead to their creation? ***(Chapter 2)***

2. ETGs feign the appearance of an oblate ellipsoid, but their shape could as well be triaxial. If so, they may show stellar motion around their major photometric axis (prolate rotation). If prolate rotation is theoretically permitted and predicted for ETGs, why is such a feature so rarely observed? How can mergers account for the formation of prolate rotating ETGs? ***(Chapter 3)***

3. On smaller scales, how realistic is a merger origin of nuclear star clusters? Can globular cluster mergers produce remnants that resemble the observed dynamics of nuclear star clusters? What are the dynamical fossil records of such a formation scenario? ***(Chapter 4)***

In what follows, we provide a brief summary of the current observational and theoretical knowledge on the present-day structure, the formation and evolution of the two types of stellar systems of interest, early-type galaxies and nuclear star clusters. We focus mainly on their stellar dynamics, and use this as our viewpoint to address open questions regarding their formation and possible merger origin.

1.1 Dynamical Structure and Formation of Early-type Galaxies

1.1.1 Morphological properties of Early-type Galaxies

In the traditional picture, elliptical galaxies (Es) are smooth, roundish and dynamically "simple" stellar systems, that contain a single and old stellar population, no gas or dust, no obvious signs of spiral arms in their optical images and no rotation. In what follows, we discuss how this picture has changed over the last decade, especially from a dynamical point of view, since the introduction of Integral Field Spectroscopy (IFS) that has allowed for observations of the two-dimensional stellar kinematics of elliptical galaxies.

Classifications: Depending on their luminosity, elliptical galaxies range from the giant, very massive and spatially extended *cD galaxies* of absolute B magnitudes $M_B \sim -22$ to -25, stellar masses of $10^{13} - 10^{14}\,M_\odot$, to *dwarf ellipticals*, with $M_B \sim -13$ to -19 and stellar masses of $10^7 - 10^9\,M_\odot$. Giant ellipticals are rather rare, but are most commonly found near the centers of dense galaxy clusters, where they usually comprise the Brightest Cluster Galaxies (BCGs). Ellipticals of intermediate luminosities are called *normal ellipticals*, with $M_B \sim -15$ to -23 and masses between $10^8 - 10^{13}\,M_\odot$.

Ellipticals appear to share many of their observed properties with lenticular galaxies (S0s). Both Es and S0s compose a broader classification of galaxies, the ***early-type galaxies (ETGs)***, which is the term adopted throughout this thesis.

Spirals (also referred to as "disk galaxies") and irregular galaxies make up the late-type galaxies (LTGs), according to the widely known Hubble (1936) classification system of galaxies and its revisions (de Vaucouleurs 1959; Sandage 1961)[1].

Sizes: Early-type galaxies show a wide variety of observed sizes. Since galaxies are systems that do not possess clearly defined boundaries, the most commonly adopted parameter to quantify their size is the *effective radius*, r_e, which is the projected radius which contains half of the total galaxy light. Effective radii range from ∼20 to 30 kpc for cD galaxies to hundreds of pc for the smallest dwarf ellipticals.

Luminosity profiles: The profiles of most elliptical galaxies can be well described by the Sersic (1968) profile:

$$I(r) = I(r_e) exp\left(-b(n)\left(\frac{r}{r_e}\right)^{1/n} - 1\right), \tag{1.1}$$

where n is the Sersic index, r_e is the effective radius and b(n)∼2n - 0.327. The Sersic index n increases with increasing total galaxy luminosity (e.g. D'Onofrio et al. 1994; Graham & Guzmán 2003) and correlates with the central light concentration of the galaxy $C_{r_e}(\alpha)$, which is the ratio between the flux

[1] An interesting note about this nomenclature is that it is, until now, widely believed that Hubble (1936) used this to propose an evolutionary stage from early to late types– this does not seem to be true. Quoting Hubble (1927): *"The nomenclature, it is emphasized, refers to position in the sequence [...] The entire classification is purely empirical and without prejudice to theories of evolution"*.

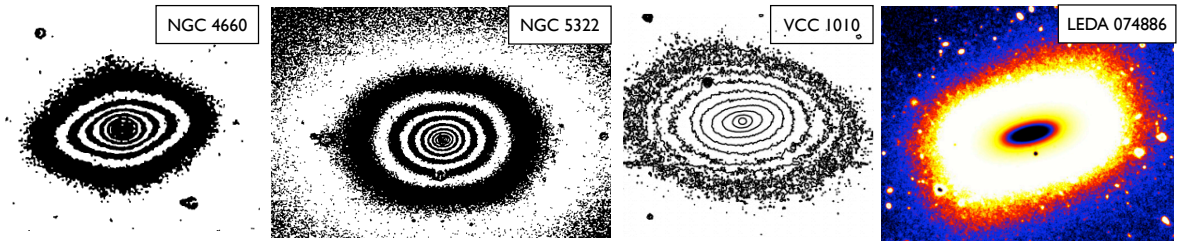

Figure 1.1: Examples of isophotal features observed in ETGs. *From left to right:* The disky isophotes of NGC 4660, the boxy isophotes of NGC 5322 (adapted from Bender et al. 1988), and the isophotal twist of VCC 1010 (adapted from Ryden et al. 1999) and the change of isophotes of LEDA 074886 from disky to boxy with increasing radius (adapted from Graham et al. 2012).

within r_e and the flux within αr_e (α<1) (Trujillo et al. 2001).

In fact, the outer parts of giant normal ellipticals (M_b <-21) can be well described by a Sersic function with n≥4 (e.g. Caon et al. 1993), while less massive normal ellipticals (M_b >-21) have Sersic profiles with n≤3 (e.g. Graham & Guzmán 2003). Dwarf ellipticals show typically Sersic indices of n∼1 (e.g. Binggeli & Jerjen 1998).

Nuclear profiles: At parsec scales, the central regions of some elliptical galaxies show clear breaks in their surface brightness profiles, with a steep outer profile followed by a shallower inner one (*"core galaxies"*), while others show a gradually changing slope towards the center (*"power-law galaxies"*, Ferrarese et al. 1994; Lauer et al. 1995). A number of studies have shown that the slope of the nuclear regions of ETGs seem to correlate with global galaxy properties (e.g. Ferrarese et al. 2006) – for example, giant ellipticals typically have cores, while more faint ellipticals are coreless (Faber et al. 1997).

Isophotal shapes: This apparent morphological dichotomy between elliptical galaxies was also supported by studies of their isophotal shapes, which have revealed that the isophotes of many ETGs are non-elliptical (e.g. Carter 1979). Brighter ellipticals can have more *"boxy"* isophotal shapes, and less bright ones show *"disky"* (or "pointed") isophotes (see Figure 1.1, Bender et al. 1988), suggesting for the latter the existence of embedded stellar disks (e.g. Jedrzejewski 1987a; Rix & White 1990). This was supported by the fact that disky ellipticals appeared to rotate faster than boxy ones (Bender 1988) – implying that the apparent morphological dichotomy corresponds to a *kinematic dichotomy* as well.
The "boxiness" or "diskiness", as well as the position angles of the major-axis of their isophotes can show a significant variation with increasing radius (Jedrzejewski 1987b). The latter is commonly referred to as *"isophotal twists"*. Figure 1.1 shows some typical examples of boxy and disky isophotes, as well as isophote shape and position angle variations observed in ETGs.

Intrinsic shapes: It was for long thought that the three-dimensional shape of elliptical galaxies is *oblate*: resembling an ellipsoid where two of its principal axes are of equal length (Figure 1.2). Contopoulos (1956) suggested that the intrinsic shape of elliptical galaxies could be in general, *triaxial*.

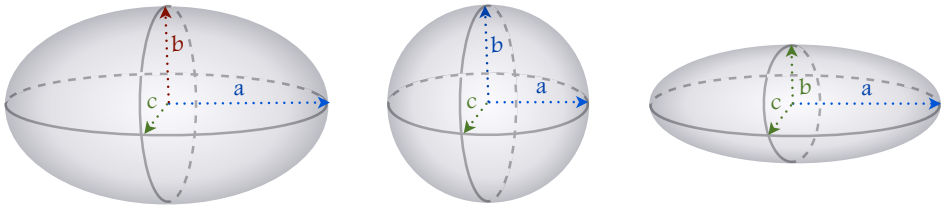

Figure 1.2: Intrinsic shapes of ETGs. *From left to right:* A generic triaxial ellipsoid with principal semi-axes a>b>c, an axisymmetric oblate ellipsoid with a=b>c (face-on view) and an axisymmetric prolate ellipsoid with a>b=c (side-on view).

Since then it has been established that triaxial stellar systems are, theoretically, dynamically stable configurations (e.g. Aarseth & Binney 1978; Binney 1985). The existence of isophotal twists in some ETGs was the first evidence that they might not be oblate, but in general, triaxial or even *prolate* ellipsoids (King 1978; Binney 1978).

1.1.2 Dynamical Structure of Early-type Galaxies in the IFS Era

More insightful evidence about the intrinsic structure of ETGs can be found by studies of their stellar kinematics. In the traditional picture, ETGs are round and simple stellar systems, that show no rotation and are dynamically supported by the random motions of their stars. Over the last decade, the major instrumental advancement of **Integral-Field-Spectroscopy (IFS)** has brought rapid changes to this past picture, mainly with the findings from large IFS Surveys such as SAURON (Bacon et al. 2001), ATLAS^{3D} (Cappellari et al. 2011), and CALIFA (Sánchez et al. 2012).

With IFS one can study the spectrum of a galaxy as a function of position, by using Integral Field Units (IFU) and obtaining simultaneously spectra in a two-dimensional field. The signal from each pixel of the field is fed into a spectrograph, which generates a spectrum for each individual pixel. All the spectra are arranged into a datacube which contains the entire 2D field of view plus the third dimension drawn from the spectrograph, allowing us to retrieve 2D spectroscopic information for a galaxy.

The spectra of ETGs show absorption features similar to those of late-type giant stars, which typically dominate the light of the old stellar population of the galaxy. These features are shifted and broadened as a result of the motion of the galaxy's stars. Typically, by convolving the spectrum of a template star with a Gaussian *line-of-sight velocity distribution (LOSVD)*, one can match very well the observed spectrum of an elliptical galaxy. The mean of the Gaussian yields the mean stellar line-of-sight (LOS) velocity, and the dispersion of the Gaussian yields the spread of the observed velocities.

In general, the LOSVDs of ETGs are not perfectly Gaussian and are usually parametrized with the Gauss-Hermite series (van der Marel & Franx 1993):

$$L(\upsilon) = \frac{\alpha(w)}{\sigma}\left[1 + \sum_{j=3}^{N} h_j H_j(w)\right], \tag{1.2}$$

with

$$w = \frac{\upsilon - V}{\sigma}, \qquad \alpha(w) = \frac{1}{\sqrt{2\pi}} e^{-w^2/2}, \tag{1.3}$$

where υ is the LOS velocity and V and σ the mean and the dispersion of the best-fit Gaussian. H_j is a set of Hermite polynomials of degree j, and h_j are the *Gauss-Hermite moments*, which for j>2 measure deviations from the best-fit Gaussian. In particular, h_3 and h_4 parametrize the *skewness* and the *kurtosis*, respectively, of the LOSVD.

In the traditional picture provided mainly by long-slit spectroscopy, an ETG shows a small amount of stellar rotation V relative to its systemic velocity, a high and centrally peaked velocity dispersion σ that declines on either side of the center and very low higher-order moments h_3 and h_4, meaning that their LOSVDs are very close to Gaussian – thus often referred to as, "simple systems".

This past picture has changed drastically over the last few years, as the first generation of IFS Surveys have been able to provide full two-dimensional observations of the stellar kinematics for significantly large samples of ETGs. These findings have now established that the dynamical structure of ETGs is not simple but rather complex. Many ETGs were found to exhibit significant amount of stellar rotation (with velocity amplitudes even reaching the typical ones of spiral galaxies), others showed no rotation and even complex kinematic peculiarities.

Kinematic dichotomy: A new kinematic classification was then established, according to which ETGs appear in two broad types (flavours): the *"fast"* or *"slow" rotators*, depending on whether they exhibit a large-scale rotation or not (Emsellem et al. 2007, 2011). Fast and slow rotators are defined according to their λ_R parameter (Emsellem et al. 2007):

$$\lambda_R = \frac{\langle R\,|V|\rangle}{\left\langle R\sqrt{V^2 + \sigma^2}\right\rangle}, \tag{1.4}$$

which is a proxy for the stellar angular momentum of the galaxy as a function of its radius R from the center. Fast and slow rotators are defined as having λ_R values above or below $\kappa \times \sqrt{\epsilon}$, respectively, where ϵ is the apparent ellipticity of the galaxy within the specified radius and κ=0.31 for measurements made within an effective radius R_e (see Figure 1.3, Emsellem et al. 2011).

Slow rotators are found to be common amongst the most massive ellipticals, and are generally classified as Es from photometry alone. Fast rotators are generally less massive and are classified either as Es or S0s. In this kinematic classification, the morphological distinction between Es and S0s is not relevant: many ETGs classified as Es from photometry, were found to show embedded stellar disks in their kinematics – thus showing kinematics similar to the ones observed in S0s and classified as fast rotators. In general, fast rotators may show typically disky isophotes, while slow rotators may exhibit cores and boxy isophotes.

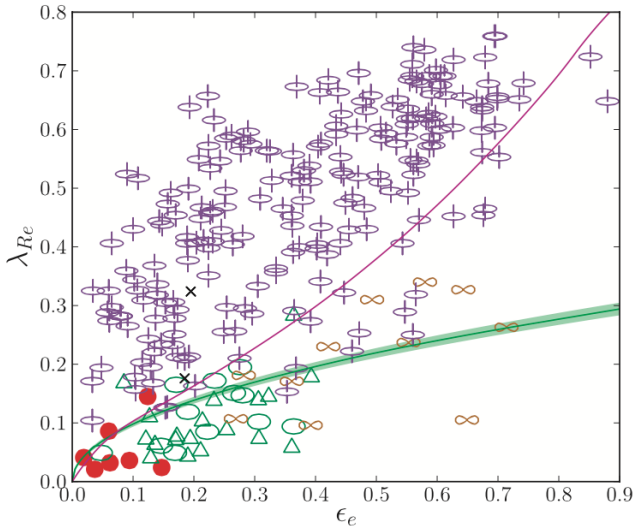

Figure 1.3: The kinematic dichotomy between ETGs. Measured λ_{R_e} values versus the ellipticity ϵ_e within an aperture of 1Re for 260 ETGs from the IFS Survey ATLAS^{3D}. The solid green line is $0.31 \times \sqrt{\epsilon}$ and shows the separation between fast and slow rotators. The solid magenta line corresponds to ETGs with anisotropy β=0.65ϵ within R_e (see Cappellari et al. 2007; Emsellem et al. 2011 for more details). Red circles are for non-rotators, green ellipses are for non-regular rotators without any specific kinematic feature, green triangles are for galaxies with KDCs, orange lemniscates are for 2-σ galaxies (galaxies with two counter-rotating flattened stellar components), purple symbols are for regular rotators and black crosses are for two galaxies which could not be classified. Adapted from Emsellem et al. 2011.

Kinematic peculiarities: ETGs may also be classified as *"regular or non-regular rotators"*, depending on whether the two-dimensional map of their stellar velocity is dominated by ordered rotation or by non-ordered and complex structures (Krajnović et al. 2011).

Very often, the inner regions of such non-regular rotating ETGs may counter-rotate or in general, show a distinct and decoupled sense of rotation with respect to the main body of the galaxy. Such features are known as *Kinematically Decoupled Components (or Cores)* (KDCs) and may range in sizes from a few hundred pc to a few kpc (McDermid et al. 2006). KDCs were first discovered using one-dimensional long-slit spectroscopic observations of ETGs (e.g. Efstathiou et al. 1982; Bender 1988; Franx & Illingworth 1988). Until recent years, ETGs with such kinematic peculiarities were considered rather rare. IFS surveys, being able to provide full two-dimensional observations of stellar kinematics, have favoured their detection in ETGs. Especially in slow rotators, these studies revealed an unprecedented fraction of KDCs and other kinematic peculiarities in their central stellar regions.

As a result of the existence of central counter-rotating components, some ETGs do not show a single central peak in their velocity dispersion σ profiles, but double peaks (*"2-σ galaxies"*, Krajnović et al. 2011). Most interestingly, in massive ETG IFS Surveys, KDC-host galaxies are typically the most massive ones and are very common among slow rotators (see Figure 1.3). Nevertheless, IFS observational advancements favored the discovery of KDCs in many more early-type systems over the last few years, in massive as well as in dwarf ellipticals (e.g. Toloba et al. 2014). These observations

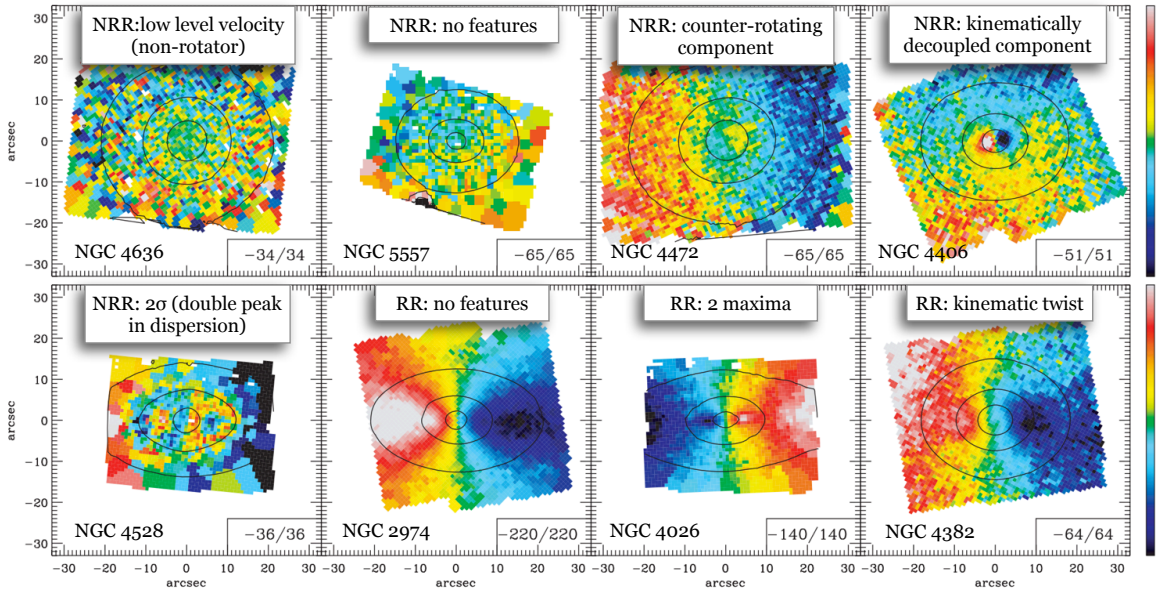

Figure 1.4: Example of the typical kinematic features found in the ATLAS^{3D} early-type galaxies for non-regular rotators (NRR) and regular rotators (RR). Values in the bottom right denote the plotted velocities in km·s^{-1}. Adapted from Krajnović et al. (2011).

led to a strong interest about the formation and evolution of KDCs and their host galaxies. This topic is addressed in more detail in *Chapter 2*.

Very often, ETGs are found to exhibit misalignments between the minor photometric and their kinematic axis. Such *kinematic misalignments* may also vary as a function of radius (*kinematic twists*). Figure 1.4 shows typical examples of the various kinematic features found in ETGs from the ATLAS^{3D} Survey (Krajnović et al. 2011).

Orbital structure: In order to understand how kinematic peculiarities and misalignments might arise, one may regard a galaxy as a composition of *orbits* rather than stars. The orbital structure of an elliptical galaxy depends crucially on the assumed shape of its gravitational potential. In general, a triaxial ellipsoid can support 4 main types of stable orbits: (i) *box orbits*, that have no sense of rotation, (ii) *short-axis tube orbits*, that rotate about the short axis, (iii) *inner long-axis tube orbits* and (iv) *outer long-axis tube orbits*, that rotate around the long axis (see Figure 1.5). There are no stable orbits rotating about the intermediate axis. Box orbits pass arbitrarily close to the center of the galaxy and are responsible for the "boxiness" of the isophotes. Tube orbits tend to avoid the center and are called "centrophobic" orbits, but carry the net angular momentum observed in the galaxy.

In an oblate galaxy, short-axis tube orbits are the only type of stable stellar rotation, thus its net spin vector is expected to be aligned with its minor axis (no misalignment between kinematics and photometry). A triaxial galaxy, on the other hand, supports two types of stable stellar rotation – these two types are supported by the short-axis and long-axis tube orbits, respectively. It is therefore

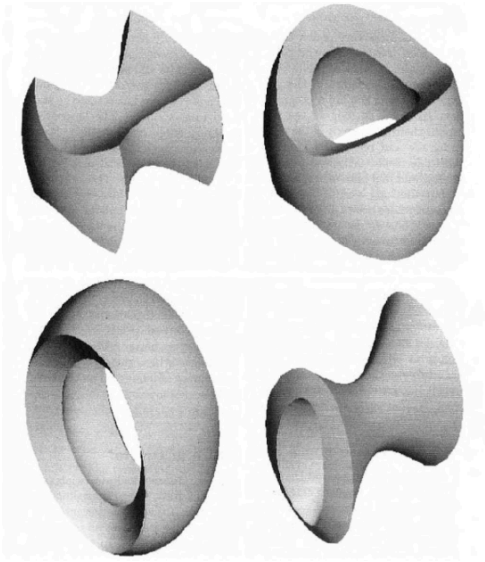

Figure 1.5: The main types of stable orbits in a (static) triaxial potential. Clockwise from top left: box orbit, short-axis tube, inner long-axis tube and outer long-axis tube. Adapted from Statler (1987).

expected that the net spin vector of a triaxial galaxy should lie somewhere between its short and long axis, resulting in observed misalignments between photometry and kinematics. Therefore, kinematic misalignments and twists in elliptical galaxies are considered signatures of *triaxiality* (Contopoulos 1956; Binney 1985). Since the orbital theory predicts that stellar motion around the long axis is stable in a triaxial system, much work has been done to search for elliptical galaxies that show such rotation ("*prolate rotation*") in their main stellar body, however most of such studies have been unsuccessful in the past (e.g. Bertola et al. 1988). Until now, only a few observations of such galaxies are available, while their formation origin is not yet clear. New observational findings and clues that could hint to the formation of such systems are presented in *Chapter 3*.

Fast rotators typically show no misalignment between their kinematic and minor photometric axis and are consistent with being nearly oblate. Kinematic misalignments are more commonly found in the more massive slow rotators, suggesting that they are weakly triaxial (Krajnović et al. 2011).

Environment: This dichotomy between fast and slow rotating ETGs seems to be reflected in their kinematics, morphology, intrinsic shapes as well as their environment: slow rotators are commonly found near the centers of groups or clusters, while fast rotators follow a similar spatial distribution as spiral galaxies within a cluster (D'Eugenio et al. 2013; Cappellari et al. 2011; Houghton et al. 2013; Scott et al. 2014; Fogarty et al. 2014). Slow rotators are very rarely found in the field. This yields a kinematic morphology–density relation (Cappellari et al. 2011), according to which, the fraction of spiral galaxies to gradually decreases with environmental density while the fraction of ETGs correspondingly increases, with slow rotators increasing more rapidly in higher densities than fast rotators. All this evidence suggests that fast and slow rotators correspond to two different galaxy families that may result from different formation and evolution pathways. Especially for slow rotators, their origin

and evolution may be more closely linked to the formation and evolution of their surrounding galaxy clusters.

This morphological and kinematical segregation of ETGs has produced very lively debates over the last few years: *How do fast and slow rotators form? What is the origin of their complex dynamics and kinematic peculiarities?* In what follows, we will give a brief overview of the current paradigm for the formation of ETGs, driven mainly by the IFS observations of their stellar kinematics described above.

1.1.3 Formation of Early-type Galaxies

About 40 years ago, two main scenarios were suggested for the formation of early-type galaxies:

1. The *monolithic collapse scenario*, according to which the stellar content of the galaxy forms from a single collapsing gas cloud that experiences a short and global burst of star formation at high redshift from uncollapsed initial conditions, followed by a passive evolution until the present day (Partridge & Peebles 1967; Larson 1974).
2. The *hierarchical merger scenario*, according to which most of the stars of the galaxy form initially in two or more pre-existing galaxies (progenitors), that subsequently merge to form the final elliptical galaxy (Toomre & Toomre 1972; Toomre 1977).

The monolithic collapse scenario was suggested in order to explain the uniformly old stellar populations observed in elliptical galaxies. One of the main problems of this narrative is the assumption of the passive evolution of ellipticals since the time of their collapse. This must have happened ∼10 Gyr ago (z>2), as is the mean age of the stellar populations found in most normal ellipticals. A series of studies have shown, however, that the evolution of ETGs has not been passive since then, since their number density evolves with redshift (Bell et al. 2004; Faber et al. 2007). Another evidence against the monolithic collapse scenario is the evolution of the sizes of ETGs with redshift (e.g. Zirm et al. 2007; van Dokkum et al. 2008, 2010; van der Wel et al. 2014). For example, van Dokkum et al. (2010) report an increase in stellar mass of massive elliptical galaxies by a factor of ∼2 since z∼2, which is accompanied by a growth in size. Additionally, van der Wel et al. (2014) found that small and compact early-type galaxies are common at z∼2 and do not exist in equal numbers today. Such results are not consistent with the passive evolution assumed by a monolithic collapse scenario since z∼2 and favors growth by mergers.

The merger scenario was suggested as an alternative to the monolithic collapse scenario originally in the seminal work of Toomre & Toomre (1972), where the hypothesis of the formation of an elliptical galaxy through the merger of two disk galaxies was first introduced. The merger hypothesis seems, until today, the most promising picture for the formation of elliptical galaxies. Direct evidence of a recent merger event can be found in many cases of ETGs that may feign a regular and smooth appearance, but in deep images show a disturbed morphology, or shells, ripples, tidal tails and other fine structures (see for example Figure 1.6).

Figure 1.6: Deep images of ETGs with morphological signatures of a recent major merger: inner dust lanes, strongly perturbed morphology and tidal tails. *From left to right:* NGC 5557, NGC 1222, NGC 2764. These galaxies feign a more regular morphology in less deep images. Adapted from Duc et al. (2015).

A galaxy merger can be characterized by a wide variety of "merger parameters", that include intrinsic properties of the participating galaxies (progenitors), such as their relative masses (mass ratio), their sizes, their stellar and dark matter halo properties, as well as the existence or lack of gas, characterizing a merger as "wet" (gas-rich) or "dry" (gas-poor), respectively. A *major merger* corresponds typically to a stellar mass ratio of 1:1 to 1:3 between progenitors, and a *minor merger* to a ratio less than 1:3[2]. Merger parameters also include the initial orbital configurations of the progenitors, such as their relative velocities and initial separation, and the orientation of their orbital plane, with respect to their intrinsic rotation axes. A *prograde merger (p)* corresponds to a merger where the rotation axes of the two galaxies coincide, while in a *retrograde merger (r)*, they are opposite. There are 4 different types of combinations between the three rotation vectors of the two merging galaxies and their orbital plane, hence 4 types of merger orientations: ppp (progenitors spin and orbital spin coincide), ppr and prp (one of the progenitors is retrograde), and rpp (both progenitors are retrograde with respect to their orbital spin). Assuming that a merger between two identical disk galaxies has no preferred orientation in a cosmological framework (Khochfar & Burkert 2006a), then each of the above 4 types of mergers has a 25% probability to happen.

What are the implications of a merger origin on the dynamical structure of an early-type galaxy? To be able to properly address this question one needs to make use of numerical simulations as a primary tool for understanding the physical processes that govern a merger – especially because these processes are proven hard to be quantified analytically, due to the dynamical complexity of the systems involved.

The vast progress of numerical simulations has improved significantly our understanding on how the merger scenario can account for the observed dynamical properties of present-day ETGs. Due to the strong gravitational interaction and associated violent relaxation, it was shown that a major merger between two equal-mass disk galaxies can efficiently destroy their disk components and pro-

[2]We should note here that this definition is arbitrary, and different values are adopted throughout the literature for the distinction between a major a minor merger.

duce elliptical-like remnants with boxy isophotes. Minor mergers, on the other hand, with mass ratios of the order of 1:3 result in more disky (oblate) ellipticals (Naab et al. 1999; Bendo & Barnes 2000; Naab & Burkert 2003).

The mass ratio of a merger is thus very important, but only one of the various parameters that are responsible for the dynamical structure of a merger remnant. The extent of the dark matter halo of the progenitor galaxies was proven to be an equally important component. In simulations where the stellar disks of the progenitors are embedded in extended and massive dark matter halos, the resulting elliptical galaxy shows slow rotation, as the dynamical friction during the merger can efficiently transfer the orbital angular momentum of the two progenitors to the dark matter halo before they finally merge (e.g. Barnes 1988).

Gas dissipation and the subsequent star formation during a merger also affects crucially the dynamical structure of a remnant: Using a large set of wet and dry merger simulations, Cox et al. (2006) showed that wet mergers typically produce oblate rotators, with very small kinematic misalignments. On the other hand, massive, slow rotating ellipticals with boxy isophotes are much more likely to originate from dry mergers of equal mass progenitors (Khochfar & Burkert 2005; Cox et al. 2006).

Power-law and core elliptical galaxies have been associated with the presence or lack of cold gas, respectively, in their progenitors disks (e.g. Barnes & Hernquist 1991). Power-law galaxies might result from gas-rich mergers, where after the merger process gas settles to the center of the remnant and triggers a starburst of star formation, therefore steepens the light profile (Hopkins et al. 2008). However the central nuclei of some early-type (as well as late-type) galaxies might not only originate from gas infall, but also from dry accretion of globular clusters to the center of the galaxy, according to the *"cluster-inspiral scenario"* (Tremaine et al. 1975; Capuzzo-Dolcetta 1993; Antonini et al. 2012; Gnedin et al. 2014). A detailed description of the formation of galactic nuclei and nuclear star clusters is given in Section 1.2.2 and in *Chapter 4*.

Core galaxies, on the other hand, are very likely the end-products of gas-poor mergers between two galaxies hosting super-massive black holes (SMBH) at their centers. According to this paradigm, the SMBH binary formed after their coalescence ejects stars via three-body interaction, producing a density core in the center of the remnant (Milosavljević & Merritt 2001; Khochfar & Burkert 2005).

It is likely that the central parts of elliptical galaxies originate preferentially by major mergers, while their outer parts ($r > r_e$) were probably assembled by subsequent multiple minor mergers (Burke & Collins 2013; Naab et al. 2014). This is in line with lookback studies of ETGs (e.g. van Dokkum et al. 2010; Pérez et al. 2013) that report that massive ellipticals with stellar mass $M_* \gtrsim 10^{11}\,\mathrm{M}_\odot$ have gradually built up their mass by a factor of two since $z \sim 2$, with the growth affecting their effective radius greater than their stellar masses.

In support of this scenario, wide-field stellar kinematics observations out to 2-4 r_e (e.g. Arnold et al. 2014) show that most ellipticals that are slow rotators within $1r_e$, retain their slow rotation within large radii, while many fast rotators do not retain their rotation. Hence, they suggested that the oblate morphology and fast rotation of many ETGs within $1r_e$ is due to the existence of a central stellar disk,

which is embedded in a more slowly rotating and spherical structure that dominates at larger radii.

All the above findings are in favor of a new picture of the formation of ETGs: the *"two-phase assembly"* scenario, according to which fast rotators ETGs built their inner parts ($r < 1 - 2r_e$) early on through gas-rich major mergers before $z \sim 2$ that built up their central stellar disks, followed by a prolonged period of multiple minor dry mergers that affected mainly their outer parts ($r > 1 - 2r_e$) since then and built up their outer spheroidal and slow-rotating structures. Slow rotators may also fall into this picture, however it is more likely that the first phase of their assembly might have been a gas-poor major merger, especially in the case of cored ETGs or, in general, massive ETGs that do not show oblate rotation in their central parts, but for example, prolate rotation (see *Chapter 3*).

Kinematically decoupled components (KDCs) that are often observed in the central parts of slow rotators, are also a dynamical evidence for formation from an early merger since they are found to host predominantly old stellar populations (Carollo et al. 1997; McDermid et al. 2006; Kuntschner et al. 2010). The KDC is most likely to originate from a major merger of two disk galaxies, where one of them is employed on a retrograde merging orbit (opposite rotation) with respect to the other. This initial rotation axis misalignment between the progenitors disks can result in a kinematic decoupling in the center of the remnant elliptical galaxy (e.g. Bois et al. 2010, 2011). However, KDCs are very common in present-day slow-rotating ETGs, with a fraction that could be much higher than 50%. Cosmological simulations show that prograde (same rotation) and retrograde mergers are equally likely to happen (Khochfar & Burkert 2006a). Assuming that KDCs can only result from such retrograde mergers, then the probability of their formation in a "random" merger should be less than 50%. Why is the observed fraction of KDC-host galaxies higher than predicted? In *Chapter 2* we address this problem in more detail and provide a possible explanation with the discovery of a new, additional channel for the formation of KDCs in ETGs through major mergers.

It appears that the major merger scenario is the most viable hypothesis for the formation of the central parts of ETGs– ellipticals, but also lenticular galaxies (e.g. Querejeta et al. 2015). However, our understanding on the exact physical processes that govern the formation of their complex dynamical structures is still limited. Which exact dynamical processes lead to stellar counter-rotation in the center of a galaxy? Why is such a feature so commonly observed? On the other hand, why are prolate ellipticals so rarely observed? Does this imply an uncommon mechanism of their formation? How are these features connected to mergers?
In the following two Chapters we address these questions in the context of the major merger scenario and present our new findings from numerical simulations of the formation of ETGs, as well as new findings from observations of the stellar kinematics of ETGs.

1.2 Dynamical Structure and Formation of Nuclear Star Clusters

The nucleus of a galaxy is a place of particular interest. Located at the bottom of the galactic potential well, it is a region where extreme physical processes may take place, and consequently galactic nuclei are often the hosts of extreme objects. Such extremeties are nuclear star clusters (NSCs), the *densest stellar systems* known (Walcher et al. 2005), as well as supermassive black holes (SMBHs), thought to be *the densest single objects* in the present-day Universe. Both these classes of objects are often called "central massive objects" (CMOs), as they are found to reside at the centers of most galaxies across the Hubble sequence, and in some cases they even coexist, as for example in our own Milky Way.

The study of the structure and dynamics of NSCs provides important information about the physical conditions occurring at the galactic nucleus. Due to their location at the centre of the galactic potential, which is tightly connected to the secular evolution of the whole galaxy, nuclear star clusters offer a unique area of study with crucial implications for galaxy formation and evolution.

1.2.1 Observational Properties of Nuclear Star Clusters

Nuclear star clusters are very massive and compact star clusters, with typical sizes of a few parsecs and typical stellar masses of $10^6 - 10^7\,M_\odot$ (e.g. Georgiev & Böker 2014). That makes them comparable in size to globular clusters (GCs), but brighter and more massive (Walcher et al. 2005). Our nearest nuclear star cluster lies at the center of our own Milky Way, surrounding a supermassive black hole at a distance of ~8 kpc from our Sun.

Our Milky Way (MW) was the first known galaxy to host both a NSC and a central massive black hole (MBH). The MBH was discovered by Balick & Brown (1974), due to its strong radio emission in the direction of the inner ~1 pc of the galactic nucleus, hence known as Sgr A*. Due to its proximity, it is possible to monitor individual stellar orbits around Sgr A*, which allows one to measure the distance and the mass of the black hole with a high accuracy (Eckart & Genzel 1996; Genzel et al. 1997; Ghez et al. 2000; Gillessen et al. 2009). According to the most recent measurements the mass of the MBH is $M_\bullet = 4.02 \pm 0.16 \pm 0.04 \times 10^6\,M_\odot$ and is located at a distance of $R_o = 7.86 \pm 0.14 \pm 0.04$ kpc (Boehle et al. 2016)[3].

Surrounding the MBH and within the central 10 pc of Sgr A* lies the nuclear star cluster (NSC). It is a very massive NSC, with a mass of $2 - 3 \times 10^7\,M_\odot$ (Schödel et al. 2014; Feldmeier et al. 2014) and a half-light radius of 4.2 ± 0.4 pc (Schödel et al. 2014). Due to the strong interstellar extinction toward the Galactic center, the detection of the NSC is especially challenging. The NSC is optimally observed at infrared wavelengths, where the interstellar extinction is minimized but its stellar emission still dominates. The MW NSC was first discovered as a source of infrared radiation at wavelengths of 1.65, 2.2 and 3.4 μm at the Galactic center by Becklin & Neugebauer (1968), who also found an agreement between a similar source of infrared luminosity in the nucleus of M31 (Andromeda

[3] errors correspond to orbital fitting uncertainty and jackknife uncertainty from the reference frame.

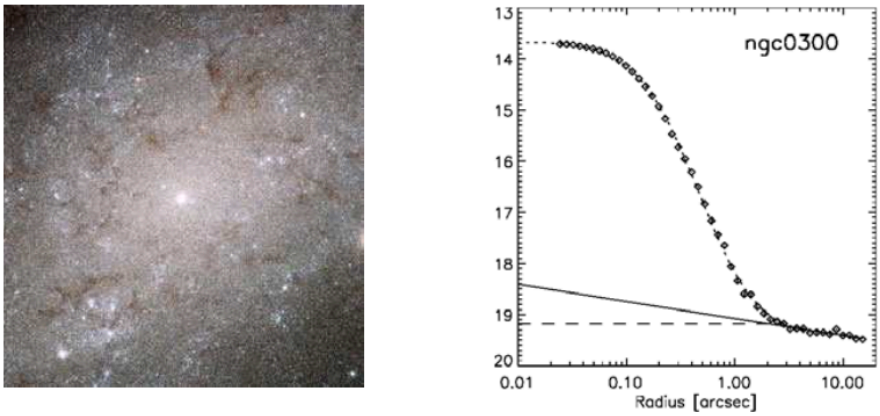

Figure 1.7: *Left:* HST color composite image of the central 1.2 × 1.2 kpc^2 of the spiral galaxy NGC 300, with the prominent NSC at its center. *Right:* I-band surface brightness profile in mag/arcsec^2 for the central 10 arcsec (87 pc) of the galaxy. The NSC is evident as an overluminosity in the brightness profile, as compared to inward extrapolations (solid, dashed lines) of the brightness profile at large radii. Adapted from van der Marel et al. (2007).

galaxy).

Over the last few years, recent observational advancements, such as the high spatial resolution observations provided by the Hubble Space Telescope (HST) have confirmed the existence of NSCs in the centers of many more galaxies across the Hubble sequence. A NSC is typically detected as a distinct overluminosity (upturn) in the central few parsecs of the brightness profile of a galaxy, as compared to inward extrapolations of the brightness profile at larger radii. Figure 1.7 shows an image of the NSC in the central region of the galaxy NGC 300, and its corresponding brightness profile, as an example.

One of the most striking results of these extragalactic studies is that NSCs are *extremely common* in galaxies of all morphological types: more than 77% of late-type galaxies host a NSC at their centre (Böker et al. 2002; Georgiev & Böker 2014), as well as at least 66% of early-type galaxies, mainly dwarf ellipticals and lenticulars (Côté et al. 2006; Turner et al. 2012; den Brok et al. 2014). These fractions establish only a lower limit to the true fraction of galaxies hosting NSCs, mainly due to several observational biases that can limit their detection. Such biases are mainly the strong presence of dust in and around galactic nuclei and/or the bright stellar background of the bulge component of the host galaxy. The latter may explain especially the lower fraction of NSC detections in earlier type galaxies (ETGs).

Even though NSCs appear to be similar in size to globular clusters (but more massive and dense), they are more flattened and show stronger rotation. In the Milky Way (MW), the amplitude of the stellar line-of-sight velocity of the NSC is ~40 km·s^{-1} within its effective radius r_e~4-5 pc. The rotation axis of the MW NSC is misaligned with respect to the rotation axis of the galactic plane by ~9° (see Figure 1.8, Feldmeier et al. 2014). In extragalactic NSCs, their rotation axis is aligned to

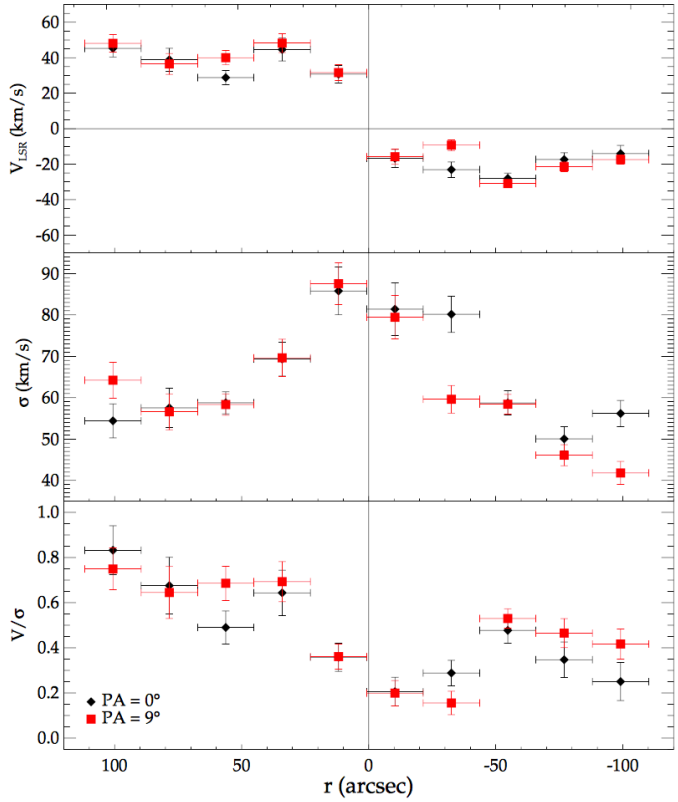

Figure 1.8: Velocity profile, velocity dispersion σ, and V/σ of the MW NSC, for a 22 arcsec broad slit along the Galactic plane (black diamonds), and for a slit tilted by 9° counterclockwise with respect to the Galactic plane (red square symbols). The latter shows higher rotation and reveals the kinematic misalignment of the NSC with respect to the Galactic plane. From Feldmeier et al. (2014).

within ~10° compared to the one of the host galaxy (in case of late-type, edge-on galaxies, Seth et al. 2006).

NSCs in late-type galaxies often consist of an old spheroidal component and a younger and bluer embedded stellar disk (Seth et al. 2006, 2008). Such NSCs thus exhibit complex star formation histories, with mean luminosity-weighted ages ranging from 10 Myr to 10 Gyr (Rossa et al. 2006). Their star formation is likely to happen in an episodic manner, (e.g. Schinnerer et al. 2008), recurring on a timescale of the order of 100 Myr (Walcher et al. 2005, 2006).

In the MW NSC, observational evidence shows that there has been an increase in star formation in the last few hundred Myr of its evolution (Blum et al. 2003; Pfuhl et al. 2011). In the very centre (~0.5 pc) the light is dominated by ~6 Myr old stars (e.g. Paumard et al. 2006; Feldmeier-Krause et al. 2015). However, the formation of the NSC must have started about 10 Gyr ago and ~80% of the MW NSC stars are more than 5 Gyr old (Pfuhl et al. 2011).

NSCs characteristics appear to correlate strongly with global properties of their host galaxies. Apart from their small misalignments observed with the galactic plane, also their masses seem to correlate

tightly with the host stellar velocity dispersion and bulge luminosity (Wehner & Harris 2006; Rossa et al. 2006; Ferrarese et al. 2006), or, especially for disk galaxies, with the total stellar galaxy mass (Erwin & Gadotti 2012). SMBHs also show such correlations, however it is not clear how similar their correlations are with the ones of NSCs (e.g. Graham 2012; Scott & Graham 2013; Kormendy & Ho 2013). Nevertheless, these findings suggest that the formation processes and growth mechanisms of both NSCs and SMBHs must be tightly associated with the properties of their host galaxy. As SMBHs have no memory, the stars of NSCs are the only tracers of the mechanisms responsible for the build-up of the galactic central regions. As a consequence, the study of NSCs can reveal important information about the secular evolution of their host galaxies.

Why are NSCs so commonly observed in the centers of galaxies? How do they form and evolve? What does this imply for the formation and secular evolution of their host galaxies?

In order to address these still widely debated topics, we will give a brief summary of the scenarios suggested for the formation of NSCs. As adopted throughout this thesis, our primary tool to understand the origin and evolution of these systems is their stellar dynamics, as observed with IFS data and as derived from numerical simulations of their formation.

1.2.2 Formation of Nuclear Star Clusters

The two main scenarios suggested for the formation of nuclear star clusters are:

1. The *in situ formation scenario* (Loose et al. 1982; Milosavljević 2004) that favors gas accretion. The NSC forms as gas infalls to the center of the galaxy, where subsequently star formation takes place locally and most likely in an episodic manner (e.g. Schinnerer et al. 2008).

2. The *cluster-inspiral (merger) scenario* (Tremaine et al. 1975; Capuzzo-Dolcetta 1993; Antonini et al. 2012; Gnedin et al. 2014), that favors the accretion of massive globular clusters, that infall to the center of the galaxy due to dynamical friction and subsequently merge to form the NSC.

Both of these models can explain the mixture of stellar populations of different ages in NSCs (e.g. Walcher et al. 2006; Rossa et al. 2006; Seth et al. 2010; Georgiev & Böker 2014).

It is very likely that *both* mechanisms work in parallel to form and grow NSCs. The search for the dominant mechanism for the formation of NSCs is still an ongoing and widely debated topic. Our approach is that the detailed study of the dynamics of NSCs, in combination with results from numerical simulations, can provide a very important tool to dissentagle and reveal the relevant importance between the two possible formation mechanisms.

So far the most direct dynamical evidence for the need of in situ star formation comes from numerical simulations by Hartmann et al. (2011), tuned to explain the kinematic properties of extragalactic NSCs. They found that the globular cluster merger scenario cannot reproduce the high amount of rotation observed in the inner parts of NSCs. Additionally, they find that merger remnant NSCs show

a central peak in the second order kinematic moment $V_{RMS} = \sqrt{V^2 + \sigma^2}$ which does not agree with observations of some extragalactic NSCs. Based on this, they conclude that less than ~50% of the mass of the NSC could have been assembled from the mergers of GCs, with the majority due to in situ star formation.

However, in the case of the Milky Way NSC, recent findings by Feldmeier et al. (2014) show a central peak in V_{RMS}. They also report strong evidence for a polar kinematic substructure (a kinematically decoupled component or twist) in its central region. These findings, combined with the kinematic misalignment between the main body of the NSC and the Galactic plane, show that the accretion processes that accounted for its formation might have not originated from the galactic plane, as one would expect in the case of gas accretion. Especially the stellar kinematic substructure, that appears to rotate with almost a ~90° misalignment from the rotation axis of the Galactic plane, might have been formed by globular cluster mergers, as it appears to host predominantly old populations (Feldmeier et al. 2014).

Kinematic substructures have been additionally reported in extragalactic NSCs: Seth et al. (2010) and Lyubenova et al. (2013) report the existence of counter-rotating stellar populations in the NSCs of the early-type galaxies NGC 404 and FCC 277, respectively.

Several questions emerge from these findings. Kinematically decoupled components (KDCs) in NSCs are, as in the case of KDCs in early-type galaxies, the direct dynamical evidence of formation by mergers. However, *the observed rotation of NSCs has been so far attributed mainly to gas accretion. How can globular cluster inspiral produce rotating NSCs?*

In *Chapter 4* we address these open questions, with particular attention to the Milky Way NSC. We present findings from numerical simulations and show that globular cluster mergers can account for a variety of dynamical properties of the MW NSC, including significant rotation, in contrast to what was previously thought. Our findings suggest that the merger origin of NSCs is a viable hypothesis for their main assembly.

1.3 Research Content

The goal of this thesis is to investigate the connection between the merger origin and the dynamical structure and evolution of stellar systems on different spatial scales. The thesis is structured as follows:

In ***Chapter 2***, we discuss the merger origin of kinematically decoupled cores in early-type galaxies and present a new channel for their formation using merger simulations. In ***Chapter 3***, we show whether and how prolate rotation in early-type galaxies can be a result of mergers, using simulations, and additionally present new observational findings for prolate stellar rotation in early-type galaxies from the CALIFA Survey. In ***Chapter 4*** we investigate the merger origin of nuclear star clusters and present new findings from numerical simulations. We show that a merger origin can account for their observed dynamical features, and in particular the ones observed in the nuclear star cluster of

our Milky Way. In ***Chapter 5*** we summarize and discuss the findings presented in this thesis. In addition we present a brief description and preliminary results from our current and future research programs. In particular, our research outlook addresses the dynamical modeling of early-type galaxies (Appendix), the existence of intermediate mass black holes in nuclear star clusters, and the connection between globular and nuclear star clusters.

The content of Chapters 2, 3 and 4 are based on the following papers:

- A. Tsatsi, A. V. Macciò, G. van de Ven and B. P. Moster, 2015, *"A New Channel for the Formation of Kinematically Decoupled Cores in Early-Type Galaxies"*, ApJ, 802, L3 (*Chapter 2*)
- A. Tsatsi, A. Mastrobuono-Battisti, G. van de Ven, H. B. Perets, P. Bianchini and N. Neumayer, 2016*a*, *"On the Rotation of Nuclear Star Clusters formed by Cluster-inspirals"*, MNRAS in press, accepted 6 Oct. 2016, ArXiv e-prints: 1610.01162 (*Chapter 4*)
- A. Tsatsi, M. Lyubenova, G. van de Ven et al., 2016*b*, *"CALIFA reveals Prolate Rotation in Early-type Galaxies: A Polar Galaxy Merger Origin?"*, to be submitted (*Chapter 3*)

Chapter 2

The Merger Origin of Kinematically Decoupled Cores in Early-type Galaxies

Early-type galaxies (ETGs) are the end-products of complex assembly and evolutionary processes that determine their shape and dynamical structure. Signatures of such past processes in present-day ETGs are likely to be in the form of peculiar kinematic subsystems that reside in their central regions. Such subsystems are Counter-Rotating Cores (CRCs) or general, *Kinematically Decoupled Cores/Components (KDCs)* and they are defined as central stellar components with distinct kinematic properties from those of the main body of the galaxy (e.g. McDermid et al. 2006; Krajnović et al. 2011; Toloba et al. 2014).

In this chapter we discuss the prominent existence of KDCs in ETGs, their possible merger origin and present a new channel for their formation. These findings are described in Tsatsi et al. (2015).

2.1 Observations of KDCs

KDCs were first discovered using one-dimensional long-slit spectroscopic observations of the stellar kinematics of ETGs (Efstathiou et al. 1982; Bender 1988; Franx & Illingworth 1988). More recently, integral-field unit spectroscopic surveys like SAURON (Bacon et al. 2001), ATLAS^{3D} (Cappellari et al. 2011), CALIFA (Sánchez et al. 2012) or MUSE (Bacon et al. 2010), being able to provide full two-dimensional observations of the stellar kinematics, have favored the detection of KDCs and revealed that a substantial fraction of ETGs in the nearby universe show kinematic decoupling in their central regions. This fraction ranges in different surveys, depending mainly on technical and sample-selection biases.

Notably, the fraction of ETGs that host KDCs in the SAURON sample, consisting of 48 E+S0 galaxies (de Zeeuw et al. 2002) is substantially high, especially in the centers of slow-rotating ETGs: 8 out of the 12 slow rotators ($\sim$ 67%) from the main survey host a KDC (Emsellem et al. 2007). In the ATLAS^{3D} volume-limited sample of 260 ETGs, this fraction is 47% (see Figure 2.1, Krajnović et al. 2011). The KDCs found in slow rotators are typically "old and large", with stellar populations older than 8 Gyr that show little or no age differences with their host galaxy, and sizes larger than 1 kpc (McDermid et al. 2006; Kuntschner et al. 2010).

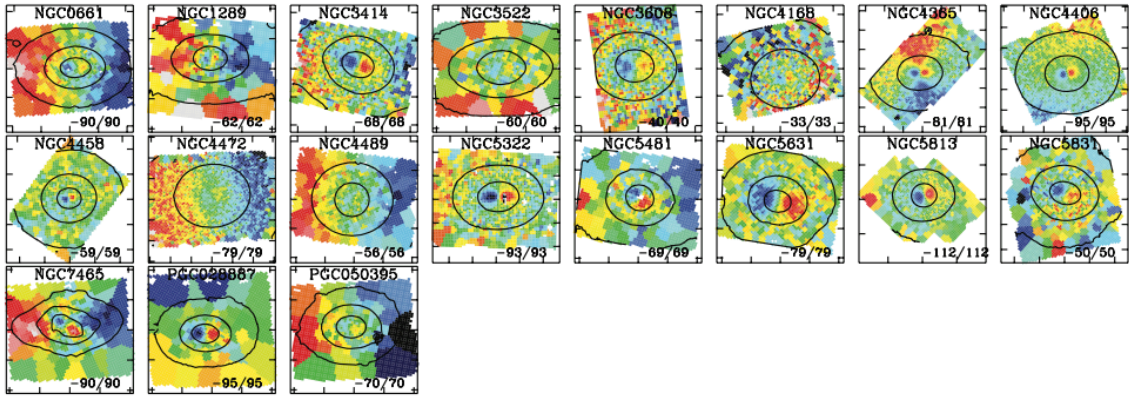

Figure 2.1: Early-type galaxies from the ATLAS^{3D} Survey that show a kinematically decoupled component (KDC) in their central stellar regions. The values on the bottom right corner denote the range of the stellar velocities plotted (adapted from Krajnović et al. 2011).

KDCs are also detected in fast-rotating ETGs. 25% of fast rotators from the SAURON survey host KDCs. This type of KDCs are typically "young and compact", with stellar populations younger than 5 Gyr and sizes less than a few hundred parsecs (McDermid et al. 2006).

We note that these fractions establish a lower limit to the true fraction of ETGs with kinematically decoupled regions, considering projection effects, the fact that young and compact KDCs are subject to technical or observational biases (e.g. McDermid et al. 2006), while many ETGs with resolved KDCs in their centers are subject to different classifications throughout the literature (e.g. 2σ-galaxies, see Krajnović et al. 2011).

Current and future observational advancements will, however, be able to reveal the existence of KDCs in many more ETGs. A recent example is M87, a giant elliptical galaxy in the Virgo cluster, that was for long considered to be non-rotating (SAURON, Emsellem et al. 2004) and was later discovered, using the MUSE spectrograph, to exhibit a low-amplitude KDC in its central region (Emsellem et al. 2014).

2.2 The Standard Paradigm

While a consensus is reached about the prominent existence of KDCs in luminous ETGs, the physical processes and the rate at which they are formed are still poorly understood. There is no unified mechanism for the formation of KDCs. Young and compact KDCs in fast rotators might have formed via star-formation in situ. According to this scenario, the stellar component of the KDC is formed in initially kinematically misaligned gaseous regions, probably originating from externally accreted gas or unequal mass merging (Hernquist & Barnes 1991), where the orientation of the merging orbit defines the orientation of rotation of the resulting KDC. Following this line of thought, Balcells &

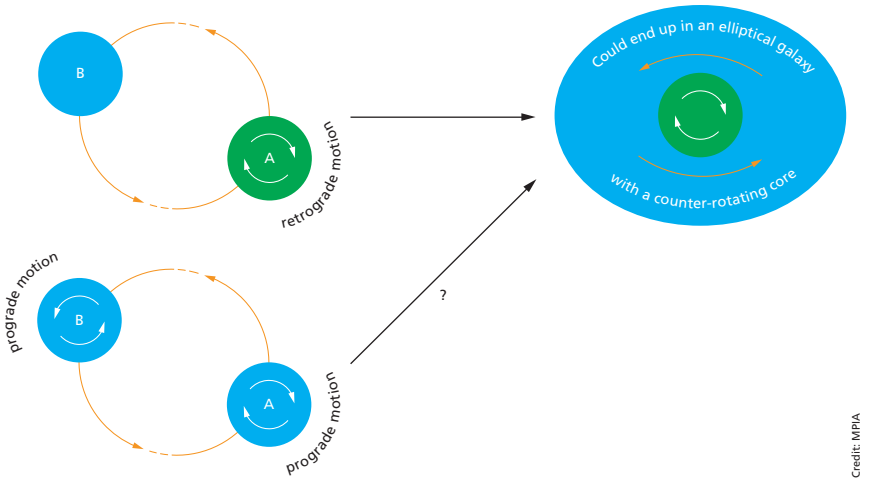

Figure 2.2: Schematic diagram of the standard paradigm for the formation of KDCs/CRCs. Top: retrograde mergers of two disk galaxies are able to result in elliptical galaxies with KDCs. Bottom: prograde mergers were, until now, not thought to be able to form KDCs (image credit and concept: MPIA Graphics Department and A.Tsatsi).

Quinn (1990) suggested that counter-rotating cores can only result from retrograde mergers.

However, this scenario could not hold for the large and old KDCs found in slow rotators, whose stellar population was probably formed at the same epoch as the main body of the galaxy. In this case, processes such as gas accretion or accretion of low-mass stellar systems are more likely to affect the outer parts of the galaxy and can not be consistent with observations that show no color gradients between the KDC and the surrounding galaxy (Carollo et al. 1997).

The most plausible formation scenario that could explain the similarity of the stellar content of the KDC and the main body of the galaxy is major merging. This scenario has been confirmed in simulations (e.g. Bois et al. 2010, 2011), resulting in elliptical-like and slow-rotating merger remnants hosting KDCs only when the two progenitor galaxies were initially following retrograde merger orbits. Using mergers of type Sb and Sc galaxies, they show that a KDC is formed as long as the more dynamically stable of the two progenitors is on a retrograde orbit. Figure 2.2 shows a schematic diagram of the "standard paradigm" of the formation of KDCs.

These studies imply that if retrograde and prograde orbits are equally likely to happen (e.g. Khochfar & Burkert 2006a), then the maximum probability to form a KDC in a "random" merger would be $\sim 50\%$. In large surveys, such as ATLAS^{3D}, the fraction of slow rotators that harbor KDCs is $\sim 47\%$ ($\sim 67\%$ for the SAURON Survey). These values only represent a lower limit to the true fraction of KDCs, considering projection effects and technical/observational biases, as discussed in Section 2.1.

Another scenario that suggests that the true rate at which KDCs are created in ETGs might be well above the theoretical prediction of the upper limit of $\sim 50\%$, is the scenario of "fading KDCs", according to which the light of young and compact KDCs can fade significantly as its stellar population ages,

to a point where they can be barely visible after a few Gyr of evolution (McDermid et al. 2006). This suggests that the rate at which (especially) compact and old KDCs are created should be significantly larger than their corresponding observed present-day fractions.

All the above evidence suggests that the fact that a KDC is not observed in the present-day kinematics of a galaxy, does not mean that (a) it is not there or/and (b) that it might not have existed at some point during its lifetime.

This implies that kinematic decoupling might be a much more common feature during the formation of early-type galaxies than the aforementioned observed KDC fractions, which can not be explained only by retrograde mergers. This is pointing to the need of additional KDC formation scenarios that can add to their predicted rate of occurence.

2.3 A New Formation Channel

In Tsatsi et al. (2015) we show that, a KDC might as well result from an *initially prograde* major merger simulation. The kinematic decoupling in the center of the final elliptical-like merger remnant can result from a short-lived change of the orbital spin of the two progenitor galaxies right after their second encounter. This new channel for the formation of KDCs might serve as an additional mechanism that can help towards explaining their observed rate of occurrence in ETGs.

2.3.1 Simulation Parameters

The simulation reproducing an elliptical galaxy through a major merger that we use is described in Moster et al. (2011). It was performed using the TreeSPH-code GADGET-2 (Springel 2005). GADGET simulates the evolution of a self-gravitating collisionless *N*-body system, and allows gas dynamics to be included by means of smooth particle hydrodynamics (SPH), including star formation and supernova feedback.

The two progenitor disk galaxies in this simulation are identical and they are composed of a cold gaseous disk, a stellar disk and a stellar bulge, which are embedded in a dark-matter and hot-gas halo.

The gaseous and the stellar disk of each progenitor galaxy have exponential surface brightness profiles and they are rotationally supported, while the spherical stellar bulge follows a Hernquist (1990) profile, and is initially non-rotating[1]. The dark matter halo has a Hernquist profile and a spin parameter consistent with cosmological simulations (Macciò et al. 2008). The hot gaseous halo

[1]We note that these initial structural properties of the progenitors are influenced by their close interaction, i.e. they develop bulge rotation, bars and spiral arms in the first few hundred Myr of the simulation.

follows the β -profile (Cavaliere & Fusco-Femiano 1976)[2] and is rotating around the spin axis of the disk (see Moster et al. 2011 for a more detailed description of the galaxy model).

The stellar mass of each progenitor is $M_* = 5 \cdot 10^{10}\,\mathrm{M}_\odot$ and the bulge-to-disk stellar mass ratio was chosen to be $B/D = 0.22$. The mass of the cold gaseous disk is $M_{g,cold} = 1.2 \cdot 10^{10}\,\mathrm{M}_\odot$, such that the gas fraction in the disk is 23%. The virial mass of the dark matter halo is $M_{dm} = 1.1 \cdot 10^{12}\,\mathrm{M}_\odot$, while the mass of the hot gaseous halo is $M_{g,hot} = 1.1 \cdot 10^{11}\,\mathrm{M}_\odot$. The system is modelled with N_{dm}=500 000 dark matter particles, N_{disc}=100 000 stellar disk, $N_{g,cold}$=33 333 gaseous disk, N_{bulge}=20 000 bulge and $N_{g,hot}$=375 000 hot gaseous halo particles. The softening length is 100 pc for stellar, 400 pc for dark matter and 140 pc for gas particles.

The two progenitors are initially employed in a nearly unbound prograde parabolic orbit, with an eccentricity of $e = 0.95$ and a pericentric distance of $r_{p_1} = 13.6$ kpc. Such an orbit is representative for the most common major mergers in ΛCDM cosmology (Khochfar & Burkert 2006b). The two galaxies have an initial separation of $d_{start} = 250$ kpc. The orbital and the rotation spin of the first galaxy are aligned, while the spin axis of the second galaxy is inclined by θ=30 ° with respect to the orbital plane. The simulation lasts for 5 Gyr, such that the remnant elliptical galaxy is fully relaxed.

2.3.2 Structure and Kinematics of the Merger Remnant

In order to connect the orbital and mass distribution of our simulated galaxy with observable properties, we create two-dimensional mock stellar mass maps as follows. Stellar particles are projected such that the galaxy is seen edge-on with respect to the initial orbital plane of the merger. Particles are then binned on a regular grid centered on the baryonic center of mass of the galaxy. We adopt a distance of 20 Mpc, so that 1 arcsec corresponds roughly to 0.1 kpc. Our grid has a size of 20x20 kpc^2, covering approximately twice the half-mass radius (r_h) of our galaxy, and a pixel size of 0.075 kpc, so that it corresponds to the spatial resolution of the IRAC camera of the Spitzer Space Telescope (Fazio et al. 2004).

We parametrize the galaxy's projected stellar mass distribution using the Multi-Gaussian Expansion (MGE) model (Monnet et al. 1992; Emsellem et al. 1994), as implemented by Cappellari (2002), where the galaxy's stellar surface brightness distribution is fitted with a sum of 2D Gaussians, while allowing for position angle twists and ellipticity variations in the projected distribution.

The intrinsic shape of the remnant's stellar particle distribution is parametrized using an iterative method to obtain the best fitting ellipsoid to the distribution and to extract the eigenvalues of the mass tensor inside this ellipsoid (Macciò et al. 2008). The intermediate-to-long and short-to-long axes ratios that we retrieve are p=0.88 and q=0.54, respectively, and the average projected ellipticity of the

[2]This profile is commonly used to describe the density distribution of hot gas in clusters:

$$\rho_{hg}(r) = \rho_0 \left(1 + \left(\frac{r}{r_c}\right)^2\right)^{-\frac{3}{2}\beta}, \tag{2.1}$$

where the ρ_0 is central density, r_c the core radius and β the outer slope parameter of the hot gas density profile.

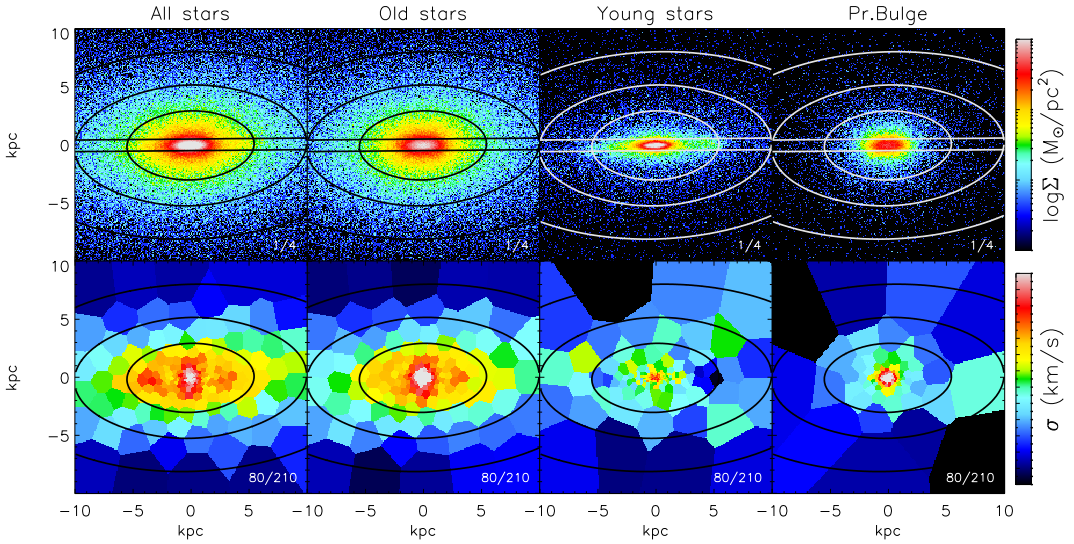

Figure 2.3: From left to right: Component analysis of the merger remnant's stellar population: all stars (old+young), old stars (>5 Gyr), young stars (<5 Gyr), and "Pr.Bulge" stellar population. The latter are particles that initially formed the bulge of the progenitor galaxies. Top row shows the 2D maps of the line-of-sight projected stellar mass surface density (Σ) and bottom row shows velocity dispersion (σ) for every component. Overplotted are the MGE best-fitting contours of the total projected stellar mass, as a reference. The remnant is seen edge-on with respect to the orbital plane of the two progenitors. (Adapted from Tsatsi et al. 2015).

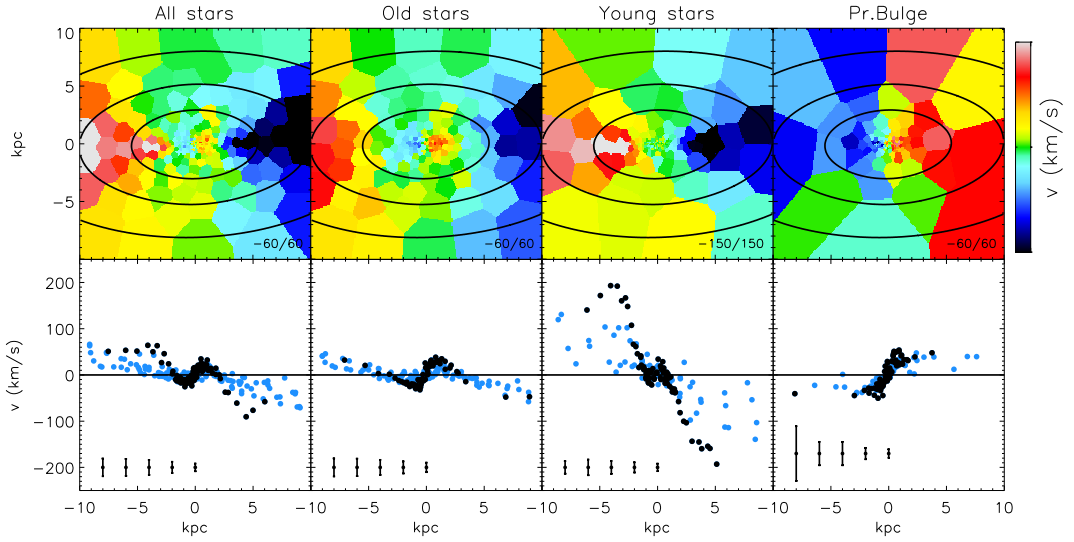

Figure 2.4: Line-of-sight projected stellar rotation for every component of Figure 2.3. The top row shows the 2D maps of the line-of-sight projected stellar mean velocity (v) for every component. The bottom row shows the stellar rotation curve extracted from the 2D velocity maps: black points correspond to the mean velocity per bin inside a slit of 1 kpc width along the apparent major photometric axis (the position of the slit is shown at the top row figures of Figure 2.3). Blue points correspond to bins outside the slit. Typical average errors are shown at the bottom. (Adapted from Tsatsi et al. 2015).

remnant is $\epsilon = 0.49$, estimated within 2 r_h.

Stellar particles are projected along the chosen viewing angle and binned on a regular 20x20 kpc grid centered on the baryonic center of mass of the galaxy. In order to mimic real integral-field spectroscopic data, the pixel size of 0.1 kpc corresponds, at the adopted distance of 20 Mpc, approximately to the spatial resolution of the SAURON spectrograph (Bacon et al. 2001). The bulk velocity of the galaxy is estimated within a sphere of 50 kpc around the center and subtracted from all particle velocities. Then we extract the mass-weighted stellar line-of-sight mean velocity and velocity dispersion for every pixel. The extracted kinematic maps are spatially binned using the 2D Voronoi binning method (Cappellari & Copin 2003), based on a minimum number of particles per pixel in the map. Signal corresponds to the number of particles per pixel and we adopt Poisson noise, such that our signal-to-noise ratio per bin (SN_{bin}) should correspond approximately to a target value $SN_T \sim 30$.

We also use a simple logarithmic function inferred from CALIFA data (Husemann et al. 2013) to construct mock velocity errors of our binned kinematic data:

$$\delta\upsilon = 5\,SN_T(1 + 1.4\log N_{pix})/SN_{bin},\ \mathrm{km\,s^{-1}} \tag{2.2}$$

where N_{pix} is the number of pixels per bin.

For the purpose of this work, we divide the stellar particles of the remnant into 4 different components: "old stars", which are stars that initially were part of the progenitors' stellar material, (ages > 5 Gyr), "young stars", which were formed during the merger (ages < 5 Gyr) and "all stars", which is the total stellar content of the merger remnant. We also track the stellar particles in the remnant that initially formed the bulges of the two progenitor galaxies. These particles form the "Pr.Bulge" (Progenitor bulge) stars. The projected two-dimensional stellar mass and the stellar kinematics for every stellar component are shown in Figures 2.3 and 2.4.

One can clearly see from the velocity maps the presence of a large-scale KDC of radius ∼2 kpc in the center of the elliptical merger remnant (Figure 2.4). This component is a counter-rotating component with respect to the outer body of the galaxy and is most prominent in the "old" stellar population kinematics: stars that initially belonged to the two progenitor galaxies.

On the other hand, "young" stars form a stellar disk which is almost aligned with the orbital plane of the two progenitors. This young stellar disk is rotationally supported and strongly prograde-rotating, with a maximum velocity which is 4 times higher than the one of the "old stars". We also note a weak sign of counter-rotation in the central region of the disk, seen in the extracted stellar rotation curve.

Notably, stars that were initially part of the two progenitors' bulges ("Pr.Bulge") are globally counter-rotating in the merger remnant, exhibiting almost a solid-body rotation.

One can also see the presence of two symmetrical off-centered peaks in the "all stars" stellar velocity dispersion map of Figure 2.4. This feature is commonly observed in ETGs with counter-rotating components (CRC). These galaxies are called "2σ-galaxies"(Krajnović et al. 2011), and they were associated with external accretion of counter-rotating gas (Rubin et al. 1992) or major retrograde mergers (Crocker et al. 2009). Here we see that a 2σ-galaxy results from a single, prograde major

merger. We also note that the 2σ-feature is more prominent in the "all stars" map, where the young disk of stars is present, and less strong in the "old stars" map, even though the CRC is more prominent in the latter. In real ETGs a 2σ-feature usually implicates the existence of a CRC, while the opposite is more ambiguous. Here we show that the 2σ-feature might arise because of the presence of the CRC, but it is enhanced only if one of the components is fast-rotating[3].

2.3.3 Origin of the Kinematic Decoupling: the Mestschersky Mechanism

In order to understand the origin of the kinematic decoupling in the central region of the galaxy, we study the behavior of the merging orbits of its two progenitors: Figure 2.5 shows the separation (d) and the specific orbital angular momentum (l_z) for one of the two progenitors as a function of time. The merging orbits are shown in Figure 2.6, viewed face-on with respect to the initial orbital plane.

[3]We should note, however, that most 2σ-galaxies do not exhibit a centrally peaked velocity dispersion, like the one presented here.

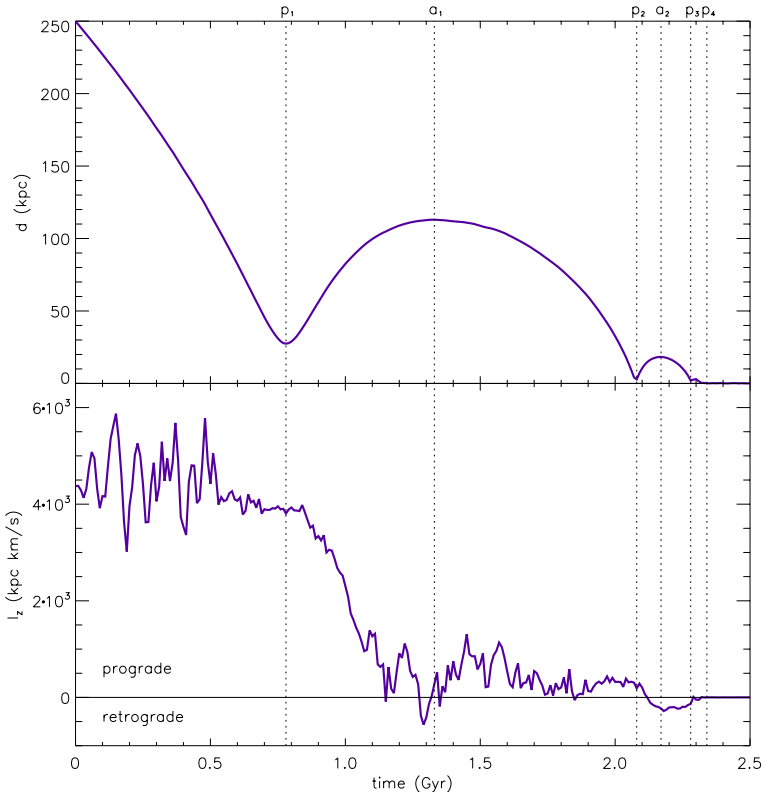

Figure 2.5: Separation (d) and specific orbital angular momentum (l_z) of the two progenitor galaxies as a function of time. Times p_1, p_2, p_3 and p_4 indicate the time of the 1st, 2nd, 3d and 4th pericentric passage. Times α_1 and α_2 denote the 1st and the 2nd apocentric passage. The orbital spin of the two progenitors changes after p_2. (Adapted from Tsatsi et al. 2015).

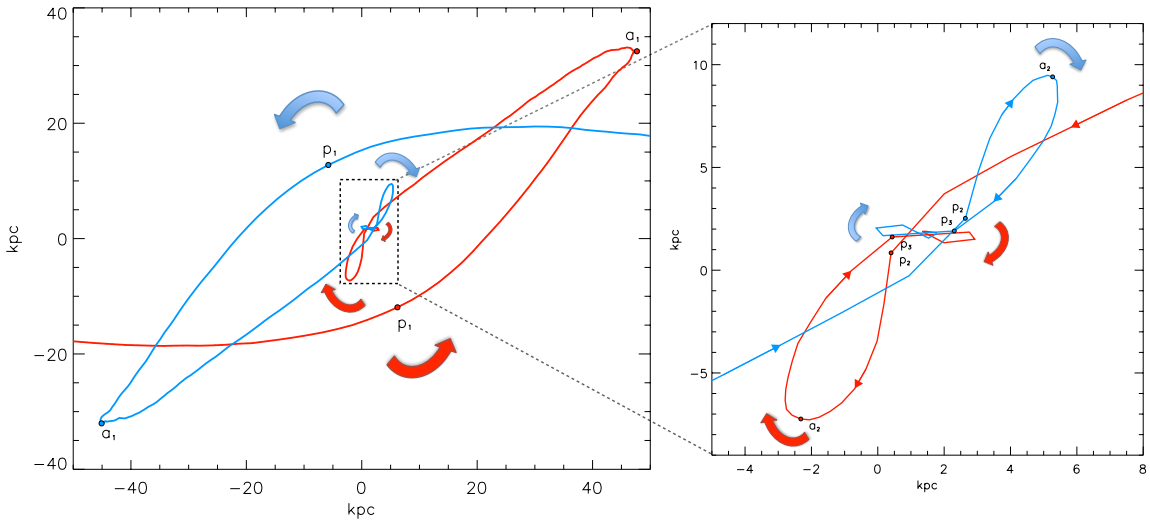

Figure 2.6: Merging orbits of the two progenitor galaxies, with the orbital plane seen face-on. Each curve (red and blue) corresponds to the orbit of each progenitor's bulge center of mass; the red curve denotes the galaxy that has its disk aligned with the orbital plane. Red and blue arrows show the direction of the orbital spin. *Left:* p_1 denotes the 1st pericentric passage, when the two galaxies follow prograde orbits. The orbital spin changes sign right after the second pericentric passage p_2. *Right:* Zoom-in view of the region inside the dashed line on the right, when the orbits become retrograde. (Adapted from Tsatsi et al. 2015).

At the time the two progenitors reach their first pericenter (p_1=0.78 Gyr), they become tidally distorted, resulting in long trailing arms that expel loosely bound material from their disks. The orbital angular momentum is decreasing due to mass loss and dynamical friction (Figure 2.5). This causes the galaxies to approach their second pericenter (p_2=2.08 Gyr) with almost radial orbits (Figure 2.6). After their second encounter, the two galaxies change their orbital spin and follow a retrograde orbit for ~300 Myr, until they finally reach their coalescence at t~2.4 Gyr.

The sudden change from a prograde to a retrograde merger can be understood in the framework of reactive forces. Due to strong tidal interactions during the merger, the two progenitor galaxies are systems of variable mass; mass is constantly ejected along their short-lived trailing arms. We suggest that the mass loss from each system results in a reactive force, known as the Mestschersky (1902) force:

$$\overrightarrow{R} = \dot{m}(\overrightarrow{v} - \overrightarrow{V}) \tag{2.3}$$

where $\dot{m}$ is the mass loss rate, $\overrightarrow{V}$ the bulk velocity of the system and $\overrightarrow{v}$ is the velocity of the outflowing matter. The Mestschersky force acts upon the two galaxies as a "reactive thrust" which, if strong enough, can cause the change of the orbital spin. Figure 2.7 shows a schematic diagram of the suggested "Mestschersky mechanism".

Due to this effect, the central region of the final remnant is counter-rotating and the width of the last oscillation before coalescence corresponds to the size of the KDC (~2 kpc), which is prominent in the

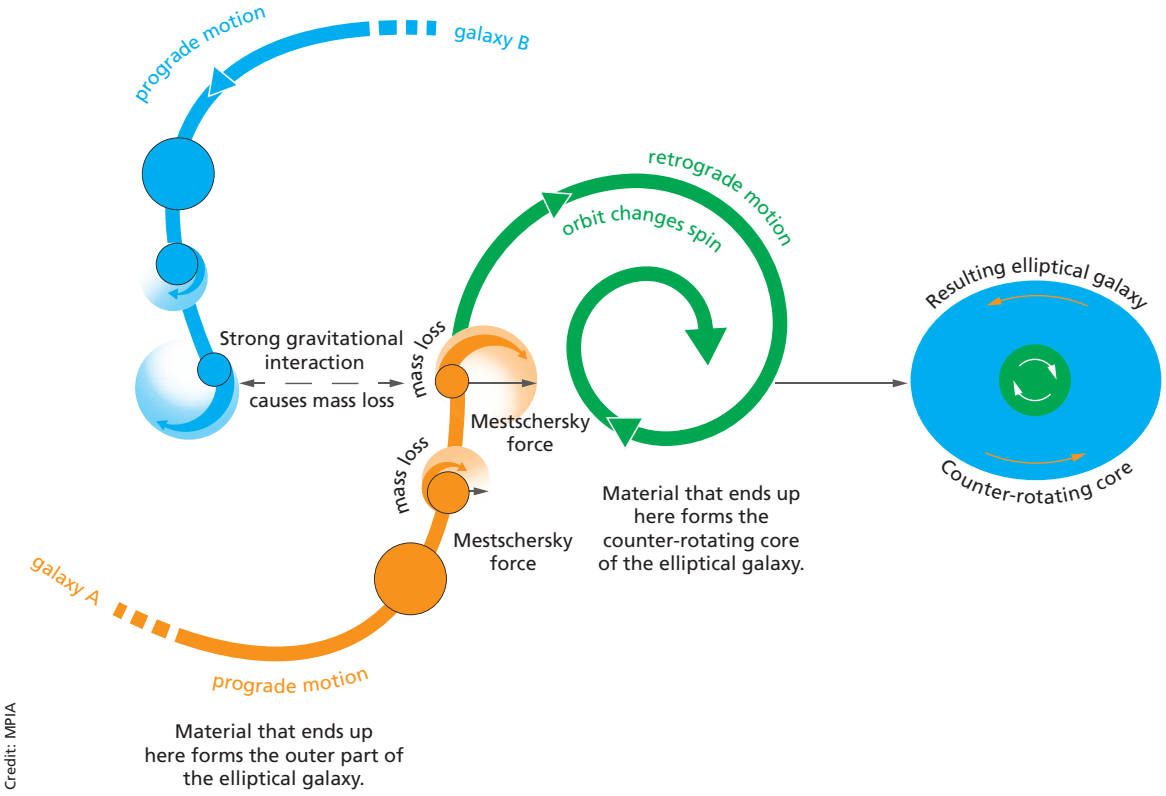

Figure 2.7: Schematic diagram of the suggested *"Mestschersky mechanism"*, that results in the reversal of the orbital spin of two merging galaxies: mass loss due to strong tidal forces during their close encounter results in a reactive force (Mestschersky force) causing the orbit to change spin. Material that gets ejected during the encounter forms the outer part of the final elliptical galaxy, while the two retrograde-rotating cores survive after the merger in the central part of the elliptical galaxy, resulting in a counter-rotating component. (Image credit and concept: MPIA Graphics Department and A.Tsatsi).

center of the galaxy for more than 2 Gyr after the kinematic decoupling of its progenitors.

Figure 2.8 shows in detail this effect after the second pericentric passage in our simulations. After the two progenitors approach closely, strong tidal forces that act upon them result in short-lived trailing arms, which mainly consist of their disks' stellar component. Loosely bound material gets ejected along these arms, resulting into a strong reactive thrust to the main bodies of the progenitors, causing them to change their orbital spin and follow retrograde trajectories until their coalescence at t~2.4 Gyr[4].

Under this framework, one can explain why stars that were initially part of the progenitors' bulges

[4]The suggested mechanism could be responsible for the formation of KDCs in non-retrograde close encounters, e.g.Barnes (2002).

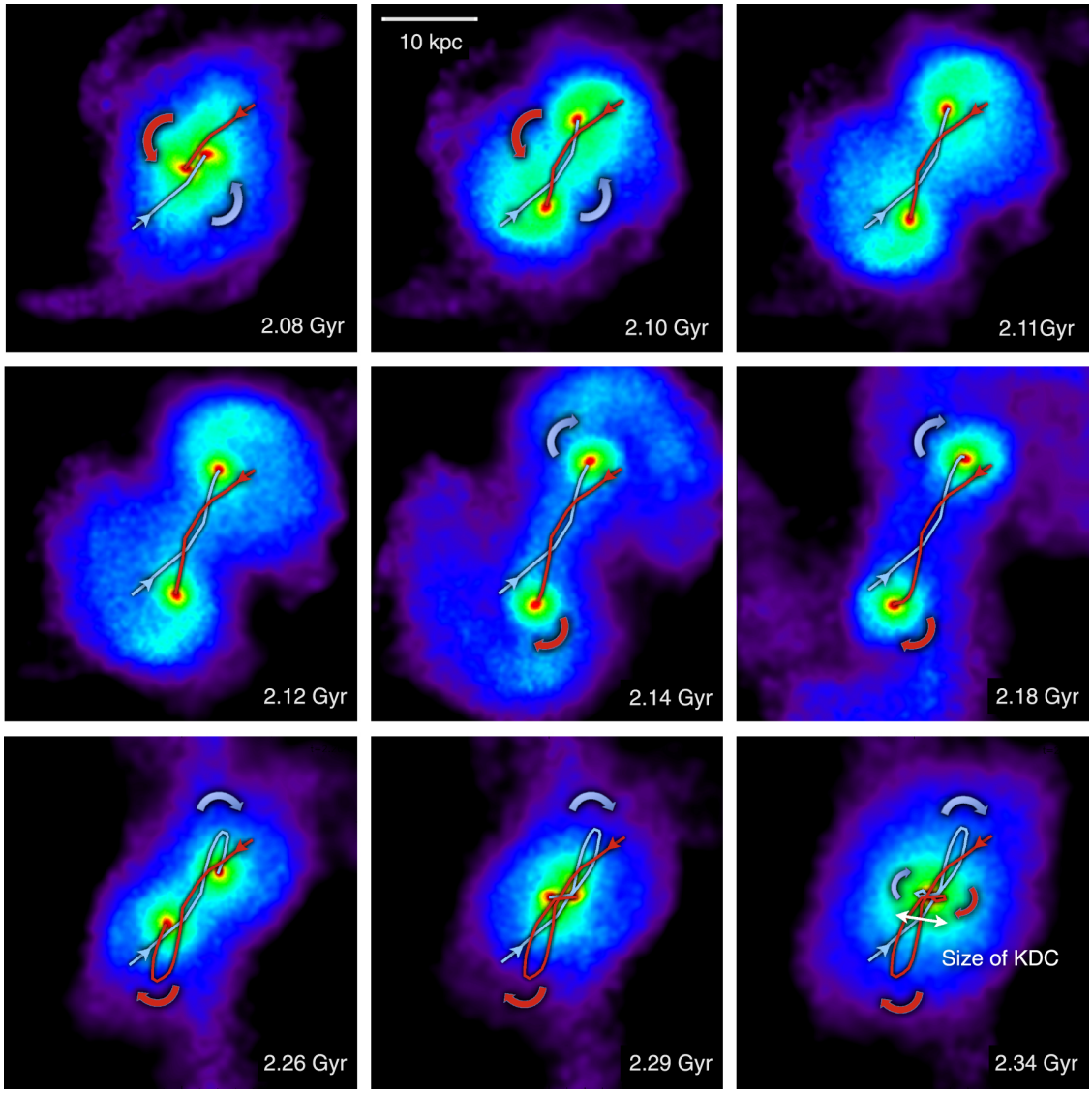

Figure 2.8: Stellar surface density of the two progenitor galaxies after their second pericentric passage (2.08 Gyr) where the orbital spin changes sign. During this time, strong tidal interactions acting upon the two progenitors result in short-lived trailing spiral arms (2.08-2.18 Gyr), along which loosely bound material gets ejected from their main bodies. This results into a strong reactive force that causes the two galaxies to change their orbital spin and follow retrograde trajectories until their final coalescence at t$\sim$ 2.4 Gyr. The width of the last oscillation before coalescence corresponds to the size of the KDC in the final merger remnant. Images were created with SPLASH (Price 2007). Adapted from Tsatsi et al. 2015.

show global counter-rotation in the post-merger kinematics (Figure 2.5): these stars, more tightly bound in the centers of the galaxies during their close encounters, can track the behavior of the orbital spin of their progenitors' center of mass before coalescence.

On the other hand, the outer parts of the galaxy keep the initial prograde spin. Gas and stars ejected during the merger are subsequently re-accreted, while inheriting the outer prograde spin, forming the prograde-rotating outer part of the remnant.

We suggest that the Mestschersky force is present in every stage of the merger. We interpret the change of sign of the orbital angular momentum near the first apocenter α_1, as a result of this force (Figure 2.5), which is also seen as a change of curvature of the two merging orbits near α_1 in Figure 2.6. However, at this time in the merging process the effect is not strong enough to change the orbital spin.

2.4 Conclusions and Discussion

We have shown that a KDC in an early-type galaxy can result from an initially prograde major merger of two disk galaxies. This finding is in contrast to the commonly suggested idea that KDC formation can only result from retrograde mergers. We show the plausibility of an orbital reversal of a prograde merger, caused by reactive forces that act upon the two progenitors due to mass loss, which results in KDC formation in the final merger remnant.

The KDC that resides in the center of the remnant shows strong counter-rotation for more than 2 Gyr after the final coalescence of its progenitors. The KDC is most prominent in the old stellar population of the galaxy (ages > 5 Gyr) and is large in size (2 kpc radius), making it consistent with observations of KDCs in massive ETGs (McDermid et al. 2006) and comparable to the observed CRC/2-σ galaxies (Krajnović et al. 2011). The fact that it results from an initially prograde merger provides a new channel for KDC formation that can add to the predicted rate of occurrence of KDCs and help towards explaining their observed high fraction in ETGs.

The suggested formation scenario depends on reactive (Mestschersky) forces, that act upon the progenitors due to mass loss during the merger, causing the reversal of the orbital spin. Since prograde mergers result in substantial mass loss compared to retrograde mergers (Toomre & Toomre 1972; Barnes 1988), we expect that such an effect is more likely to occur in prograde mergers. We would also expect this effect to depend on the mass ratio, the initial inclination, as well as the structural properties of the progenitor galaxies. Resolution effects in the simulations might also influence properties of the KDC, such as its size and its position angle (e.g. Bois et al. 2010).

Using the merger simulations presented in Moster et al. (2011), we note that the formation of the KDC does not depend on the particular form of feedback used or to the hot and cold gas employed in the progenitor galaxies.

The suggested Mestschersky mechanism in galaxy encounters, as well as the possibility of orbital

reversals during mergers and their effects on the dynamical structure of the resulting remnants has yet not been widely recognized. Barnes (2016) recently found such orbital reversals in close galaxy encounters, that can occur even after the first pericentric passage of the two galaxies, and explained this by means of dynamical reflections of their central bulges caused by torques exerted from their two interpenetrating dark matter halos. In our case, the dark matter halos themselves suffer the same orbital reversal as their bulges after the second pericentric passage.

Nevertheless, both the results from Tsatsi et al. (2015) and Barnes (2016) show that the final encounters of merging systems can involve complex orbital dynamics and orbital reversals, that cannot be explained just by dynamical friction. A larger statistic of merger simulations may eventually assess the implications of these findings on the dynamical structure of merger remnants in a statistical sense, and show how common this new channel for KDC formation is in early-type galaxies.

Chapter 3

The Merger Origin of Prolate Rotation in Early-type Galaxies

An early-type galaxy's (ETG) rotation does not necessarily coincide with its flattening. As discussed previously (*Chapters 1 and 2*), elliptical galaxies can show a variety of kinematic peculiarities, such as kinematically decoupled cores, or, in general, kinematic twists and misalignments. While most observed galaxies appear to rotate around their minor apparent axis, some ETGs show rotation around their major axis, so called "prolate rotation"[1]. This feature is considered to be indicative of their triaxial/prolate shape.

While prolate rotation in elliptical galaxies is a dynamically stable configuration, its origin is still unclear and observations of prolate rotators are very rarely found in the literature. Here we present a sample of 10 early-type prolate rotating galaxies from the CALIFA Survey (9 of which were not previously known to be prolate rotators), adding a significant fraction to the number of galaxies that show such a kinematic feature in their stellar kinematics. We investigate the origin of such systems, using *N*-body simulations of galaxy mergers and show that prolate rotators can be the end-products of major polar mergers. Our findings are presented in Tsatsi et al. 2016b, *to be submitted*.

3.1 Triaxiality and Prolate Rotation

Almost 60 years have passed since Contopoulos (1956) suggested that the intrinsic shape of elliptical galaxies could be triaxial. Since then, it has been established that the existence and persistence of triaxial galaxies is theoretically permitted (e.g. Aarseth & Binney 1978; Binney 1985). If elliptical galaxies are such systems, they are expected to show two types of stable stellar rotation; rotation around their short axis (short axis tube orbits), as in the typical case of oblate systems (oblate rotation), as well as rotation around their long axis (long-axis tube orbits), or prolate rotation (see Figure 1.5).

This suggests that any observations of an undisturbed elliptical galaxy that shows rotation around its major apparent axis is indicative of its triaxial shape. However, several attempts to find such systems have been unsuccessful in the past (e.g. Bertola et al. 1988) and until now, only a few observations of

[1]Note: "Prolate rotation" is often referred to as "long axis" rotation, or "minor axis" rotation, the latter meaning a velocity gradient along their projected minor axis.

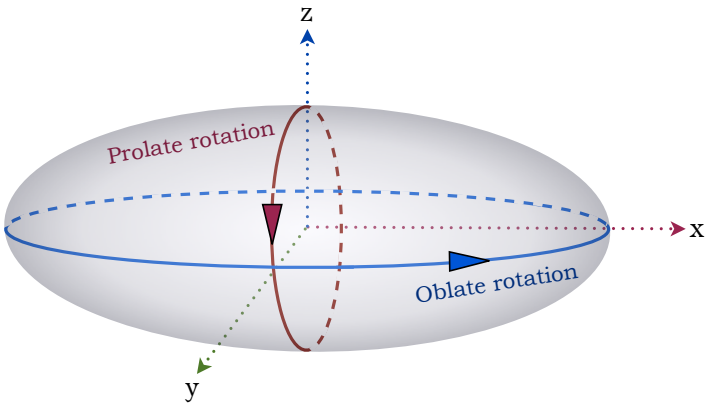

Figure 3.1: Schematic diagram of the two types of dynamically stable rotation in a triaxial potential: Rotation around the short (z) axis (oblate rotation) consisting of short axis tube orbits, and rotation around the long (x) axis (prolate rotation), consisting of long-axis tube orbits. Rotation around the intermediate (y) axis is unstable.

galaxies with clear prolate rotation exist. These cases concern: NGC 1052 (Schechter & Gunn 1979; Davies & Illingworth 1986), NGC 4406, NGC 5982, NGC 7052, NGC 4365, NGC 5485 (Wagner et al. 1988), NGC 4261 (Davies & Birkinshaw 1986; Wagner et al. 1988), NGC 4589 (Wagner et al. 1988; Moellenhoff & Bender 1989), AM 0609-331 (Moellenhoff & Marenbach 1986) and M87 (Davies & Birkinshaw 1988; Emsellem et al. 2014), totalling 10 objects[2].

Out of these 10 ETGs that are reported as prolate rotators in the literature, 3 galaxies (NGC 4589, NGC 5485 and AM 0609-331) show strong dust lanes along their minor axes, while most of them are members of groups or clusters.

Only for 5 of these 10 known prolate rotating ellipticals, two-dimensional integral field unit (IFU) spectroscopy of the stellar kinematics has been carried out so far: NGC 4261, NGC 5485, NGC 4365, NGC 4406 and M87 (Davies et al. 2001; Emsellem et al. 2011; Krajnović et al. 2011; Emsellem et al. 2014). Their study revealed that the main-body prolate rotation of these galaxies may coexist with short axis rotation, often in the form of a kinematically decoupled component (KDC).

While the dynamical stability of prolate rotation in triaxial galaxies has been extensively studied theoretically, the formation origin of such systems is yet elusive. As the known cases of prolate rotators reported so far seem to belong in the potential wells of groups or clusters of galaxies, their formation origin is likely to be merger-driven.

Massive ellipticals of stellar mass $M_* \gtrsim 10^{11}\,M_\odot$ appear to have gradually built up their mass by a factor of two since $z \sim 2$, with the growth mostly affecting their outer regions ($r > r_e$) (van Dokkum et al. 2010; Pérez et al. 2013). This is in favor of a *"two-phase assembly"* formation scenario, where the central regions of the most massive elliptical galaxies have been formed early on by a gas rich

[2]Note: There is also evidence for (although not clear) prolate rotation in NGC 2749, IC 179 (Jedrzejewski & Schechter 1989) NGC 3923 (Carter et al. 1998) and NGC 7626 (Davies & Birkinshaw 1988).

major merger at $z \sim 2$, followed by a prolonged period of dry minor mergers. This picture is in line with observations of most ellipticals (Cappellari 2013) that show an oblate rotating central structure, embedded in an extended, more spherical, and more slowly rotating outer structure (Arnold et al. 2014).

However, in the case of ellipticals that show strong prolate rotation in their central regions, it is not clear how the above picture could form a triaxial inner structure with no (significant) oblate rotation. It is possible that the two-phase assembly scenario, where the central region was formed by a major merger still holds for this special case of prolate rotators: Naab & Burkert (2003) showed that the amount of prolate rotation in the remnant of a 1:1 merger is stronger than in unequal-mass merger remnants. However, Cox et al. (2006), showed that dissipational, equal-mass disk mergers result in merger remnants with stronger oblate rotation.

Given the motivations above, it is most likely that the inner regions of present-day massive ellipticals that show strong prolate rotation and no (significant) oblate rotation, were formed preferentially by gas-poor major mergers. However, assuming that such systems are formed by mergers, it is not clear why they are so rarely observed.

3.2 New Evidence from Observations

Motivated by all the above evidence, we have made use of the Calar Alto Legacy Integral Field Area (CALIFA) survey (Sánchez et al. 2012), which provides IFU data for a statistically well defined sample of ~600 galaxies across the Hubble sequence, in order to search for possible prolate rotating elliptical galaxies.

The CALIFA sample is selected from a Mother Sample of 938 galaxies in the photometric catalogue of the 7th data release (Abazajian et al. 2009) of the Sloan Digital Sky Survey (SDSS), with the main selection criteria to be their angular isophotal diameter ($45'' < D_{25} < 80''$), and a redshift range of $0.005 < z < 0.03$. The survey uses the PPAK IFU (Verheijen et al. 2004; Kelz et al. 2006) of the Potsdam Multi-Aperture Spectrograph, PMAS (Roth et al. 2005) at the 3.5 m telescope of CAHA, with a Field-of-View (FoV) that can extend up to several effective radii (r_e) using two different setups (V500 and V1200) of resolutions R~850 and R~1650, respectively. For a more detailed description of the CALIFA survey and extraction of stellar kinematics, see Walcher et al. (2014); Falcón-Barroso et al. (2016).

In this work we focus on observations of the following 10 ETGs from the CALIFA Survey. Our sample consists of 9 ETGs drawn from the CALIFA 3rd Data Release[3] (DR3) sample of 667 galaxies: LSBCF560-04, NGC 0647, NGC 0810, NGC 2484, NGC 4874, NGC 5216, NGC 5485, NGC 6173 and NGC 6338, as well as NGC 5794, an ETG from the CALIFA Mother Sample which is not part of the DR3. Some of their qualitative properties, including their Hubble types, group memberships, distances, stellar masses and effective radii are shown in Table 3.1.

[3] See Sánchez et al. 2016 for a detailed description of the 3rd Data Release of CALIFA.

Name	Type/Membership	d	M_*	r_e
		Mpc	(10^{11} M$_\odot$)	(kpc)
LSBCF560-04	E5/BCG	238	7.1 ± 0.6	17.9
NGC 0647	E7/in group	184	3.7 ± 0.3	8.7
NGC 0810	E5/in pair	110	6.1 ± 0.6	9.3
NGC 2484	E4/BCG	192	5.0 ± 0.5	12.5
NGC 4874	E0/BCG	102	3.7 ± 0.3	12.4
NGC 5216	E0/in pair	42	0.35 ± 0.03	4.1
NGC 5485	E5/in group	27	0.63 ± 0.06	4.1
NGC 5794	S0/in group	59	–	–
NGC 6173	E6/BCG	126	9.5 ± 0.9	30.5
NGC 6338	E5/BCG	117	5.5 ± 0.5	17.0

Table 3.1: Properties of prolate rotators in CALIFA DR3[4]: Col.1: Name. Col.2: Hubble type from Walcher et al. (2014)/ group membership (NED/SIMBAD). Col.3: Redshift-based distance in Mpc. Col.4: Stellar mass, as estimated from WISE photometry by Norris et al. (2016). Col.5: Effective radius, determined by growth curve analysis of SDSS images of each galaxy as in Walcher et al. (2014).

[4]*As NGC 5794 is not part of CALIFA DR3, some of its structural properties are not included in this table.*

Out of these 10 galaxies, 6 belong to the CALIFA kinematic sub-sample of 82 ETGs (∼ 300 galaxies in total), described in Falcón-Barroso et al. (2016), a statistically well-defined sample, which is representative of the CALIFA Mother Sample of 938 galaxies across the Hubble sequence.

We derived our stellar kinematics maps following the strategy described in Falcón-Barroso et al. (2016). However, there are a few differences that we adopted in our work. We used the CALIFA V500 data set only, as these observations typically reach fainter magnitudes and this way we are able to better recover the stellar kinematics in the outer parts of the galaxies. In order to reliably measure the higher order Gauss-Hermite terms h_3 and h_4, we binned the data to S/N∼40 using the Voronoi binning technique as implemented by Cappellari & Copin (2003). Then we used a subset of ∼330 stars from the IndoUS library (Valdes et al. 2004, the same set as in Falcón-Barroso et al. 2016), and fitted the binned spectra in the wavelength range 4250.0 – 5500.0 Å.

In this way we extracted the stellar kinematics shown in Figures 3.2 and 3.3. The CALIFA maps reveal strong prolate rotation for all 10 galaxies, of amplitudes ranging from ∼ 60 to 100 km/s. In all cases we find strong kinematic evidence for triaxiality, as the stellar rotation of the main body of the galaxy is prolate (around the major apparent axis). In the case of NGC 6338 the rotation is prolate only in its inner parts, while the outer parts show oblate rotation– a new case of an elliptical galaxy with a prolate kinematically decoupled component. It is interesting to note that almost all of

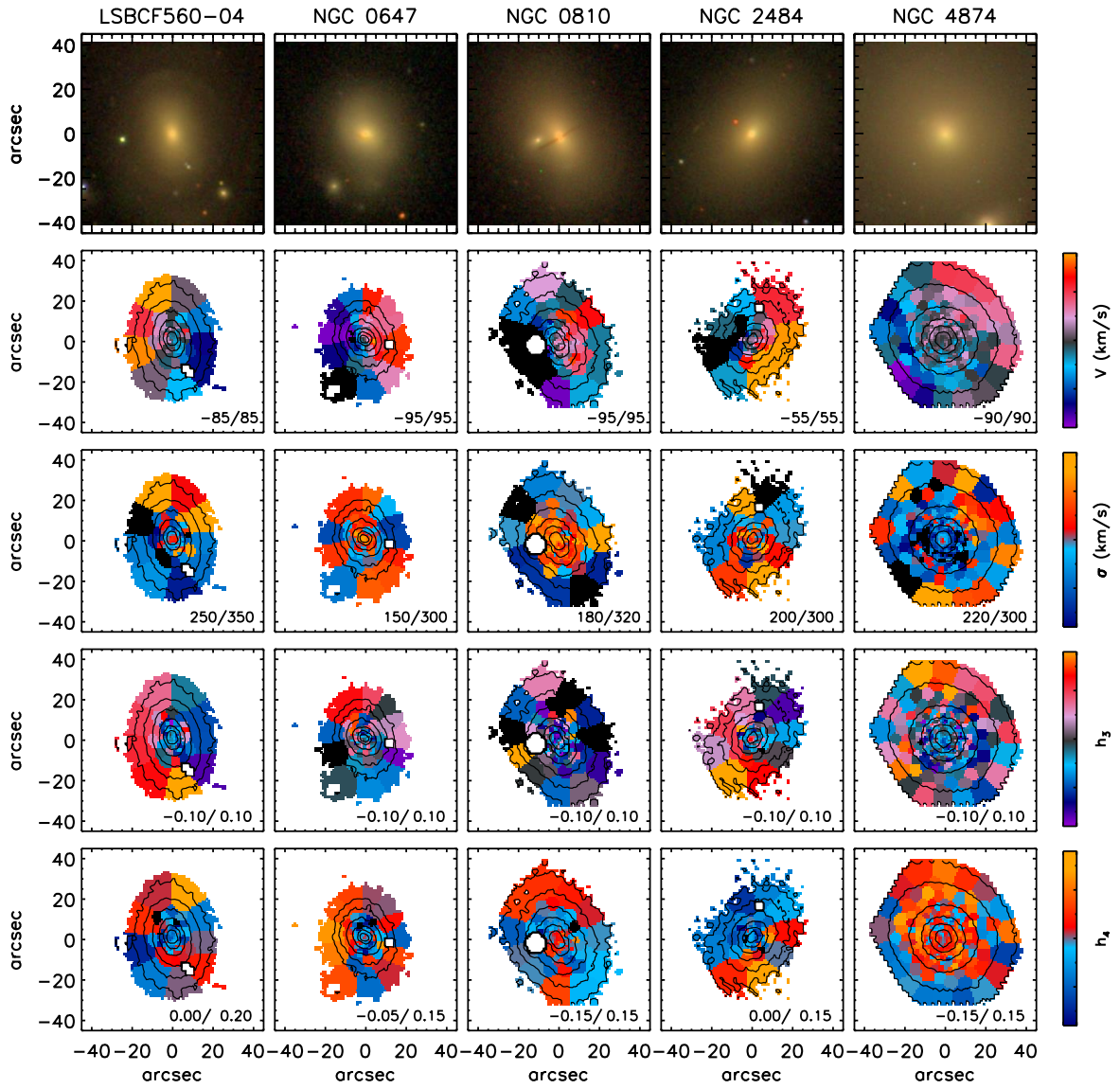

Figure 3.2: *From left to right:* LSBCF560-04, NGC 0647, NGC 0810, NGC 2484 and NGC 4874, 5 galaxies from the CALIFA sample of 10 prolate rotators (see Figure 3.3 for the remaining 5 galaxies). *From top to bottom:* Color-composite SDSS image of each galaxy, stellar line-of-sight velocity V, velocity dispersion σ in km/s, and the higher order moments h_3 and h_4 extracted from the V500 CALIFA dataset for each galaxy. The range of values for every kinematic parameter shown in the color maps is denoted at the bottom-right corner (Tsatsi et al. 2016b, *to be submitted*).

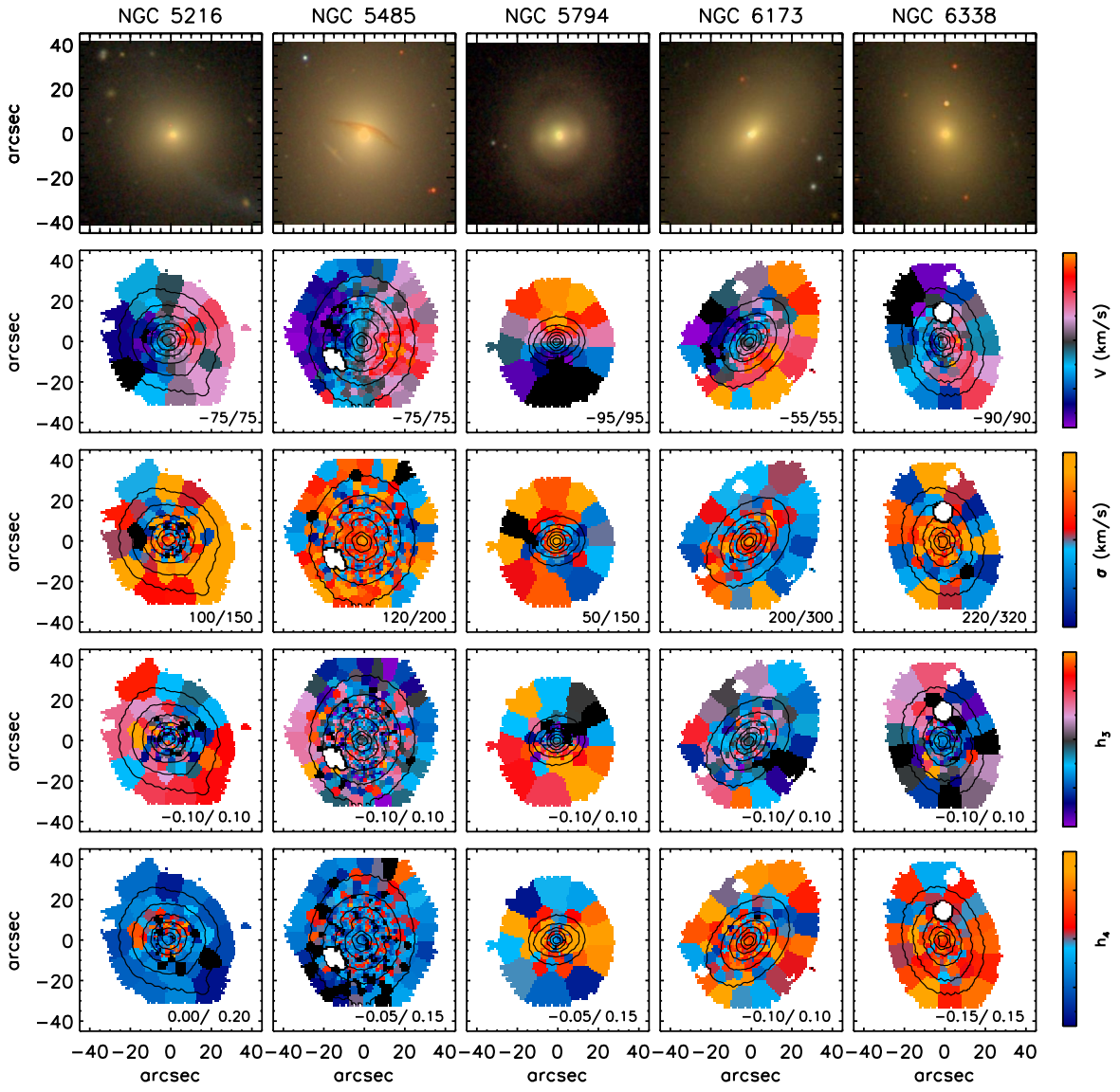

Figure 3.3: *From left to right:* Same as Figure 3.2 for NGC 5216, NGC 5485, NGC 5794, NGC 6173 and NGC 6338, from the CALIFA sample of 10 prolate rotators. *From top to bottom:* Color-composite SDSS image of each galaxy, stellar line-of-sight velocity V, velocity dispersion σ in km/s, and the higher order moments h_3 and h_4 extracted from the V500 CALIFA dataset for each galaxy. The range of values for every kinematic parameter shown in the color maps is denoted at the bottom-right corner (Tsatsi et al. 2016b, *to be submitted*).

the galaxies in our sample belong in groups or clusters. Five out of ten are the brightest galaxies in their clusters (BCGs), with relatively high stellar masses ($M_* \gtrsim 10^{11}$ M$_\odot$).

One can also see that two prolate rotators of our sample show strong dust lanes along their minor photometric axis in their SDSS images (Figures 3.2 and 3.3). These galaxies include NGC 5485, a known case of an ETG with prolate rotation and a minor axis dust lane (Wagner et al. 1988; Emsellem et al. 2011), as well as the new case of NGC 0810.

Assuming that dust and gas settle in the principal planes of a galaxy, the existence of a minor axis dust lane is the visual evidence for triaxiality (Bertola & Galletta 1978; Merritt & de Zeeuw 1983). We expect that the 10 prolate rotators of our sample must be, to some extent, triaxial or prolate.

Considering the rarity of observations of such systems so far, their formation origin is still poorly understood. It is likely that prolate rotation may not be as rare as previously thought. Our findings present 6 prolate rotators out of 82 ETGs ($\sim$ 7%) in a statistically well defined sample (CALIFA kinematic sample, as described in Falcón-Barroso et al. 2016) of 300 galaxies across the Hubble Sequence (for the CALIFA Main Sample, the statistics are best for galaxies with stellar masses around $10^{10.8}$ M$_\odot$, see Walcher et al. 2014 and Sánchez et al. 2016). This fraction is much higher than in the volume-limited ATLAS^{3D} Survey, where only 2 out of 260 ETGs ($\sim$ 0.8%) were found to exhibit prolate rotation (Emsellem et al. 2011).

What are the implications of these findings for the formation of such systems? Could prolate rotators be the end-products of major mergers? According to the two phase-assembly scenario, the central parts of ETGs have been preferentially assembled through gas-rich major mergers approximately $\sim$10 Gyr ago. However we do not observe clear signs of oblate rotation in most of the prolate rotators presented here from CALIFA. This suggests that for this special type of objects their merger origin might have been rather gas-poor. In what follows, we explore the dynamical structure of remnants resulting from such a formation scenario.

3.3 New Evidence from Simulations

We investigate a possible merger origin of prolate rotation, by studying simulated early-type galaxies formed in N-body simulations of binary disk mergers, and extracting mock IFU observations of their stellar kinematics.

We show that polar mergers can produce prolate-shaped merger remnants with strong rotation around their major axis, which could be the progenitors of the observed present-day prolate rotating galaxies. Such a formation scenario is in agreement with the existing picture of a two-phase assembly of ETGs and can explain the rarity of observations of prolate rotators as a natural consequence of the infrequency of major polar mergers.

Name	Progenitor B/T	r_{hm} (kpc)	b/a	c/a	T
M0	0.00	16.00	0.57	0.51	0.91
M1	0.10	14.83	0.57	0.47	0.87
M2	0.30	12.42	0.61	0.51	0.84
M3	0.50	9.90	0.63	0.50	0.81
M4	0.70	7.11	0.55	0.43	0.85

Table 3.2: Properties of the simulated remnants: Name, mass ratio between bulge and total mass of each progenitor B/T, half-mass radius r_{hm}, axial ratios b/a, c/a and triaxiality parameter T (see Equation 3.1) of the simulated remnants, estimated within r_{hm}.

3.3.1 Simulations of Polar Galaxy Mergers

The simulations we use were performed using a modified version of the TreeSPH-code Gadget-2 (Springel 2005) described in *Chapter 2*, GADGET-3[5]. In order to investigate the gas-poor merger scenario of prolate galaxies, our simulations do not include cold or hot gas (hence our simulations are N-body).

The two progenitor disk galaxies are identical and they are composed of a stellar disk and a stellar bulge, which are embedded in a dark matter halo. The disk of one of the progenitor galaxies is always aligned with respect to the orbital plane, while the other progenitor has its disk inclined by 90° with respect to the orbital plane.

We run 5 realizations of the simulation described above, with different bulge-to-total stellar mass ratios (B/T) of the progenitor galaxies. We adopt a range of B/T ratios of 0.0, 0.1, 0.3, 0.5 and 0.7 (see Table 3.2). All the simulations have the same number of stellar and dark matter particles (N=2 425 432), so that the each merger remnant has a stellar mass of $M_* = 2.6 \times 10^{11}$ M$_\odot$ and a dark matter halo of $M_{dm} = 1.6 \times 10^{13}$ M$_\odot$. The two progenitor galaxies initially evolve in isolation for 2 Gyr. After they evolve, the merger simulation starts and lasts for approximately 8 Gyr.

We note here that the estimated stellar mass of some of the observed prolate rotators in the CALIFA sample (especially for the BCGs) is a factor of two larger than in our simulations. We assume that our simulated galaxies are likely to be the progenitors of such galaxies, which, as discussed previously, after their first major merger phase are expected to grow in mass and size by minor mergers. However this process will have an effect mainly in their outer parts (e.g. van Dokkum et al. 2010) and we would expect that it would not influence significantly the central stellar kinematics of the remnants we are interested to investigate here.

[5]A public release of the GADGET-3 code is not yet available.

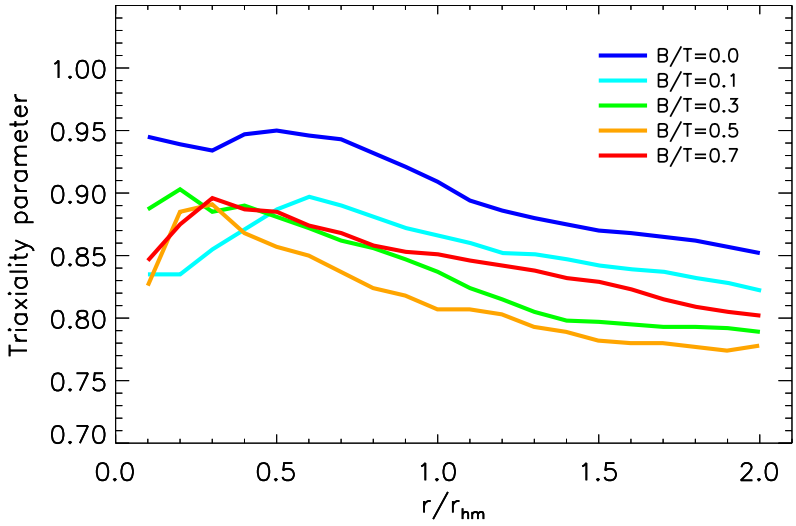

Figure 3.4: Triaxiality parameter T as a function of distance from the center for each simulated merger remnant of Table 3.2. Different colors correspond to the different B/T ratios of their progenitors (Tsatsi et al. 2016b, *to be submitted*).

3.3.2 Shape and Kinematics of the Simulated Prolate Galaxies

In order to connect the intrinsic mass and orbital distribution of our simulated galaxies with observable properties, we create two-dimensional mock stellar mass and stellar kinematic maps as follows.

Stellar particles are projected along a chosen viewing angle and then binned on a regular grid centered on the baryonic center of mass of the galaxy. We adopt a grid size of 20 $\times$20 kpc^2 and a pixel size of 0.5 kpc, which corresponds to the spatial resolution of CALIFA ($\sim$1$''$), assuming that our simulated galaxies are observed at a distance of $\sim$100 Mpc. The bulk velocity of the galaxy is estimated within a sphere of 50 kpc around the center and subtracted from all particle velocities. Each stellar particle in our simulations correspond to different masses, hence we extract mass-weighted kinematic maps for each galaxy. These maps are then spatially binned using the 2D Voronoi binning method (Cappellari & Copin 2003), based on a minimum number of particles per pixel in the map. Signal corresponds to the number of particles per pixel and we adopt Poisson noise, such that our signal-to-noise ratio per bin corresponds approximately to an average target value of $S/N \sim 35$ for all the remnants.

The mass-weighted stellar line-of-sight velocity distribution (LOSVD) is then extracted for every Voronoi bin and fitted with the Gauss–Hermite series (van der Marel & Franx 1993), as implemented by van de Ven et al. (2006, see Appendix) allowing us to retrieve the Gauss–Hermite parameters of the LOSVD (V, σ, h_3, h_4) of the final merger remnants.

The shape properties of the final merger remnants are shown in Table 3.2. The remnants become more compact as the B/T of their progenitors increases and their half-mass radius decreases.

Figure 3.4 shows, as a function of distance from the center of each remnant, the triaxiality parameter

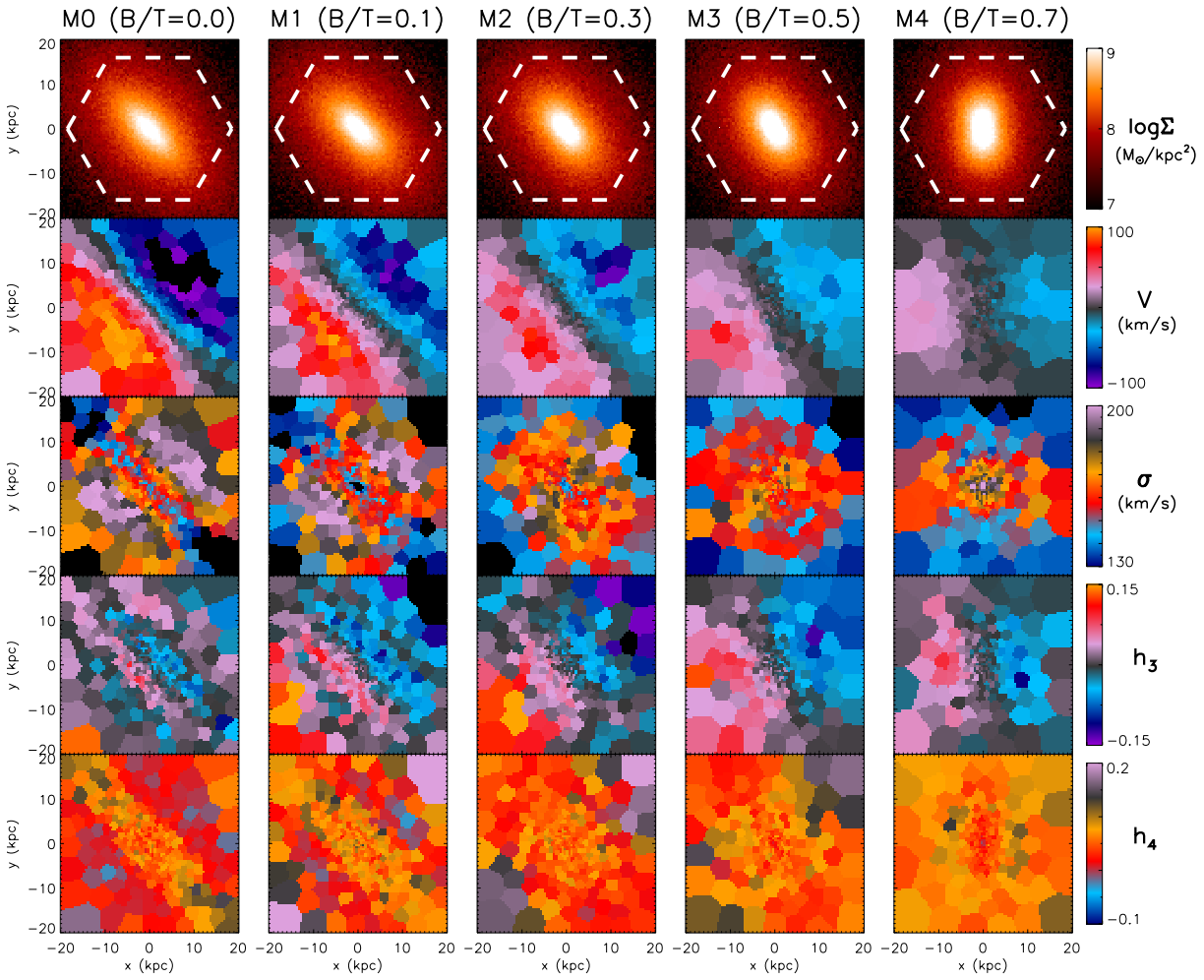

Figure 3.5: Stellar mass and line of sight orbital distribution of the simulated merger remnants M0-M4 (the B/T ratio of their progenitors increases from left to right). The projected plane x-y corresponds to the orbital plane of the merger. From top to bottom: Mass surface density $\log \Sigma$ and Gauss-Hermite moments fitted to the LOSVD: V, σ, h_3 and h_4. The CALIFA field of view for the assumed distance is overplotted on the mock images of the first row (Tsatsi et al. 2016b, *to be submitted*).

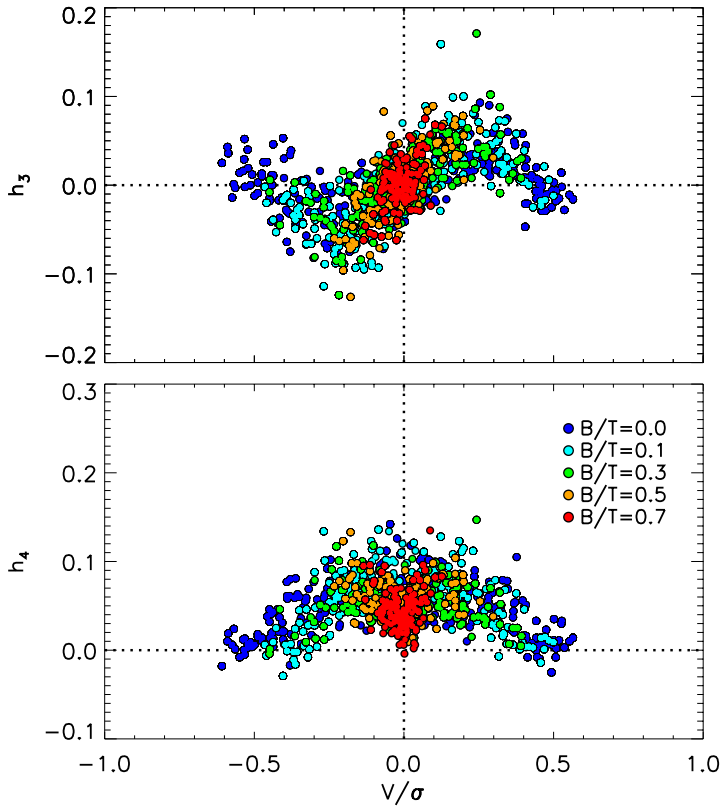

Figure 3.6: Pixel values within r_{hm} of h_3 (upper panel), h_4 (bottom panel) versus V/σ extracted from the simulated kinematic maps for all the simulated remnants of Figure 3.5. Different colors correspond to the different B/T ratios of their progenitors (Tsatsi et al. 2016b, *to be submitted*).

T, defined as:

$$T = \frac{1-(b/a)^2}{1-(c/a)^2} \tag{3.1}$$

with a>b>c the principal axes of the ellipsoid, which are computed by extracting the eigenvalues of the mass tensor within spherical shells of radius r for each remnant. For oblate ellipsoids T=0 and for prolate ellipsoids T=1. We see that all our simulated remnants are highly prolate within two half-mass radii, with T>0.8. For radii r>r_{hm} there appears to be a trend of lower T with increasing B/T ratio of the progenitors, except for remnant M4, which corresponds to the highest B/T progenitor ratio.

The projected stellar mass, mean velocity and velocity dispersion of all the final merger remnants are shown in Figure 3.5. All the remnants show prolate rotation, with amplitude depending on the initial B/T ratio of their progenitors. A lower B/T ratio of the progenitors results in remnants with stronger prolate rotation, with a maximum amplitude of ∼100 km/s in the case of two bulgeless progenitors (B/T=0).

The velocity dispersion shows two double peaks along the minor photometric axis and a central dip for the bulgeless case. As the progenitor B/T ratio increases, the double peaks become weaker and the central dip becomes a central peak.

Figure 3.5 shows that for all our simulated remnants the skewness of the LOSVD (h_3) and V/σ are correlated. Krajnović et al. (2008) found that fast rotators show two different trends: a strong anticorrelation of h_3 with large values of V/σ, indicative of the existence of a disk component, or an h_3 that is close to zero, and shows positive correlation at intermediate V/σ, suggesting that this must be the result of minor axis contamination. Naab et al. (2014) suggested that the two trends observed can be linked to their assembly history, and showed that dissipational mergers can lead to a strong h_3-V/σ anticorrelation, while gas-poor major mergers can result in fast rotators with no h_3-V/σ correlation.

The quality of the CALIFA data is not enough in order to measure robustly the higher order moments h_3 and h_4. Better quality data would be needed to show the relation between the stellar LOS velocity and h_3 in the observed prolate rotators. Higher quality IFU observations (e.g. with instruments such as MUSE, Bacon et al. 2010) will help us to further assess the implications of these findings and place additional constraints on the gas fraction of the progenitors of these systems.

Finally, we find that the triaxial merger remnants also exhibit figure rotation on the orbital plane. This figure rotation is caused either by torques exerted from the triaxial dark matter halo, or/and by angular momentum transfer from the stellar component that is expelled during the merger and gets subsequently re-accreted onto the main stellar halo. The direction of the figure rotation is the same as the orbital direction of the merger and coincides with its flattening. In principle, such tumbling motion in triaxial systems may reflect to an observed oblate rotation of the system, which in projection might feign as an intrinsic rotation of its stars. However in our simulations we find that the tumbling motion is very slow, and, as an example in the case of simulation M4 the long axis of the remnant completes one full rotation in approximately 4 Gyr. As a result, this motion is not observationally distinct in the mock kinematics of our remnant.

3.3.3 Origin of Prolate Rotation

In order to understand better the origin of prolate rotation, we separate the LOSVD of the stellar particles in each remnant according to their formation origin, by selecting the particles that initially formed the disks and the bulges of the two progenitors.

Figure 3.7 shows, for remnant M4, that only the particles that initially belonged to the progenitor that had its disk inclined by 90° with respect to the orbital plane of the merger (Progenitor I) show strong prolate rotation in the final merger remnant, with an amplitude of ~200 km/s. These particles account for less than 15% of the total mass of the galaxy in this particular simulation set-up. The particles that initially formed the disk of the progenitor whose disk was aligned with the orbital plane (Progenitor II) are more dispersed and show very weak rotation around the apparent minor axis of the remnant (oblate rotation). The rest of the stellar particles of the remnant that initially formed the bulges of the two progenitors show no rotation. This implies that stellar populations that contribute

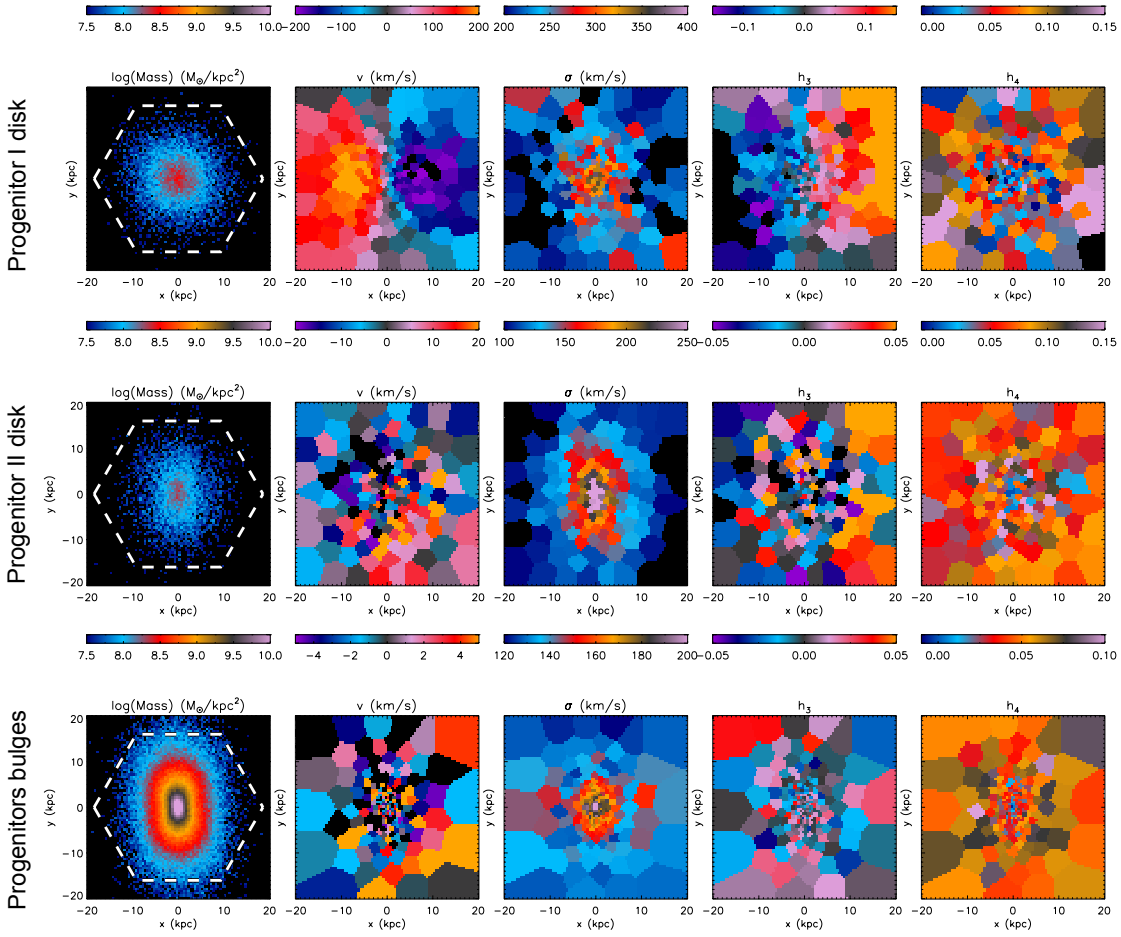

Figure 3.7: LOSVD of the stellar particles of merger remnant M4 in the same projection as in Figure 3.5, where we separate particles according to their formation origin. The first row shows the stellar kinematics of the merger remnant only for particles that initially belonged to the disk of Progenitor I (that was inclined by 90° with respect to the orbital plane) and show strong prolate rotation in the remnant. The second row shows the same for the particles that initially formed the disk of Progenitor II and show weak rotation around the apparent minor axis of the remnant, while the third row shows the rest of the stellar particles of the remnant (initially forming the progenitors bulges), that show no rotation (Tsatsi et al. 2016b, *to be submitted*).

mainly to the prolate rotation are only a small fraction of the total stellar mass of the galaxy.

This result is in agreement with findings for NGC 4365, a well-studied elliptical galaxy that shows prolate rotation in its outer parts with an amplitude of ∼60 km/s (Davies et al. 2001). State-of-the-art orbit-based dynamical modeling[6] of this galaxy, shows that its long-axis tube orbits show an amplitude of stellar rotation which is larger than ∼150 km/s, although contributing only ∼20% to the total stellar mass of the galaxy (van den Bosch et al. 2008).

We see that the stars contributing to the prolate rotation in our simulations retain memory of their initial orientation in their progenitor's disk prior to the coalescence of the two progenitors. This result is in agreement with the findings from *Chapter 2*, where we have shown that stars that counter-rotate in the center of a merger remnant retain memory of the orbital spin reversal of their two progenitor galaxies prior to coalescence. Globally, our findings show that the orbital parameters and dynamics of major mergers prior to final merging are one of the main drivers of the dynamical nature of their remnants.

3.4 Conclusions and Discussion

We present 10 ETGs from the CALIFA Survey that show large-scale prolate rotation (rotation around the major photometric axis) in their stellar kinematics. This sample includes the discovery of 9 new prolate rotators, adding a significant fraction to the cases known in the literature. We investigate their possible merger origin by studying the stellar kinematics of elliptical merger remnants using *N*-body simulations of major polar galaxy mergers. Our results can be summarized as follows:

(i) Most of the 10 prolate rotating galaxies presented here appear to belong to galaxy groups or clusters. Some of them are BCGs (Brightest Cluster Galaxies). Two of them show distinct minor axis dust lanes (NGC 0810 and NGC 5485). Together with the main stellar body prolate rotation, minor axis dust lanes are an additional evidence for triaxiality (Bertola & Galletta 1978; Merritt & de Zeeuw 1983). We suggest that the galaxies presented here are intrinsically triaxial systems.

(ii) Early-type galaxies with prolate rotation might be more common than previously thought: In the volume-limited ATLAS^{3D} Survey, only 2 out of 260 ETGs are prolate rotators (∼0.8%). We have so far detected 6 prolate rotators out of 82 ETGs in the CALIFA sub-sample of 300 galaxies as described in Falcón-Barroso et al. (2016), which is a fully representative sample of the CALIFA Mother Sample of 938 galaxies across the Hubble sequence. This implies that in a statistically well defined sample ∼7% of ETGs show prolate rotation. This fraction is unprecedentedly high and yields potential implications for ETG formation.

(iii) We investigate the merger scenario, according to which the central stellar body of a prolate rotator was formed by a major merger more than ∼10 Gyr ago. As for most of the CALIFA galaxies

[6]See Section 5.2.1 and Appendix for a detailed description of orbit-based dynamical modeling in early-type galaxies.

we see no evidence for oblate stellar rotation (rotation around the short axis), we suggest that their merger formation must have been gas-poor. We thus perform a set of dissipationless, *N*-body simulations of major polar mergers of galaxies and investigate the dynamical structure of their resulting remnants. We find that such remnants exhibit highly prolate shapes, with a triaxiality parameter T>0.8 within 2 half-mass radii. All remnants show strong prolate rotation that depends on the B/T (bulge-to-total stellar mass) ratio of their progenitor galaxies. The higher this ratio is, the lower the amplitude of prolate rotation in the resulting elliptical galaxies.

(v) By constructing mock IFU observations of their stellar kinematics, we find that all the simulated merger remnants show a double peak on their line-of-sight (LOS) velocity dispersion profile along the minor axis. As the B/T of the progenitors increases, the double peaks become weaker and a central peak in the velocity dispersion arises. We also find a positive correlation between their LOS velocity and the higher-order-moment h_3. This is in contrast with what is observed for ETGs with oblate rotation (Krajnović et al. 2008), and more likely originates from the fact that the remnants result from gas-poor mergers (Naab et al. 2014). Better quality observations are now needed in order to confirm the presence of such kinematic features in the observed prolate rotators.

(vi) We show that the prolate rotation in each simulated galaxy originates from the progenitor galaxy that had its disk in an orthogonal orientation with respect to the orbital plane prior to the merger. In that sense, the stars that account for the prolate rotation in the remnant retain the memory of their initial orientation prior to the merger.

The substantial fraction of prolate rotators in the CALIFA sample presented here, suggests that prolate rotating galaxies may be more common than previously thought. This result implies important information about the formation of ETGs, since these galaxies may have been formed initially by polar major mergers. We note that here we have investigated only mergers of two identical spiral galaxies with orthogonal disk orientations prior to the merger. Such orientations may indeed be infrequent, and we would expect that varying the initial relative inclinations of the two disks would change the resulting kinematics of the remnant.

However, similar merger simulations have been performed by Łokas et al. (2014); Ebrová & Łokas (2015), which involved dwarf-dwarf galaxy mergers. This formation scenario was suggested in order to explain the prolate rotation that was recently observed in the dwarf spheroidal galaxy Andromeda II (Amorisco et al. 2014), the first dwarf galaxy observed to show such a kinematic feature (Ho et al. 2012). Ebrová & Łokas (2015) found that a variety of initial conditions can result in remnants with prolate rotation. In line with their findings, we would expect that ETG prolate rotators may result from a variety of initial orientations of their progenitors disks, and that our fine-tuning of a strictly orthogonal orientation should not be considered as a limitation to the predicted fraction of prolate rotators. The dependance on the initial disk orientations and orientation is beyond the scope of this work, however we plan to investigate this further with the use of additional simulations.

In our simulations we find prolate remnant elliptical galaxies with a positive correlation between their LOS velocity and the higher-order-moment h_3. The quality of the CALIFA data is not sufficient

to measure robustly the higher-order moments in order to compare with findings from our merger simulations. These CALIFA ETGs would require further study with higher resolution observations from next generation IFS instruments (e.g. MUSE, Bacon et al. 2010) in order to assess further the implications of our findings.

In future work, we plan to investigate how varying the initial orbital and structural parameters of the two progenitor galaxies affects the shape and dynamics of the resulting prolate rotating remnants. This work, combined with higher quality observations of the sample of galaxies presented in this chapter will give better insights into the dynamical nature of this special type of rotators, and help towards setting better constraints on their formation origin as well as their rate of occurence.

Chapter 4

The Merger Origin of Nuclear Star Clusters

Nuclear Star Clusters (NSCs) are commonly observed in the centres of most galactic nuclei, including our own Milky Way. While their study can reveal important information about the build-up of the innermost regions of galaxies, the physical processes that regulate their formation are still poorly understood. NSCs might have been formed through gas infall and subsequent in situ star formation, and/or through the infall and merging of multiple star clusters into the centre of the galaxy.

As in the case of early-type galaxies, a possible merger origin of NSCs would be reflected by a complex present-day dynamical structure. In that sense, NSCs might be indeed much more similar, although on a smaller scale, to early-type galaxies. Recent findings suggest the existence of kinematic misalignments, decoupled regions in the stellar kinematics of NSCs, as in the case of the Milky Way NSC (Feldmeier et al. 2014), and even central counter-rotating stellar populations (e.g. Lyubenova et al. 2013; Seth et al. 2010) in extragalactic NSCs. As discussed in previous chapters, such features are commonly found in the stellar kinematics of early-type galaxies and are considered to be the direct, present-day observational evidence of their merger origin.

In this chapter we investigate these dynamical implications of a merger origin of NSCs. We find that merger remnant NSCs can show both morphological and kinematic properties that match very well observations of the Milky Way NSC, including significant rotation – a fact that has been so far attributed mainly to gas infall. We suggest that a merger origin is a viable hypothesis for the formation of rotating NSCs. These findings are presented in Tsatsi et al. 2016 (*in press*).

4.1 Observational Evidence

4.1.1 Extragalactic NSCs

Nuclear Star Clusters (NSCs) are massive and compact stellar clusters found in the central regions of most galaxies. With half-light radii of a few parsecs (e.g. Georgiev & Böker 2014) and typical dynamical masses of $10^6 - 10^7\,M_\odot$, they are thought to be the densest stellar systems in the Universe (Walcher et al. 2005).

Over the last decade, a series of studies have shown that NSCs are extremely common: more than

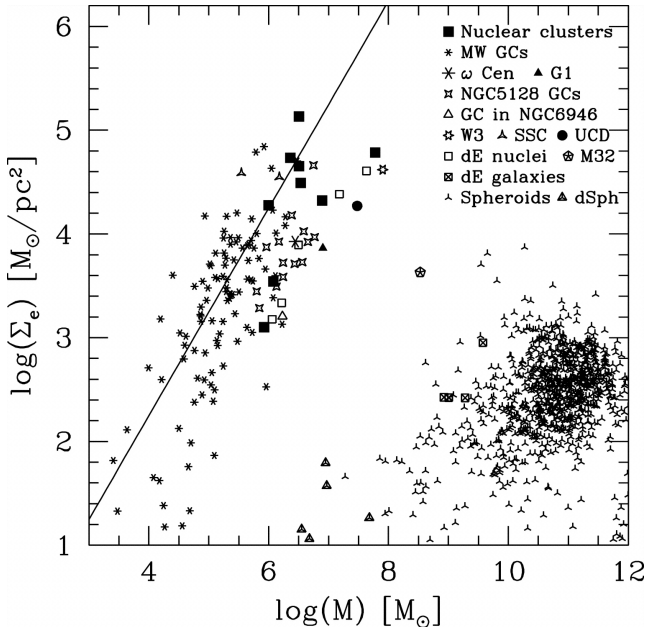

Figure 4.1: Mean projected mass density inside the effective radius $log(\Sigma_e)$ for various stellar systems, plotted against their total mass $logM$. Adapted from Walcher et al. (2005).

77% of late type galaxies host a NSC at their centre (Böker et al. 2002; Georgiev & Böker 2014), as well as at least 66% of early-type galaxies, mainly dwarf ellipticals and lenticulars (Côté et al. 2006; Turner et al. 2012; den Brok et al. 2014). Those fractions are only a lower limit to the true fraction of galaxies hosting NSCs, mainly due to several observational biases that limit their detection across the Hubble sequence. For example, NSCs are not detected in the most luminous early-type galaxies – this could be due to their very steep central surface densities that makes the detection of NSCs an observationally challenging task.

NSCs seem to correlate with global properties of their host galaxies. It has been suggested that the masses of NSCs and the masses of supermassive black holes (SMBHs) share similar-slope correlations with the host stellar velocity dispersion and bulge luminosity (Wehner & Harris 2006; Rossa et al. 2006; Ferrarese et al. 2006). However, a number of studies have questioned this similarity (e.g. Graham 2012; Erwin & Gadotti 2012; Scott & Graham 2013; Kormendy & Ho 2013). Although it is not clear if the formation and growth mechanisms of NSCs are coupled to that of SMBHs, they both seem to be connected with the formation and evolution of their host galaxies.

NSCs are similar to globular clusters (GCs), following a similar mass-density relation as the typical Milky Way GCs (see Figure 4.1, Walcher et al. 2005), however they are more luminous and more massive and compact. They typically show complicated star formation histories and their high luminosities arise partially from the young stellar populations that they are often observed to contain.

Their morphological and kinematic properties are strictly connected to their evolution. In general, NSCs are flattened and rotating systems, and they are usually found to be elongated to within $\sim 10^{\circ}$

with respect to the major axis of their host galaxy, as suggested from studies of NSCs in edge-on spirals (e.g. Seth et al. 2006).

In early-type galaxies, NSCs seem to show a complex dynamical nature, where corotating as well as counter-rotating stellar orbits are simultaneously needed to reproduce their observed kinematics, as the NSC of the elliptical galaxy FCC 277 (Lyubenova et al. 2013) and the NSC of the lenticular galaxy NGC 404 (Seth et al. 2010).

4.1.2 The NSC of our Milky Way

The nearest NSC that can be observed lies within the central 10 pc of our own Galaxy. Due to its proximity, the Galactic NSC can offer an excellent laboratory for studying the nature of these systems in extragalactic nuclei.

The Galactic NSC is centered precisely on Sgr A*, the location of Milky Way's massive black hole (MBH). The most recent measurements estimate the mass of the black hole to be $M_\bullet = 4.02 \pm 0.16 \pm 0.04 \times 10^6\,\mathrm{M}_\odot$, at a distance of $R_o = 7.86 \pm 0.14 \pm 0.04$ kpc (Boehle et al. 2016).[1]

The Galactic NSC and MBH lie within a larger stellar structure of mass $1.4 \pm 0.6 \times 10^9\,\mathrm{M}_\odot$. This structure is called the Nuclear Bulge (NB), which contains the NSC and the nuclear stellar disk, a large disk of scale height ∼45 pc, radius ∼230 pc, (Launhardt et al. 2002) and flattening $q = b/a = 0.28 \pm 0.02$ (Chatzopoulos et al. 2015a). All molecular gas in the central kpc of the Galaxy is often referred to as the Central Molecular Zone (CMZ). Figure 4.2 shows the CMZ and the NSC in the central region of our Milky Way.

Due to its proximity, the study of the morphology and the kinematics of the Milky Way NSC is of exceptional interest, as it can provide a very important tool to unveil the assembly process of the Galactic center and allows us to understand how and if these processes can account for the formation of extragalactic NSCs.

A series of studies over the last years have been dedicated to investigate the dynamical structure of our NSC. Its estimated half-light radius is 4.2 ± 0.4 pc (Schödel et al. 2014) and its mass is $2 - 3 \times 10^7\,\mathrm{M}_\odot$ (Schödel et al. 2014; Feldmeier et al. 2014). The NSC is flattened, with an axis ratio between its apparent minor and major axis $q = b/a = 0.71 \pm 0.02$ (Schödel et al. 2014) and it is rotating in the same sense as the Galactic rotation. Its rotation velocity approaches approximately a value of 30 – 40 $\mathrm{km{\cdot}s^{-1}}$ within 4 pc (Chatzopoulos et al. 2015a; Feldmeier et al. 2014).

Recently it was suggested that the Galactic NSC is not a regular rotator: Feldmeier et al. (2014) give strong indications for a polar kinematic substructure in its central region, at a distance of ∼20″as well as a kinematic misalignment of ∼10° between the main body of the NSC and its apparent major photometric axis–the latter being aligned with the Galactic plane (see Figure 4.3). As discussed in

[1]The first error term corresponds to the orbital fitting uncertainty, and the second error term is the jackknife uncertainty from the reference frame.

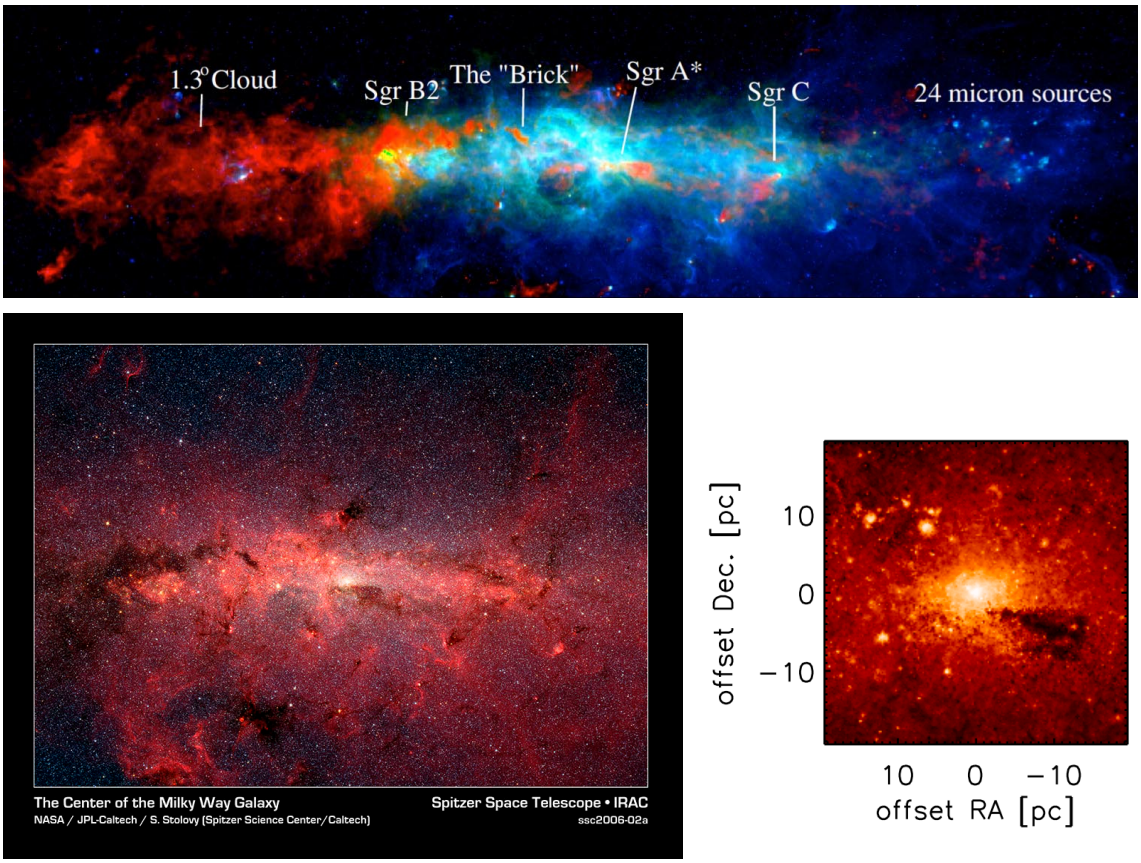

Figure 4.2: *Top:* An infrared and multi-wavelength image of the inner 500 pc of our Milky Way, showing the central molecular zone (CMZ). Dense gas is shown in red, and warm and cold dust in green and blue respectively. Several key objects in the region are labeled, including Sgr A*, and a set of embedded young stellar clusters seen at 24μm on the right (credit: Cara Battersby, CfA). *Bottom left:* A Spitzer Infrared Array Camera (IRAC) image of the central region of the MW extending 450 pc along the Galactic plane. Image produced by NASA, JPL Caltech, Susan Stolovy (Spitzer Science Center / Caltech). *Bottom right:* Zoom into the 4.5μm image of the MW NSC with IRAC, showing prominent dust extinction on the right side. Adapted from Schödel et al. (2014).

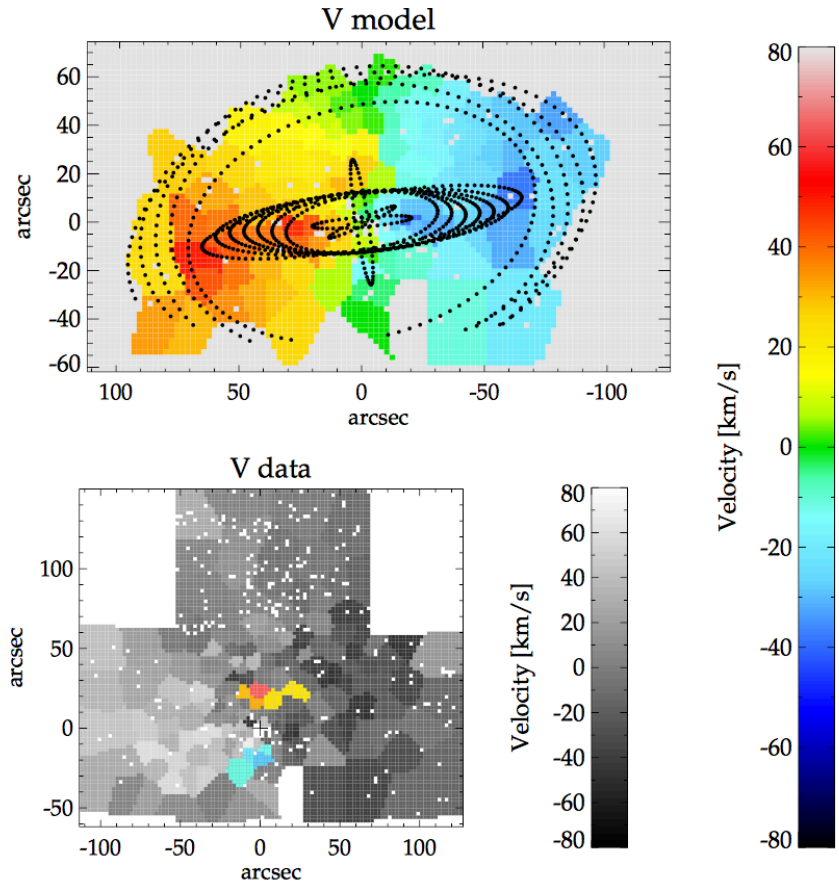

Figure 4.3: *Top panel:* Kinemetric model of the stellar velocity map of the MW NSC, with the ellipses denoting the different kinematic families within ~4 pc. The Galactic plane lies parallel to the x axis of this map. *Lower panel:* the stellar velocity map is shown in grayscale, the bins that show rotation perpendicular to the Galactic plane are overplotted in colour scale. Adapted from Feldmeier et al. (2014).

previous chapters, those kinematic peculiarities could be interpreted as fossil records of past merger events – the detailed study of those features in the Galactic NSC can thus provide us with important clues about its formation, as well as the formation of extragalactic NSCs.

4.2 Formation Scenarios

The scaling relations, the morphologies and kinematics of NSCs and their prominent existence in all galaxies across the Hubble sequence, suggest that there must be a close connection between the formation and evolution of the galactic nucleus with its surrounding galaxy. Hence the detailed study of the formation of NSCs can provide us with very important information on galaxy formation and evolution.

Two main scenarios have been proposed to explain the formation of NSCs; 1) the *"in situ formation scenario"* (Loose et al. 1982; Milosavljević 2004), according to which the NSC forms as gas infalls to the centre of the galaxy, where subsequently star formation takes place locally and most likely in an episodic manner (e.g. Schinnerer et al. 2008), and 2) the *"cluster-inspiral scenario"* (Tremaine et al. 1975; Capuzzo-Dolcetta 1993; Antonini et al. 2012; Gnedin et al. 2014), where the NSC is formed by the accretion of globular clusters, that infall to the centre due to dynamical friction. Both of these models can explain the mixture of stellar populations of different ages in NSCs (e.g. Walcher et al. 2006; Rossa et al. 2006; Seth et al. 2010). Until now, it is not clear, which model works best to explain the observations, or whether both of these processes are working in parallel to form and grow NSCs.

The detailed study of the dynamical properties of NSCs can, however, provide an important tool to disentangle the possible formation mechanisms of NSCs and understand the relative importance of each mechanism, in case they work in parallel.

The kinematics of NSCs formed via the cluster-inspiral scenario has so far been focused on simulations tuned for extragalactic NSCs (Hartmann et al. 2011). They found that NSCs formed solely through this mechanism can not exhibit the high amount of rotation that is actually observed. Additionally they show a central peak in their second order kinematic moment $V_{RMS} = \sqrt{V^2 + \sigma^2}$ that is too high to agree with observations.

Although this might be the case for some extragalactic NSCs, in the case of the Milky Way (MW) NSC, recent findings by Feldmeier et al. (2014) show a central peak in V_{RMS}, as well as strong evidence for a polar kinematic substructure in its central region and a kinematic misalignment between the main body of the NSC and the Galactic plane. These observations give evidence that globular cluster inspirals may indeed play an important role in the main build-up process of the MW NSC. However it is not yet clear if and how this mechanism can account for the rotation observed in NSCs, which is often attributed to gas infall, or star cluster infall from the galactic disc (e.g. Seth et al. 2008).

In the following work presented in Tsatsi et al. 2016 (*in press*), we investigate further if and how the cluster-inspiral scenario can reproduce the observed properties of NSCs, focusing in particular on

the kinematic signatures of the MW NSC. We use a set of N-body simulations of the formation of a NSC through the consecutive infall of globular clusters (GCs) in a Milky Way-like nuclear bulge with a central massive black hole (MBH) (Antonini et al. 2012; Perets & Mastrobuono-Battisti 2014). The NSC is analyzed in an observational-like manner, constructing mock photometric and line-of-sight stellar kinematic maps that we then use to assess the dynamical properties of the simulated NSC.

4.3 A Merger Model for the Milky Way NSC

4.3.1 Simulations

The N-body simulations used in this work are described in detail in Antonini et al. (2012) and Perets & Mastrobuono-Battisti (2014). They simulate the formation of a Milky Way-like NSC through the consecutive infall of 12 identical globular clusters (GCs) with a mass of $1.1 \times 10^6\,M_\odot$ each, in the inner region of a nuclear bulge ($M_{nb} = 10^8\,M_\odot$), hosting a central MBH ($M_\bullet = 4 \times 10^6\,M_\odot$), similar to the MW MBH (Genzel et al. 2010; Boehle et al. 2016). Each GC is represented by a tidally truncated King (1966) model and is initially moving on a circular orbit with randomly chosen parameters, at a galactocentric distance of 20 pc. The time interval is kept constant between infalls and it is ~0.85 Gyr, rescaled to the real mass of the particles, as described by Mastrobuono-Battisti & Perets (2013). After the last infall, the NSC and the surrounding nuclear bulge are let to evolve in isolation for ~2.2 Gyr, adding up to a total simulation time of ~12.4 Gyr. The total mass of the resulting NSC is approximately $1.4 \times 10^7\,M_\odot$. This value is in agreement on the 2-sigma level with the mass of the MW NSC ($2.5 \pm 0.6 \times 10^7\,M_\odot$), as estimated by Schödel et al. (2014).

Here we analyse three realisations of the initial conditions described above, with different randomisations of the initial orbital parameters of the infalling GCs (see Table 4.1 for the orbital parameters used in each simulation). In all simulations the longitude of ascending node Ω and inclination i of the GC orbit are randomly chosen. Simulation III differs from Simulations I and II because i is chosen with the constraint that $i < 90°$, so that the GCs infall with a similar orbital direction to the centre of the Galaxy (only prograde orbits). This choice of initial parameters has been made to represent clusters that might have initially formed in the CMZ of the MW, that at 20 pc distance from the centre will have random offsets with respect to the Galactic plane, but all share a similar orbital spin. Figure 4.4 shows a schematic diagram of the 3 simulation set-ups.

4.3.2 Kinematic Evolution of the NSC

Figure 4.5 shows the evolution of the specific angular momentum (i.e. the total angular momentum divided by mass) of both the NSC remnant and the surrounding nuclear bulge after each infall for the three simulation set-ups. The NSC remnants show strong angular momentum variance after each infall, which depends on the orientation of the infalling GC. Finally after the 12th infall, the system is let to evolve in isolation, resulting in no change in angular momentum. All three NSC remnants

n	Simulation I		Simulation II		Simulation III	
	Ω	i	Ω	i	Ω	i
	(deg)	(deg)	(deg)	(deg)	(deg)	(deg)
1	82.4	60.7	171.3	118.6	175.9	10.0
2	327.7	178.7	237.8	173.0	7.8	35.0
3	76.2	139.5	325.9	143.0	284.7	6.7
4	290.6	171.3	39.6	26.9	314.1	20.3
5	335.4	24.6	89.3	117.7	224.9	23.0
6	300.6	18.2	27.9	9.5	254.8	10.7
7	343.9	173.9	232.9	6.3	246.7	39.9
8	47.9	128.9	262.5	22.2	126.2	87.8
9	272.0	2.3	51.1	174.1	326.8	7.1
10	41.3	139.0	316.6	94.8	52.2	79.8
11	300.9	153.5	165.9	4.2	9.1	29.4
12	318.2	120.2	61.8	79.1	136.4	35.7

Table 4.1: Initial orbital parameters of the 12 infalling globular clusters in the three simulations used in this work: longitude of ascending node Ω and inclination i are given for each simulation, calculated with respect to the same simulation reference frame.

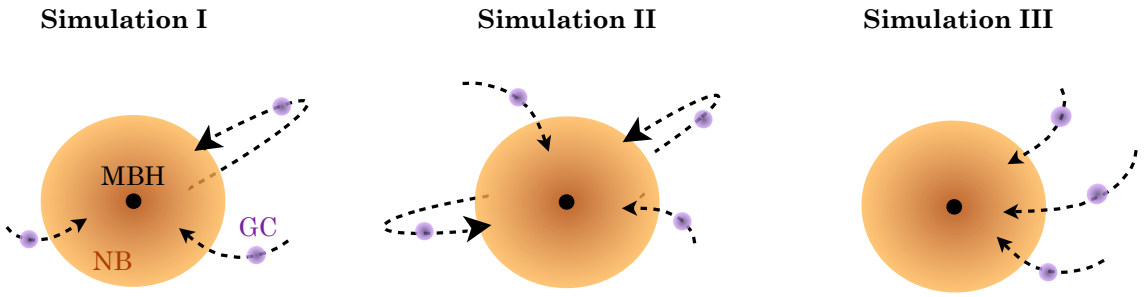

Figure 4.4: Schematic diagram of the initial conditions in the three simulation set-ups for the consecutive infall of 12 globular clusters (GCs) onto a massive black hole (MBH) surrounded by a nuclear bulge (NB). Simulation I and II correspond to randomly selected orientations of orbits of GCs, while in Simulation III GCs share a similar orientation of infall (no retrograde orbits).

show strong rotation in the final snapshots as can be seen from their high specific angular momentum. Simulation III results in a NSC with significantly higher angular momentum, as a consequence of the missing GCs in retrograde orbits. Figure 4.5 also shows the evolution of the specific angular momentum of the surrounding bulge for all simulations. The bulge rotation shows a small increase with time. The amount of bulge rotation is larger for more strongly rotating NSCs, meaning that the kinematics of the nuclear bulge can be affected by the NSC formation mechanism. The amount of bulge rotation in the final snapshot is, however, very low for all the three models.

Figure 4.6 shows the evolution of $|\Delta h|$, the specific angular momentum variation of the NSC after each infall, as well as the evolution of the precession angle $\Delta\alpha$ of the NSC. The latter shows the change in the orientation of the angular momentum vector (rotation axis) of the NSC after each infall.

The variation of $|\Delta h|$ is higher during the first infalls and becomes gradually smaller during the last infalls, as the NSC grows in mass and consequently the mass ratio between every infalling GC and the growing NSC becomes smaller. The specific angular momentum of the NSC shows no variation during the last ~2 Gyr of evolution where there is no infall.

We note that even if the globular clusters are initially randomly distributed around the center, their net angular momentum is not negligible. Most of their net angular momentum is transferred to the NSC. For example, in Simulation I, $\sim$ 65% of the total input angular momentum of the system is transferred to the NSC in the final timestep. The rest $\sim$ 35% is transferred to the surrounding nuclear bulge, which, however, does not correspond to a high rotation, as shown in Figure 4.5.

The precession angle $\Delta\alpha$ of the NSC on the other hand, seems to show a more stochastic evolution. Even after the last infall, where the mass ratio of the inspiralling GC and the growing NSC is as small as 1:11, the precession angle ranges from 15° (Simulation II) to as much as 40° (Simulation III), depending on the inclination of the infalling GC and the dynamical structure of the NSC. When the system is let to evolve in isolation, the angular momentum vector shows almost no precession for Simulations I, II, while $\Delta\alpha \sim 5°$ for Simulation III.

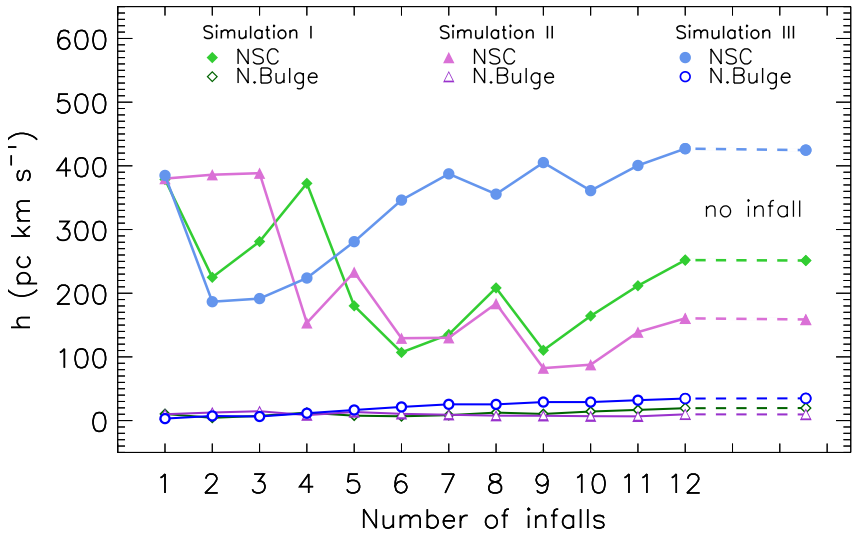

Figure 4.5: Evolution of the specific angular momentum h of the simulated NSCs after each infall. The green (diamonds), magenta (triangles) and blue (circles) points correspond to Simulation I, II, and III, respectively. Filled symbols correspond to the NSC, while open symbols correspond to the surrounding nuclear bulge particles. Dashed lines correspond to the last timestep of the simulation where the system evolves in isolation (no infall). Adapted from Tsatsi et al. 2016 (*in press*).

Note the anti-correlation between $|\Delta h|$ and $\Delta\alpha$, at least for the first $\sim$ 9 infalls in all simulations. This anti-correlation reflects the way the orbit inclination of an infalling cluster impacts the resulting angular momentum of the growing NSC. A prograde or retrograde infall will cause a high $|\Delta h|$ and low $\Delta\alpha$, while infalls of intermediate inclinations will have the opposite effect. The anti-correlation becomes weaker as the growing NSC becomes more massive (after the 9th infall).

4.3.3 Kinematics and Morphology of the NSC

In order to compare the orbital and mass distribution of the final NSCs with observable properties, we create two-dimensional mock stellar mass and kinematic maps as follows. Particles are projected along a line-of-sight which is perpendicular to the total angular momentum vector of the NSC, meaning that the line-of-sight rotation observed should be maximum. Particles are then binned on a regular grid centred on the centre of mass of the cluster, with a field-of-view (FoV) of 10 pc×10 pc and a pixel size of 0.08 pc.

The bulk velocity of the NSC is estimated within a sphere of 50 pc around the centre and subtracted from all particle velocities. The extracted kinematic maps are spatially binned using the 2D Voronoi binning method (Cappellari & Copin 2003), based on a minimum number of particles per pixel in the map. Signal corresponds to the number of particles per pixel and we adopt Poisson noise, such that our signal-to-noise ratio per bin (SN_{bin}) corresponds approximately to a target value $SN_T \sim 15$.

The stellar line-of-sight velocity distribution (LOSVD) is then extracted and fitted with the Gauss–

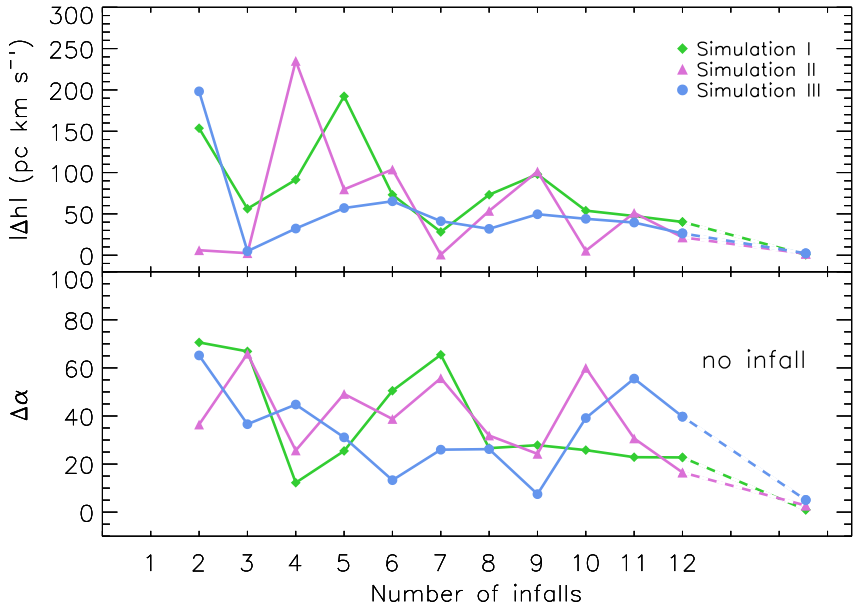

Figure 4.6: *Top:* Change of the specific angular momentum $|\Delta h|$ of the NSC after each infall. The green (diamonds), magenta (triangles) and blue (circles) points correspond to Simulation I, II, and III, respectively. *Bottom:* Evolution of the precession angle $\Delta\alpha$ of the angular momentum vector of the NSC after each infall. Note the anti-correlation of $|\Delta h|$ and $\Delta\alpha$ for each simulation. Adapted from Tsatsi et al. 2016 (*in press*).

Hermite series (van der Marel & Franx 1993), as implemented by van de Ven et al. (2006Appendix), which allows us to extract the Gauss–Hermite parameters for every bin (V, σ, h_3 and h_4). The mass and stellar LOSVD of the three simulated NSCs are shown in Figure 4.7.

4.3.4 Comparison with Observations of the Milky Way NSC

In order to compare with observations, we choose a FoV of 5 pc radius, which is approximately the half-light radius of the MW NSC (Schödel et al. 2014)[2]. The half-mass radius of our simulated NSC is approximately 10 pc for all simulation set-ups. We would expect differences between observed half-light and half-mass radius of the MW NSC if the mass-to-light ratio is not constant, as a result of the non-trivial interplay between mass segregation and the presence of young bright stars in the central region (e.g. Paumard et al. 2006). Within 5pc, the simulated NSC matches the observed shape of the surface density distribution of the MW NSC (Antonini et al. 2012). Therefore, we limit our kinematic analysis and comparison to this radial extent.

Using the first and second moments of the intensity distribution of our mock images, we find the position of the projected major axis and the flattening $q = b/a$ of our simulated NSCs within the adopted FoV of 5 pc radius. The average flattening of the NSC is $q = 0.64$ for Simulation I, and

[2]We note however, that Fritz et al. (2016) report values for the half-light radius of the MW NSC that range from 5 to 9 pc.

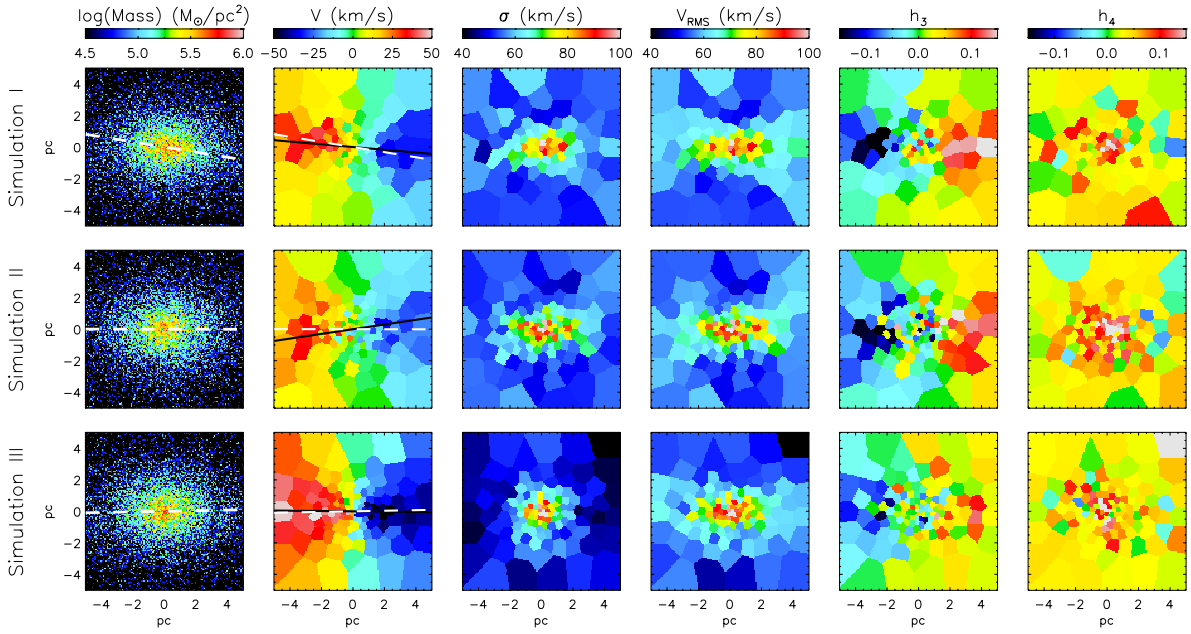

Figure 4.7: LOSVD of the simulated NSC. From left to right: Projected stellar mass surface density, line-of-sight velocity v, velocity dispersion σ in km·s^{-1}, and higher-order moments h_3 and h_4, comparable to the skewness and the kurtosis, respectively. The white dashed line shows the major photometric axis, while the solid black line shows the kinematic major axis of each cluster. Adapted from Tsatsi et al. 2016 (*in press*).

$q = 0.69$ for Simulations II and III. These values are remarkably similar to the observed flattening of the MW NSC, $q_{obs} = 0.71 \pm 0.02$ (Schödel et al. 2014).

The NSC shows a significant amount of rotation, of an amplitude of ~40 km·s^{-1} within 5 pc for Simulation I and II. The velocity is higher (~50 km·s^{-1}) for Simulation III, where the infalling GCs have a similar initial orbital direction.

In order to compare our results with the observed kinematic profiles of the MW NSC, we estimate the kinematic major axis of the NSC within the adopted FoV using the kinemetry method, as developed by Krajnović et al. (2006). The kinematic axis for each simulated NSC is shown in Figure 4.7 (solid black lines). We then place a mock slit along the kinematic axis, of width of 0.84 pc and extract the LOSVD of the simulated clusters in equal-size bins of 0.84 pc size, which corresponds to a binning similar to the one used by Feldmeier et al. (2014) to the MW NSC. The corresponding errors are calculated by Monte Carlo simulations of the extracted LOSVD (see van de Ven et al. 2006). The profiles of V, σ and V/σ for the three simulations are shown in Figure 4.8. The kinematic profiles show a very good agreement with the kinematic profiles observed in the MW NSC (Feldmeier et al. 2014).

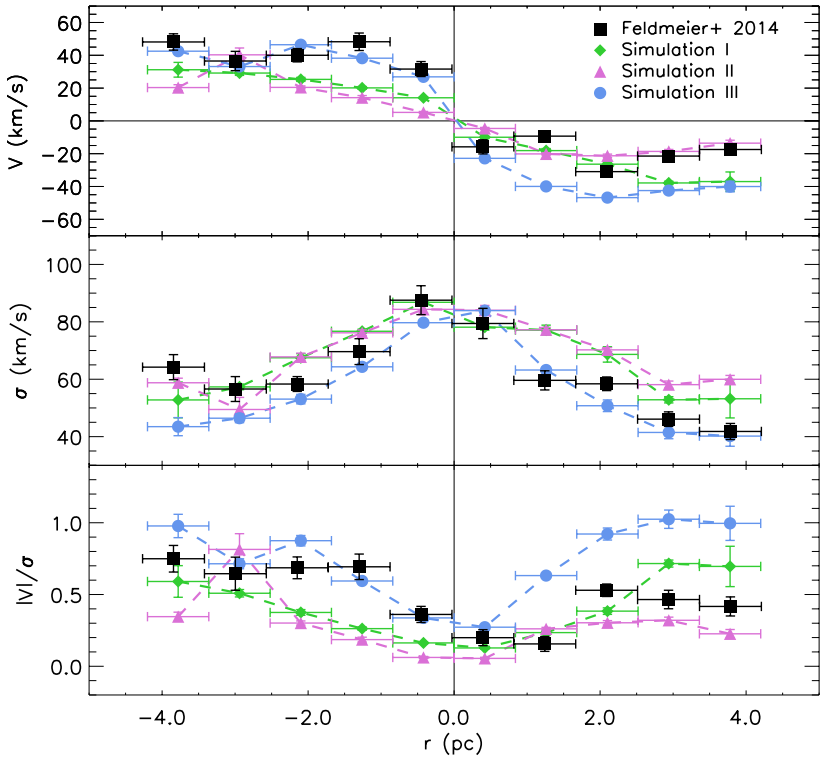

Figure 4.8: Kinematic profiles (V, σ and V/σ) for the three simulated clusters (dashed lines) compared to the corresponding profiles of the Milky Way NSC (black squares) by Feldmeier et al. (2014). All profiles are extracted from a slit along the kinematic axis. The asymmetry between left and right side of the MW NSC is caused by dust extinction (Chatzopoulos et al. 2015b). Adapted from Tsatsi et al. 2016 (*in press*).

4.3.5 Kinematic Misalignments and Substructures

Figure 4.7 shows the measured kinematic and the photometric major axes of all simulated NSCs within the adopted FoV. We find that the offset between these two axes within 5pc is $\Delta\theta \sim 4.2°$, 8.6° and 0.5° for Simulations I, II, and III, respectively. Simulation I also shows a misalignment of about 9.2° between the photometric major axis within 5pc and the projected plane, which is perpendicular to the total angular momentum vector of the NSC (the x axis of Figure 4.7). Simulation III, however, characterized by inspiralling GCs with similar orbital directions, shows no significant offset between the kinematic and the photometric axis of the resulting NSC.

Such a misalignment between kinematics and morphology has also been recently observed in the MW NSC, with a median value of $\Delta\theta \sim 9° \pm 3°$, suggesting this as an evidence that cluster-inspirals may have played an important role in the formation of the MW NSC (Feldmeier et al. 2014). Here we confirm that this scenario is able to produce observable misalignments between the photometry and kinematics of the resulting NSCs, which are stronger in the case where the infalling GCs are employed in random orbital directions (Simulations I and II), however not in the case where the GCs infall with a similar orbital direction (Simulation III).

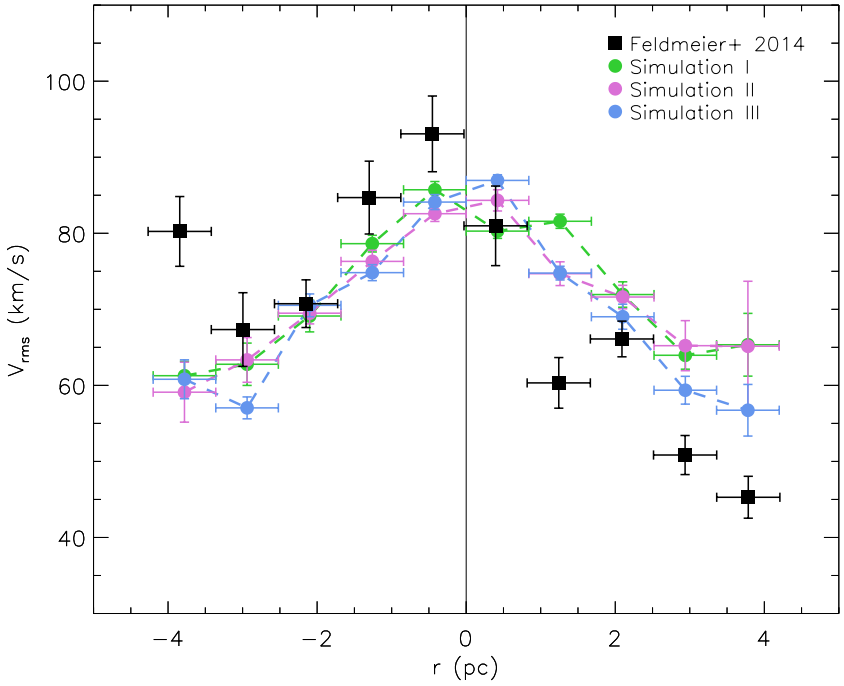

Figure 4.9: V_{RMS} profiles for the three simulated clusters (dashed lines) compared to the corresponding profiles of the Milky Way NSC (black squares) by Feldmeier et al. (2014), showing a central peak.

A kinematic substructure, most likely associated with an old stellar population, has been found at the centre of our MW NSC (Feldmeier et al. 2014). This substructure is almost aligned with the Galactic minor axis at a distance of 0.8 pc from the Galactic centre.

To quantify the ability of cluster-inspirals on creating such kinematic substructures, we create density maps of the angular momentum vector distribution for all our simulated NSCs (Figure 4.10) within a FoV of 10×10 pc^2. The angular momentum vector of every particle is projected onto the angle space (θ,ϕ) of a spherical coordinate system, where the z-axis is the rotation axis of the main body of the NSC within 5 pc. In this space the region $\phi \in [0°, 45°]$ corresponds to prograde (direct) rotating particles (D), $\phi \in [135°, 180°]$ to retrograde (R) and $\phi \in [45°, 135°]$ to particles rotating around the major axis or polar (P; where P+ has $\theta < 180°$ and P- has $\theta > 180°$, and correspond to particles with opposite polar spins).

We see that in Simulation III most of the particles end up with prograde rotation ($\phi < 45°$), while in Simulations I and II there is a significant fraction of angular momentum with $\phi > 45°$ (polar or retrograde rotation). Both Simulation I and II show strong kinematic substructures up to the 9th infall. However, as the mass ratio between each infalling GC and the NSC keeps decreasing, the GCs have less of an impact on the central kinematics of the NSC.

In order to translate this to observable properties, we create mock line-of-sight velocity maps of all the simulated NSCs at the last timesteps of their evolution and apply the kinemetry method (Krajnović

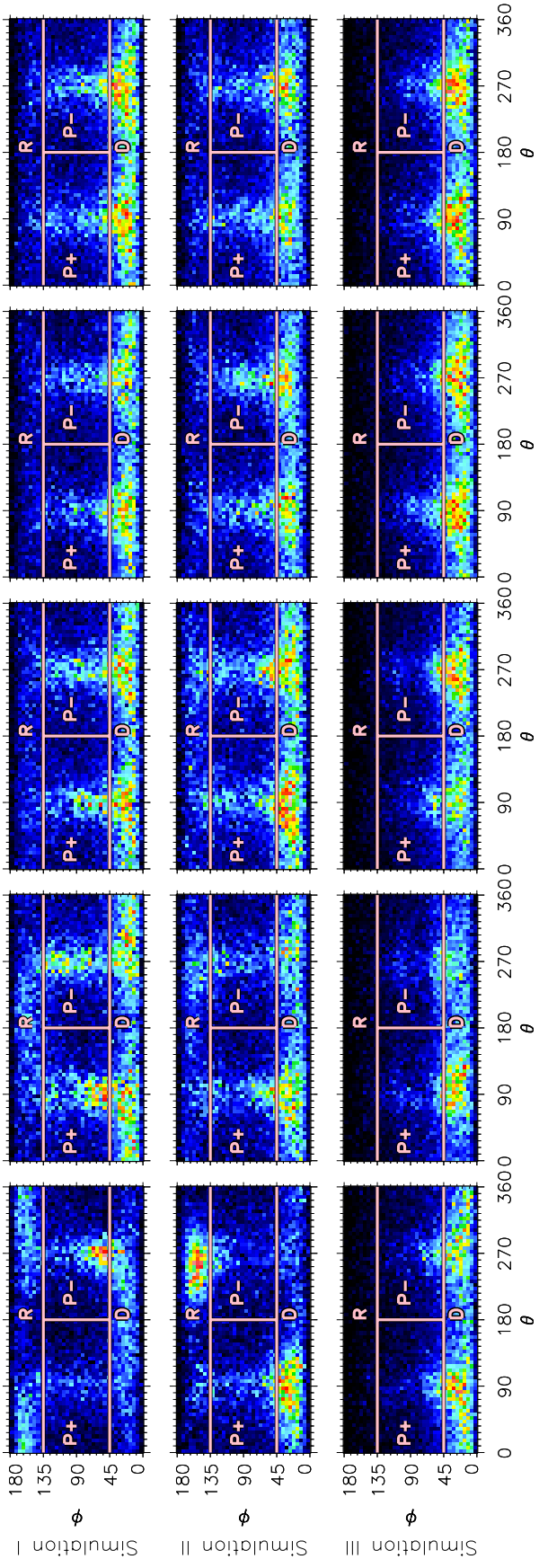

Figure 4.10: Evolution of the angular momentum vector distribution for Simulations I, II, III (top to bottom) for the last 5 timesteps of each simulation (left to right). The angles ϕ and θ are the spherical coordinates of the angular momentum within a field of view of 5 pc. The distribution is colour-coded according to the magnitude of the total angular momentum vector per pixel, normalised to the maximum value for every timestep. The distribution is divided in 4 regions that correspond to particles with prograde (D), retrograde (R) and polar spins (P+, P-), respectively. Adapted from Tsatsi et al. 2016 (*in press*).

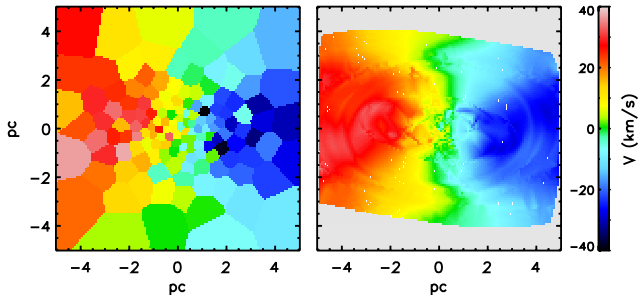

Figure 4.11: Left: Mock line-of-sight velocity map of the NSC of Simulation II, after the infall of the 12th GC. Right: the corresponding kinemetric model, showing a weak polar twist at ~3 pc. Adapted from Tsatsi et al. 2016 (*in press*).

et al. 2006). Figure 4.11 shows one of these kinematic maps, that corresponds to the NSC of Simulation II, after the 12th infall. The kinemetric model shows a weak polar kinematic twist, resulting from an imbalance between particles with opposite polar spins P+ and P- in Figure 4.10. This apparent substructure is not observed, however, in the next (last) timestep, after the NSC evolves for ~2 Gyr in isolation.

Cole et al. (2016) suggested that it is observationally difficult to kinematically distinguish stars belonging to a specific GC progenitor in the NSC remnant, except in the case where the GC is the most recently (last) accreted. This is also confirmed in our simulations. The stars responsible for the projected polar twist belong to all the four previously accreted GCs. Although in our case the last accreted GCs do not affect significantly the central kinematics of the NSC, we show that the existence of a projected central kinematic twist is a possible outcome of the process of phase space mixing of the stellar populations belonging to different GCs.

We conclude that in our adopted models the NSC cannot exhibit a strong kinematically distinct component in the case where the infalling GCs inspiral with a similar orbital spin (Simulation III). In the case that the GCs infall with random orbital directions, however, the NSC ends up with a significant amount of non-regular rotation, which can translate into weak substructures in the projected kinematics. We note that these substructures could be enhanced with a different choice of initial orbital parameters or structural properties of the infalling GCs. Such a study is, however, beyond the scope of this work.

4.3.6 The Effect of Stellar Foreground Contamination

Integral Field Unit (IFU) observations of NSCs are naturally contaminated by non-NSC stellar populations of the host galaxy along the line-of-sight. We study the effect of contamination from non-cluster stars to the observed LOSVD of NSCs. We construct mock kinematic maps adopting the same technique as described in Section 4.3.3, accounting for the contribution from all the surrounding nuclear bulge stars in our simulations that are present along the line-of-sight and within the adopted field-of-

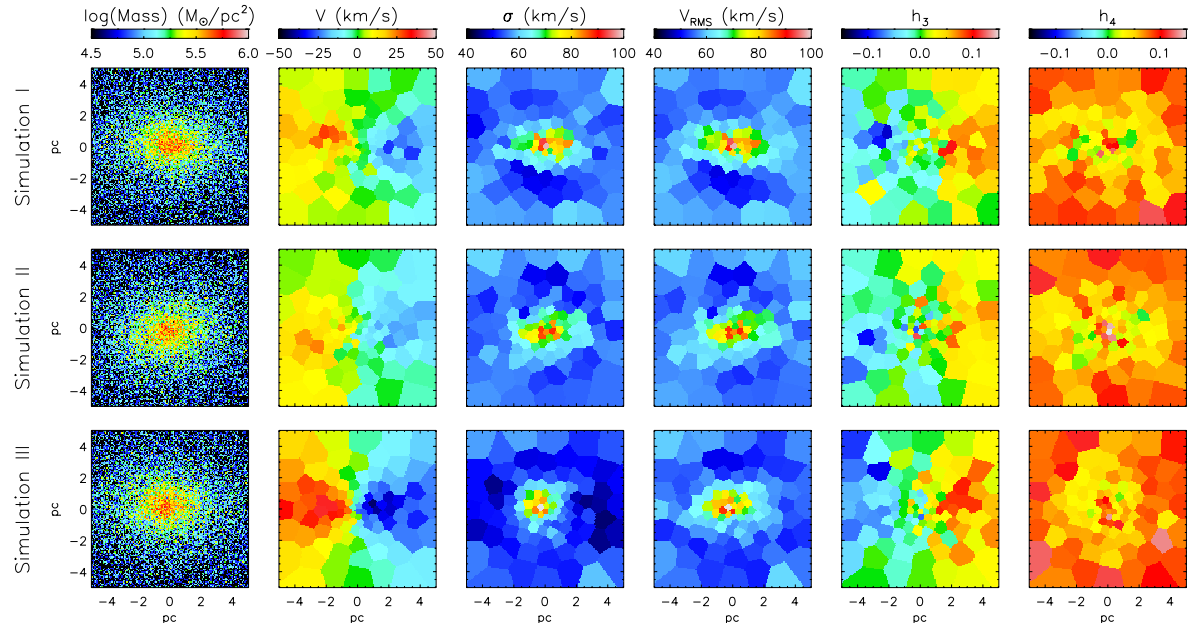

Figure 4.12: Same as Figure 4.7, where the projected NSC is contaminated with stars from the surrounding bulge. Adapted from Tsatsi et al. 2016 (*in press*).

view of 10×10 pc^2. The resulting LOSVDs of all the simulation particles (NSC and nuclear bulge) are mass-weighted and fitted using Gauss-Hermite series, as done for the non-contaminated case.

The LOSVD of the “contaminated" NSCs is shown in Figure 4.12. The nuclear bulge stars affect mostly the outer parts of the projected kinematics, where the mass density of the NSC drops and the surrounding nuclear bulge starts to dominate. The nuclear bulge, being non-rotating and dynamically “hotter” than the NSC, is causing the LOS velocity to decrease and the velocity dispersion to increase in the outer parts. The higher order moments are also affected– h_3 slightly decreases, while h_4 increases in the outer parts. This increase of σ and h_4 in the outer parts serves as a signature of the existence of contaminating nuclear bulge stars in the LOS kinematics of a NSC.

Accounting for this contamination, the model that reproduces best the observations of the MW NSC is the one that shows the highest intrinsic rotation, resulting from Simulation III (Figure 4.13).

We should note, however, that the amount of rotation in our contaminated NSC yields a lower limit to the rotation that would be observed if the NSC was embedded in a more realistic galactic environment. This is due to the fact that our contaminant is a dynamically hot, non-rotating component, while in reality the contamination along the line-of-sight can also contain rotating components (e.g. stars from the Galactic disc and bar) that would affect the observed LOSVD of the NSC.

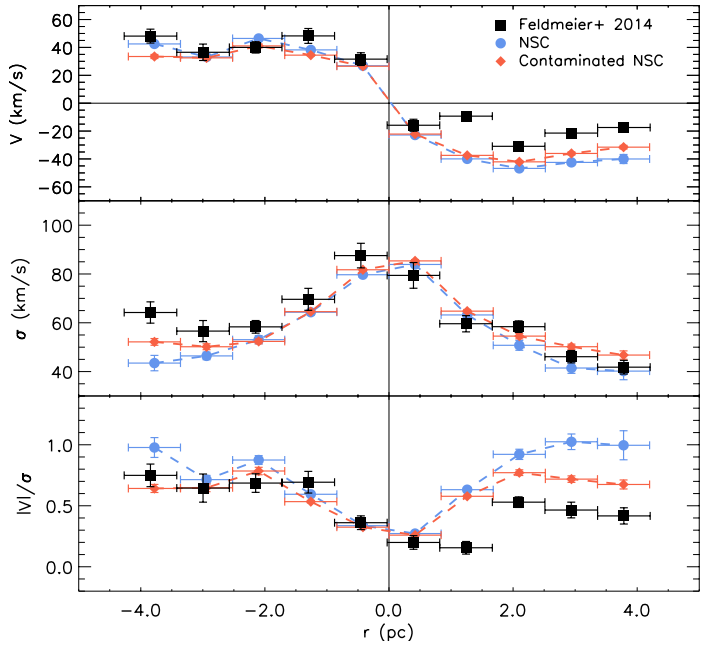

Figure 4.13: Same as Figure 4.8 for the NSC of Simulation III (blue circles), but accounting for contamination from stars of the surrounding nuclear bulge (red diamonds). Adapted from Tsatsi et al. 2016 (*in press*).

4.4 Conclusions and Discussion

In this chapter we explore whether and how the cluster-inspiral formation scenario can account for the observed rotation and kinematic properties of NSCs, focusing in particular to the MW NSC. We use *N*-body simulations of the consecutive infall of globular clusters (GCs) in the centre of a MW-like nucleus and construct mock line-of-sight kinematics of the resulting NSCs. Our results can be summarised as follows:

(i) We find that NSCs formed through GC inspirals can show a significant amount of rotation, even if the GCs are initially randomly distributed around the centre. We conclude that no fine tuning of the orientation of the inspiralling GCs is needed to result in a rotating NSC.

(ii) Both the flattening and the kinematic properties of our simulated NSCs match the observed properties of the MW NSC very well.

(iii) In the case where the GCs fall into the centre from random directions, the resulting NSC shows a significant amount of non-regular motion, which can result in projected kinematic misalignments and weak kinematic twists. In the case that the GCs fall in with a similar orbital orientation (e.g. if they originate from the Galactic disc), the resulting NSC shows more rapid and regular rotation.

(iv) Given that IFU observations are naturally contaminated with stars from the nuclear bulge sur-

rounding the NSC, we find that such a contamination lowers the observed rotation and imprints its dynamical signature in the outer parts (r>2pc), accounting for an increase in the LOS velocity dispersion σ and the kurtosis-like higher-order moment h_4 of the NSC.

We have studied the formation of NSCs solely through cluster-inspirals and do not exclude the possibility that gas accretion and in situ star formation play a role in their formation. The prevalence, if any, of each formation mechanism should be connected to the galactic environment of the NSC.

In that sense, the cluster-inspiral scenario is expected to play a dominant role in the formation of rotating NSCs in early-type galaxies that are too gas-poor to support the formation of a NSC solely through gas accretion. However, the NSC formation could have happened at a time when gas was still present. This would have implications for the formation of dwarf elliptical galaxies. If the NSCs that they host were formed through gas accretion at a time when the galaxy was still gas-rich, then this would support the theory where nucleated dwarf elliptical galaxies evolved from nucleated late-type spiral progenitors after depletion of gas through star formation, galaxy harassment (Seth et al. 2006) or ram pressure stripping, as a major merger could potentially destroy the nucleus.

Although this scenario seems possible, it does not explain the detections of nucleated dwarf elliptical galaxies hosting KDCs (Toloba et al. 2014) – a central kinematic feature, which, as discussed in Chapter 2, is most likely of a merger origin. This implies that either the nucleus could survive a merger, or that the nucleus gets destroyed from an early merger but gets subsequently rebuilt by dry accretion of clusters.

Especially for low-mass early-type galaxies observational evidence seem to support the cluster accretion scenario (e.g. Turner et al. 2012; den Brok et al. 2014). High-mass early-type galaxies seem to show a more complex nature: the existence of counter-rotating populations in NSCs points towards the cluster-inspiral scenario, while the complex stellar populations that they host point towards episodic gas accretion and in situ star formation (Lyubenova et al. 2013).

In the case of late-type host galaxies such as our Milky Way, both mechanisms are expected to work in parallel, as supported by their observed metallicity spreads and complex star formation histories (e.g. Rossa et al. 2006; Do et al. 2015). However, the contribution of each mechanism to the main build-up process of the MW NSC is not clear. Observational evidence shows that there has been an increase in star formation in the last few hundred Myr of evolution of our MW NSC (Blum et al. 2003; Pfuhl et al. 2011). In the very centre (~0.5 pc) the light is dominated by 6 Myr old stars (e.g. Paumard et al. 2006; Feldmeier-Krause et al. 2015) and in the central 1pc only a small fraction of low-metallicity stars are consistent with the typical metallicities of MW globular clusters (Do et al. 2015), favoring in situ star formation from gas accretion.

On the other hand, approximately ~ 80% of the MW's NSC stars in the central ~2.5 pc were formed more than 5 Gyr ago (Blum et al. 2003; Pfuhl et al. 2011). Kinematic evidence (e.g. the centrally peaked V_{RMS}, the kinematic offset from the Galactic disc, the evidence for a polar kinematic substructure) support the cluster-inspiral formation scenario. Here we have shown that cluster-inspirals can also account for the observed rotation of NSCs, an evidence that has been so far attributed to gas

infall.

Here we note that the complex stellar populations that are often observed in NSCs may be partly explained by the cluster-inspiral scenario, if the NSC was formed by massive clusters spanning a range of ages. Such an example is Henize 2-10, a dwarf starburst galaxy that appears to be in process of forming a NSC within the next 200 Myr, through the dry accretion of the young massive clusters surrounding its central massive black hole (Nguyen et al. 2014; Arca-Sedda et al. 2015).

The search for the dominant formation mechanism of NSCs is still ongoing and its connection to their galactic environment seems far from a foregone conclusion. Clarifying the nature of NSC formation would now require more detailed studies of their dynamics, their stellar populations and star formation history, combined with more realistic simulations of their formation.

Chapter 5

Conclusions and Outlook

5.1 Conclusions

In this thesis, we have adressed the role of mergers in explaining the observed present-day dynamical structure of their remnants, namely early-type galaxies (ETGs) and nuclear star clusters (NSCs). The approach we have adopted throughout this study was the construction of "mock" observables from numerical simulations that can be directly compared with observations. Our findings can be summarized as follows:

(i) We have shown that during a major merger between two disk galaxies, their orbital angular momentum can decay beyond zero and reverse its spin – meaning that *orbital reversals* during galaxy mergers are possible. We suggest that the cause of an orbital reversal is the significant mass loss that the two galaxies can experience during their close encounters, which results in a reactive force (thrust), known as the Mestschersky (1902) force. If strong enough, this can cause the two galaxies to change the sense of their orbital motion with respect to each other. This *"Mestschersky mechanism"* during a merger could have a crucial impact on the dynamics of the remnant that results from this process (*Chapter 2*).

(ii) Peculiar kinematic features such as *kinematically decoupled cores (KDCs)* in massive ETGs can be the result of major mergers, that probably built-up the central parts of these galaxies about ∼10 Gyr ago. Until now, it was thought that KDCs can result only from retrograde mergers, where the rotation of one of the progenitor galaxies involved in the merger is opposite to the other (Bois et al. 2010, 2011). However KDCs are very common in present-day slow-rotating ETGs, with a fraction that could be much higher than 50% – meaning more than the retrograde scenario can predict (which should be less than 50%, if retrograde and prograde mergers are equally common). We suggest that KDCs can also result from prograde mergers, where the two progenitor galaxies share the same sense of rotation and the same sense of orbital motion with respect to each other. In such a scenario, the KDC can result from an orbital reversal of the two galaxies prior to their final merger. We suggest that this new formation channel of KDCs from prograde mergers is caused by the "Mestschersky mechanism" (see point (i)). This new scenario could explain the high fractions of KDCs observed in present-day ETGs by increasing the theoretically predicted rate of their occurence (*Chapter 2*).

(iii) Massive elliptical galaxies could be triaxial, and show *prolate rotation* (stellar motion around their major photometric axis). However, observations of such systems are rather rare. We present 9 new observed cases of prolate rotators from the CALIFA IFU Survey, adding a significant fraction to the known cases that were listed so far in the literature. Most of these prolate rotators are members of groups and clusters and 5 of them are BCGs, suggesting that their kinematic properties might be of merger origin. By performing a set of major merger simulations, we find that elliptical galaxies of a prolate shape and prolate rotation can be the end-products of major polar mergers of disk galaxies. These remnants could be the progenitors that built the central parts of massive present-day prolate rotators, which can explain the rarity of their observations, as a result of the infrequency of polar mergers (*Chapter 3*).

(iv) Nuclear star clusters (NSCs), the very massive and compact star clusters found in the centers of most galactic nuclei, might as well be the end-products of mergers. According to the *cluster-inspiral scenario*, massive globular clusters can infall and merge to the center of a galaxy due to dynamical friction and build the NSCs that we observe today in the majority of late-type, as well as early-type galaxies. However, until now, it was thought that NSCs that show a high amount of rotation (including the NSC of our Milky Way) could not be merger remnants, but were preferentially formed by gas accretion. For this reason, we investigate a set of N-body simulations of the cluster-inspiral formation of a Milky Way-like NSC. We find that even in the case where the infalling clusters merge with random orientations with respect to the center of the galaxy, the resulting NSC can show significant rotation, that matches very well with the one observed for the Milky Way NSC. Moreover, we find that the merger origin of the NSC imprints onto its present-day dynamical structure in the form of non-regular motions, that translates to observable kinematic twists and misalignments, which are also in agreement with observations of the Milky Way NSC. We suggest that the cluster-inspiral formation scenario can account for the rotation observed in NSCs (*Chapter 4*).

The study presented in this thesis focuses in particular on the dynamical imprints of mergers in the central stellar kinematics of remnants, and shows that a merger origin of early-type galaxies, as well as nuclear star clusters, is consistent with the complex present-day dynamical structure unveiled by their integral field unit (IFU) observations. We focused only on the analysis of the rotation and the dynamics of remnants formed in merger simulations, hence we cannot draw robust conclusions about the non-merger origin of such systems. As an example, it is possible that gas accretion also contributes to the mass assembly of NSCs, as well as ETGs. In the case of NSCs, an observational evidence for gas accretion would be the presence of young stellar populations in their centers. In elliptical galaxies, the extended HI disk structures they often exhibit, the kinematic misalignments between stellar and gaseous components of some S0s (e.g. Katkov et al. 2014) and/or the presence of outer star forming rings might be evidence for cold gas accretion[1](e.g. the famous "Hoag's object", Finkelman et al. 2011). We would suggest that a pure merger origin seems unphysical, and it is expected that the infall of gas might be an important part of the evolution of both elliptical galaxies and NSCs. Nevertheless, the relevant importance of gas accretion to the main assembly process of these systems is still unclear.

[1]Where accretion does not require cannibalism; gas may be accreted from galaxy fly-bys or cosmological filaments.

This first generation of IFS galaxy surveys, e.g. SAURON (Bacon et al. 2001), ATLAS^{3D} (Cappellari et al. 2011) and CALIFA (Sánchez et al. 2012), is now completed. At the time this thesis is written, the new era of second generation of IFS is starting, e.g. MUSE (Bacon et al. 2010) and MaNGA (Bundy et al. 2015), which are currently collecting new and more insightful data that will assess further the implications of our findings. Combined with the use of state-of-the-art numerical simulations, we will be able in the near future to understand better the nature of galaxies, both on large and small scales, as well as the physical processes that govern their formation and evolution.

5.2 Outlook

5.2.1 Recovering the Dynamical Structure of ETGs with Schwarzschild Models

Observationally constrained dynamical models can give us an insight to the intrinsic dynamical structure of galaxies. As discussed in the previous chapters, many early-type galaxies show strong evidence for *triaxiality* in their photometry (e.g., isophotal twists in their surface brightness distribution), as well as in their kinematics (e.g., kinematic misalignments, twists, prolate rotation in their velocity fields). Hence, the only way to recover a realistic intrinsic dynamical structure of such galaxies is the construction of *triaxial* dynamical models.

The key step in constructing a realistic dynamical model is the comparison with observable properties of the galaxy. Knowing the overall shape of a galaxy cannot provide a tight constraint on its structure - different combinations of orbits can build the same mass density (Statler 1987). However, using the line-of-sight velocity distribution (LOSVD) can provide the third dimension, which, combined with the two spatial dimensions that we see projected can give a tighter constraint on the intrinsic dynamical structure of the galaxy. In addition, it is well known that different formation histories predict different orbital structures for early-type galaxies (e.g. Barnes 1992), thus, recovering accurately their orbital structure is crucial in order to constrain their formation history.

Orbit-based dynamical modeling using *Schwarzschild's superposition method* (Schwarzschild 1979) is one of the most powerful techniques to infer the intrinsic shape and orbital structure of galaxies from their stellar kinematics (e.g. Verolme et al. 2002; Krajnović et al. 2005). This method, implemented in triaxial geometry (van den Bosch et al. 2008; van de Ven et al. 2008; van den Bosch & van de Ven 2009) is more general, and can be used to model the large variety of triaxial shapes observed in early-type galaxies. The main strength of the method is that it has been developed to fit the observed two-dimensional line-of-sight stellar velocity distribution, combined with the two-dimensional mass distribution of the galaxy as a constraint. It can thus infer the dynamical structure of a galaxy using observational constraints, without using any assumptions about the orbital anisotropy or axisymmetry of the galaxy. This technique has been widely used to measure the masses of supermassive black holes at the centers of galaxies (e.g. Walsh et al. 2012), the mass-to-light-ratio of galaxies, as well as to constrain their shape, orbital structure (e.g. van den Bosch et al. 2008) and their dark matter halo distributions (e.g. Weijmans et al. 2009).

However, the accuracy of this method to recover the real global parameters and dynamical structure of galaxies remains still uncertain. The only way to understand and quantify its accuracy is to use a known galaxy model, create simulated ("mock") observations, use them as the input for the code, and then test how well the output model recovers the input model. Until now, these tests have been performed using as an input analytic functions for the gravitational potential of the galaxy (van de Ven et al. 2008; van den Bosch & van de Ven 2009). Although these tests have improved our understanding of the strengths and degeneracies of the method, questions still remain about its accuracy to recover more realistic galactic models.

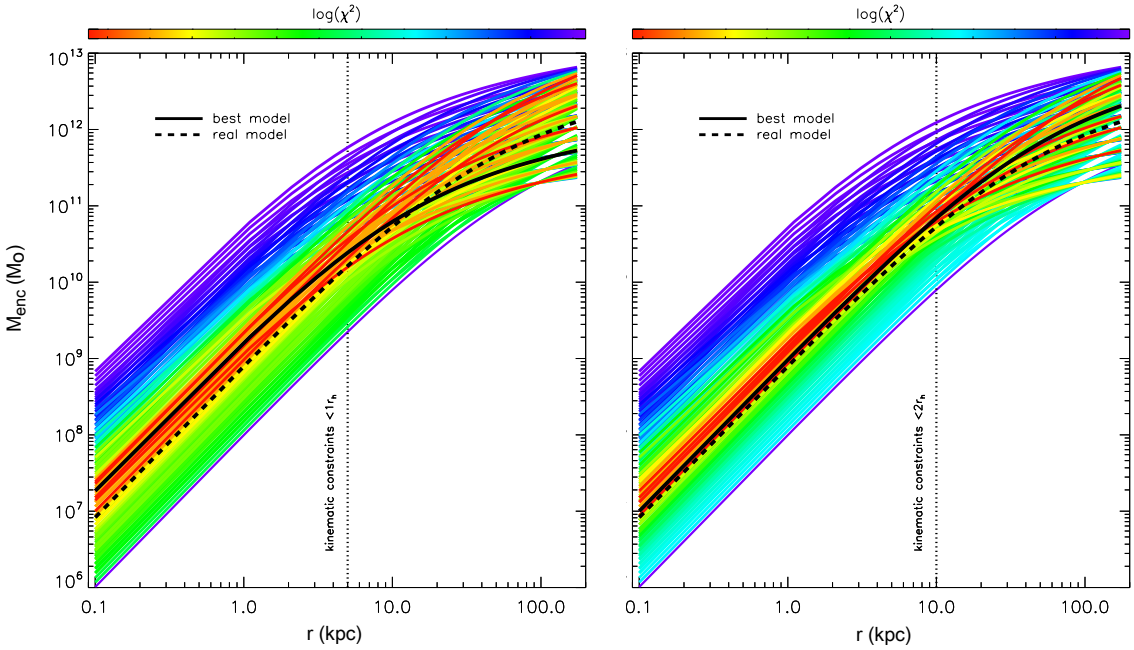

Figure 5.1: Recovery of the dark matter distribution of the simulated early-type galaxy described in Section 2.3.1 using triaxial Schwarzschild models. The colored curves show the enclosed dark matter halo mass (M_{enc}) as a function of radius retrieved from every Schwarzschild model, colored according to their corresponding χ^2. The solid black curve shows the best-fit model, while the dashed black curve corresponds to the "real model", as fitted to the simulated dark matter halo of the galaxy. The black dotted line denotes the spatial extent of the kinematics field-of-view used for the models (*left: 1 half-mass radius, right:2 half-mass radii*). The profile reaches out to the radius R_{200}=176 kpc of the real dark matter halo (see Appendix for a more detailed description of the models used.)

In future work, we plan to construct triaxial Schwarzschild models using mock observations of the simulated early-type galaxies described in *Chapter 2* and *Chapter 3*. The results of this study are very important to understand how well the output (global parameters and dynamical structure) retrieved from the models recovers realistic, simulated galaxy properties. As a first test, we investigate in particular how the accuracy of the recovery of the dark matter halo distribution of a galaxy depends on the quality of the mock observations (i.e. the spatial coverage of the LOSVD observations that we use). A more detailed description of the models and the code used is provided in the Appendix of this thesis.

Our preliminary results suggest that *the recovery of dark matter halo fractions of elliptical galaxies with dynamical models depends crucially on the spatial extent of the kinematic tracers used* (see Figure 5.1, and Figure A.3, Appendix). Even under the assumption that the mass-to-light ratio and the intrinsic shape of the galaxy are accurately constrained, one can estimate only the *enclosed* dark matter halo mass of a galaxy within the radius of the stellar kinematics field of view. In our preliminary models the enclosed dark matter fraction (total stellar over dark matter mass fraction) is recovered

within 1σ confidence, however this could mean a misprediction of a factor of ~2 of the enclosed dark matter halo mass in case the kinematic constraints extend out to only 1 half-mass radius.

However, we find that models where the stellar kinematic tracers extend beyond 2 half-mass radii of the galaxy are able to recover more accurately the enclosed dark matter mass (see Appendix).

Performing more detailed tests will allow to show how the recovery of the dark matter distribution, the orbital structure and other global parameters of the galaxy depend on the parameters used as an input for these dynamical models (e.g. the intrinsic shape, the mass-to-light ratio of the galaxy) and the degeneracies between them. The results of this study will finally reveal the accuracy with which the real dynamical structure of observed early-type galaxies can be recovered using such dynamical models.

5.2.2 The Effect of Intermediate Mass Black Holes on the Kinematics of NSCs

Over the last few years, significant effort has been devoted to the search for intermediate mass black holes (IMBHs) in the centers of globular clusters (GCs). IMBHs have masses of $\sim 10^2 - 10^4\,M_\odot$, intermediate between the stellar black holes ($M_\bullet < 10^2\,M_\odot$) and the massive/supermassive black holes found in the centers of galaxies ($M_\bullet > 10^4\,M_\odot$). The detection of IMBHs is a challenging and highly controversial issue of debate, in particular in globular clusters[2] (e.g. see Bianchini et al. 2015 and references therein). Numerical simulations of the formation and evolution of young dense clusters show that their formation and existence is theoretically permitted. According to these findings, a very massive star may form initially from runaway star collisions, sink to the center of the cluster due to dynamical friction and subsequently collapse to form an IMBH (Madau & Rees 2001; Gürkan et al. 2004; Freitag et al. 2006).

Given their possible existence in massive clusters, the cluster-infall scenario for the formation of NSCs presented in *Chapter 4* may be significantly affected by such objects. Mastrobuono-Battisti et al. (2014) explored the possible existence of IMBHs in the infalling GCs and their effects on the properties of the resulting NSC in the cluster-inspiral scenario. They found that IMBHs increase the rate of tidal disruption events to a value that is not in agreement with current observational estimates. Moreover, the resulting IMBH-populated NSC develops a central cusp, in contrast to the IMBH-free case, where it develops a core, the latter being more in agreement with observations of the Milky Way NSC. Mastrobuono-Battisti et al. (2014) thus conclude that if cluster-inspiral is the main mechanism for NSC formation, then typical NSCs, as well as the majority of the inspiralling clusters that form them, should not host IMBHs.

We plan to investigate further the dynamical implications of the presence of IMBHs in NSCs. Following the methods presented in *Chapter 4* (Tsatsi et al. 2016, *in press*), we construct the kinematic profiles of NSCs of the simulations set-ups presented in Mastrobuono-Battisti et al. (2014). These simulations concern different initial orbital parameters than the ones presented in *Chapter 4*, and model

[2]We note however, that apart from their elusive presence in GCs, there is strong observational evidence for the existence of IMBHs, such as the variable X-ray source HLX-1 in the edge-on spiral galaxy ESO 243-49 (Farrell et al. 2009).

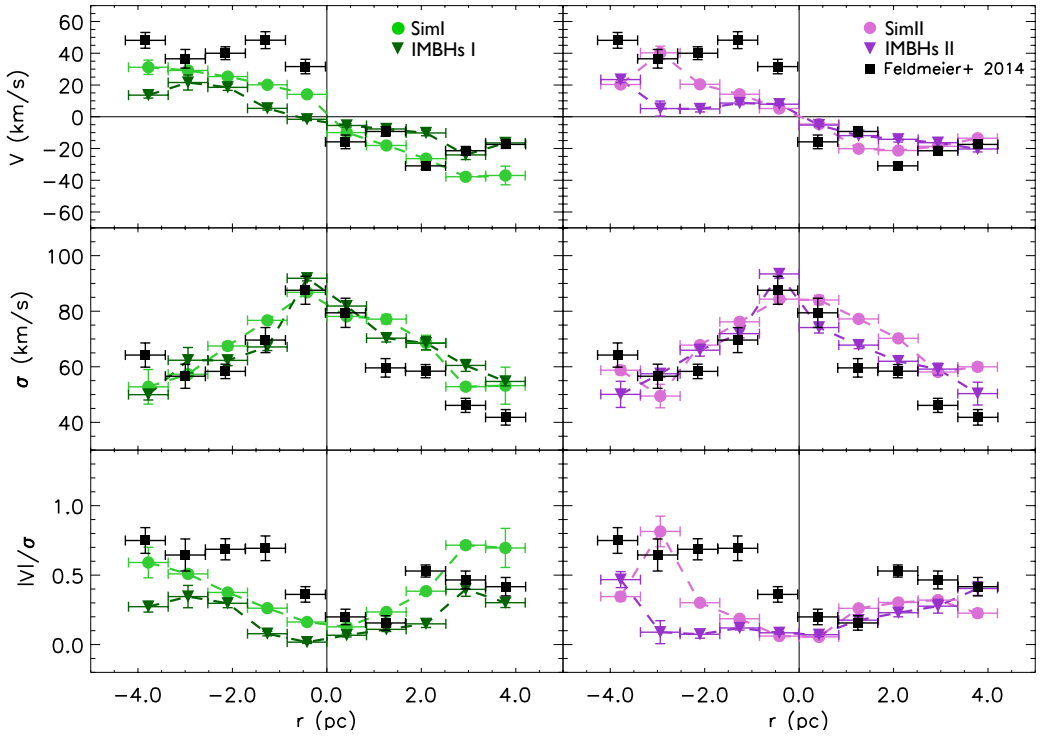

Figure 5.2: NSC kinematic profiles of the LOS velocity V, velocity dispersion σ in km·s^{-1} and V/σ for 4 different simulation set-ups. Simulation I (green circles) and Simulation II (magenta circles) correspond to the IMBH-free simulated NSCs described in *Chapter 4*. IMBHs I (dark green triangles) and IMBHs II (dark magenta triangles) correspond to the IMBH-hosting simulations described in Mastrobuono-Battisti et al. (2014) and conscern a different orbital set-up of the infalling GCs. Black squares correspond to the observed kinematic profiles of the MW NSC (Feldmeier et al. 2014), for comparison.

the formation of a NSC through the infall of 12 GCs that host IMBHs at their centers. The IMBHs are long-lived and survive in the central 2 pc of the NSC throughout its evolution without inspiralling to the central MBH, or getting ejected from its central region. We thus expect that their presence may have a significant influence on the dynamical structure of the NSC.

Figure 5.2 shows the kinematic profiles for the simulations described in Mastrobuono-Battisti et al. (2014) in the IMBH-hosting case, in comparison to the ones measured for the MW NSC (Feldmeier et al. 2014). We find that in the IMBH-hosting case the observed rotation of the NSC is significantly lower and the V/σ profile is flattened for both simulation set-ups, while the velocity dispersion shows a slightly higher central peak.

Thus, we find that that such IMBH-hosting simulations do not match the observed profiles of the MW NSC. This result is in agreement with the findings of Mastrobuono-Battisti et al. (2014) and may serve as an additional kinematic constraint for the existence of IMBHs in GCs and NSCs.

However, the low amount of rotation in the IMBH-hosting simulations may originate by the initial orbital distribution of the infalling GCs. These simulations are indeed not comparable to Simulations I and II described in *Chapter 4*. The net angular momentum of the infalling GCs in the IMBH-hosting simulations is zero, in contrast to Simulations I and II. Hence we do not conclude that IMBHs lower the observed rotation of NSCs as this may be an outcome of the different initial GC orbital distribution set-up between these two sets of simulations.

In future work we plan to investigate solely the effect of the existence of IMBHs in simulated NSCs, by comparing three sets of simulations (Simulation I, II and III, described in *Chapter 4*) with the presence and the lack of IMBHs in the infalling GCs.

We will study the behavior of the IMBHs in the central region of the NSC and investigate their dynamical imprints on the kinematics of the resulting NSCs. If IMBHs are long-lived in the central region of the NSC, they may act as massive pertubers and cause random scatterings to their surrounding stars, as shown by Mastrobuono-Battisti et al. (2014). We expect that these random scatterings may result into a lower velocity and a higher central velocity dispersion of the NSC, with potential observational implications. The results from new simulations will help us understand in more detail the dynamical effects of IMBHs, explore their observational consequences and set kinematic constraints for their existence in GCs, in the Milky Way NSC and/or extragalactic NSCs.

5.2.3 Unraveling the Link between Globular and Nuclear Star Clusters

In the near future, we plan to investigate further the connection between globular (GCs) and nuclear star clusters. As discussed in Section 4.1.1 and *Chapter 4*, NSCs may be the remnants of GC mergers, however they appear to share similar sizes with their progenitors and follow a similar mass-density relation as the typical Milky Way GCs (see Figure 4.1, Walcher et al. 2005), although NSCs in the centers of galaxies are more massive and compact.

There is very strong observational evidence of a connection between GCs and NSCs, as some observed massive globular cluster-like stellar systems may have evolved from NSCs. Such candidates are ω Cen (NGC 5139) and M54 (NGC 6715), two massive GC-like systems of our Milky Way, of masses between $2 - 5 \cdot 10^6\,M_\odot$ (Meylan et al. 1995; van de Ven et al. 2006; D'Souza & Rix 2013) and $1.5 - 2 \cdot 10^6\,M_\odot$ (Gnedin & Ostriker 1997; McLaughlin & van der Marel 2005), respectively.

Such systems have been for long suggested to be the stripped NSCs of dwarf galaxies, due to their high masses and their resemblance to NSCs in size, luminosity and possibly stellar populations, exhibiting a substantial internal iron abundance ([Fe/H]) spread (Georgiev et al. 2009; Johnson & Pilachowski 2010; Carretta et al. 2010), which is uncommon for globular clusters of lower mass.

One particular case of interest is M54, which appears to be part of the Sagittarius Stream, and probably located at the center of the Sagittarius dwarf spheroidal galaxy, in process of being disrupted by the tidal interaction with our Milky Way (Ibata et al. 1994) for at least 2.5-3.0 Gyr (Law et al. 2005).

M54 represents thus a key object to understand whether and how massive globular cluster-like systems such as this could be "naked" NSCs, that have been tidally stripped from their dwarf galaxy hosts. We expect that a much better understanding of the origin of M54 will become available thanks to its ongoing observational studies carried out with MUSE (e.g. Alfaro-Cuello et al. 2017, in preparation), but these need to be complemented with theoretical/simulations studies.

In the immediate future, we plan to rescale our simulated NSCs, as described in *Chapter 4*, to the mass of M54. Each NSC will be implemented into an orbit in a Milky Way-like potential on the estimated position of the Sagittarius dwarf 3 Gyr ago (e.g. Law et al. 2005) and evolved to the present-day conditions. The dynamical properties of the resulting stripped NSCs will then be compared to the aforementioned observations of M54 obtained from MUSE. This will allow to understand if the stripped-NSC scenario can reproduce the dynamical properties of M54.

These future findings will provide very important insights onto the dynamical nature of massive stellar clusters like M54, aiming to finally unveil their elusive connection to NSCs.

Globally, the findings presented in this thesis have shown how mergers can account for a variety of observed dynamical properties of nuclear star clusters, as well as early-type galaxies, and serve to set dynamical constraints on their formation origin. Open questions still remain, as many aspects regarding the intrinsic structure and origin of these systems seem to be far from a foregone conclusion. Now is the time for the new generation of high-quality integral-field spectroscopy instruments, in combination with the rapid progress of numerical simulations, to lead us to a very promising journey towards unraveling the physical processes that govern galaxy formation and evolution.

Appendix A

Triaxial Schwarzschild modeling

Here we present a more detailed description of the triaxial Schwarzschild dynamical modeling, and our preliminary results on the accuracy of this method to recover global parameters of early-type galaxies. In what follows, we use the mock observations described in *Chapter 2* to investigate in particular how the recovery of the dark matter distribution of an early-type galaxy depends on the spatial coverage of the stellar kinematics observations used in such dynamical models.

In the main formalism of the Triaxial Schwarzschild method, a galaxy's luminous potential is constructed by deprojecting the two-dimensional stellar surface brightness distribution of the galaxy into a triaxial mass density by assuming a mass-to-light ratio (M/L, here we assume to be constant with radius) and a set of three angles θ, ϕ, ψ (Euler angles), so that we have 1+3 parameters which are treated as free parameters in the models. The projected stellar distribution of the galaxy is parametrized using the Multi-Gaussian Expansion (MGE) model (Monnet et al. 1992; Emsellem et al. 1994), as implemented by Cappellari (2002), where the galaxy's stellar surface brightness distribution is fitted with a sum of 2D Gaussians, while allowing for position angle twists and ellipticity variations in the projected distribution. The projected mass distribution is then deprojected to a triaxial shape according to the three viewing angles θ, ϕ, ψ which depend on the intrinsic shape of the galaxy[1].

The method allows for the inclusion and determination of a central black hole and a dark matter halo. The dark matter halo distribution is assumed spherical with a Navarro-Frenk-White (NFW) profile (Navarro et al. 1996):

$$\rho(R) = \frac{\rho_s}{(R/R_s)(1 + R/R_s)^2} \tag{A.1}$$

where ρ_s the characteristic density and R_s the scale radius of the halo.

This translates to two free parameters in the Schwarzschild models, the dark matter fraction $f = M^{dm}_{200}/M^{*}_{200}$ and the concentration $c = R_{200}/R_s$ of the halo. M^{dm}_{200} and M^{*}_{200} are the dark matter and stellar mass of the galaxy, respectively, within a radius of R_{200}, corresponding to the radius where the

[1] See van den Bosch et al. (2008) for a more detailed description of the deprojection method.

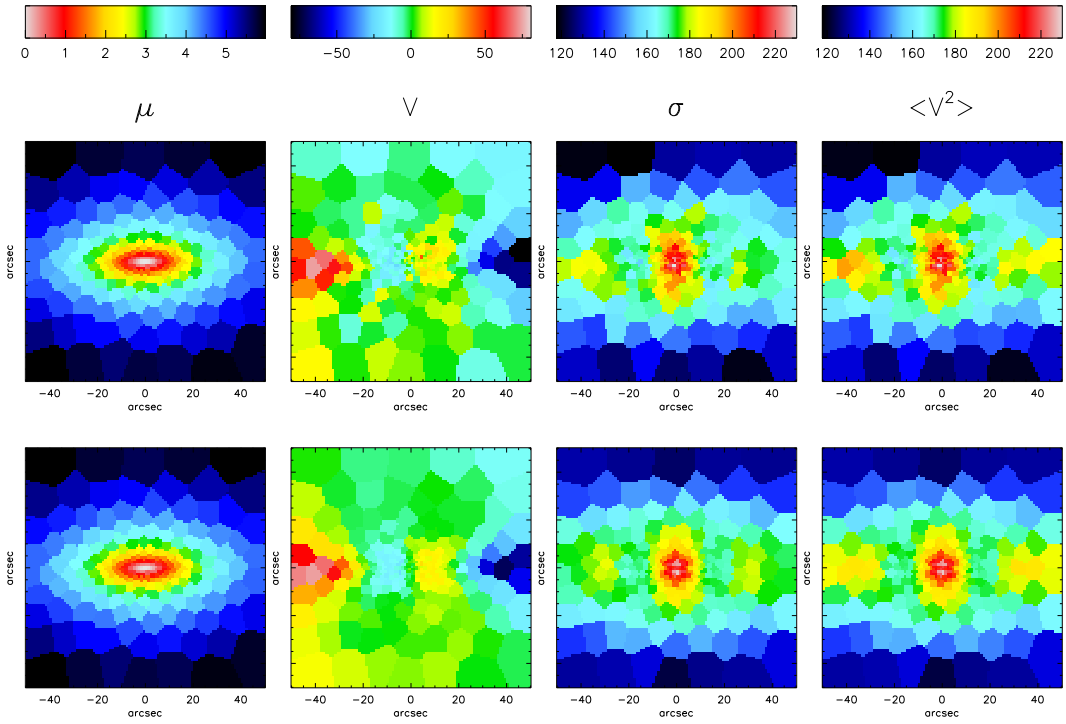

Figure A.1: Schwarzschild modeling of the simulated early-type galaxy described in Section 2.3.1. *From left to right*: Projected stellar surface brightness in $mag/arcsec^2$, line-of-sight velocity (V), velocity dispersion (σ) and second moment ($< V^2 >$) in km/s, for the stellar component of our simulated elliptical galaxy. *First row:* Mock data, *Second row:* Best fit model. The kinematics field-of-view extends out to 1 half-mass radius.

the density of the dark matter halo is 200 times the critical density of the Universe[2], ρ_{cr}.

The galaxies used in this work do not simulate the presence of black holes, hence these are also not parametrized in the models. This way the total potential of the galaxy includes contribution from the stellar and dark matter content of the galaxy.

Within this specified gravitational potential, orbits are integrated and an orbit library is generated. There are four different orbital families: three types of tube orbits and box orbits (see Section 1.1.2). From this orbit library, different orbital weights are found and given to orbits such that when they are super-imposed and projected to observables they fit the observed LOSVD, while their density matches the observed stellar density of the galaxy in each bin. The kinematic fitting is performed using the least-squares method. The stellar density is not fitted, but is used as a constraint in the fitting (the model should agree with the observed mass distribution with an accuracy of at least 2% in each bin, which is the typical accuracy of an MGE model). The reason for not fitting the mass is that it can always be reproduced up to a certain precision (van der Marel et al. 1998). The final output is a model with a 3D dynamical structure that fits best the observed LOS kinematics and stellar mass distribution in a least-squares sense.

[2]The critical density is given by $\rho_{cr}=3H^2/8\pi G$ and is the minimum density that ensures that the Universe could not expand forever, and will not collapse either. The value of ρ_{cr} depends on redshift and the Hubble constant, H.

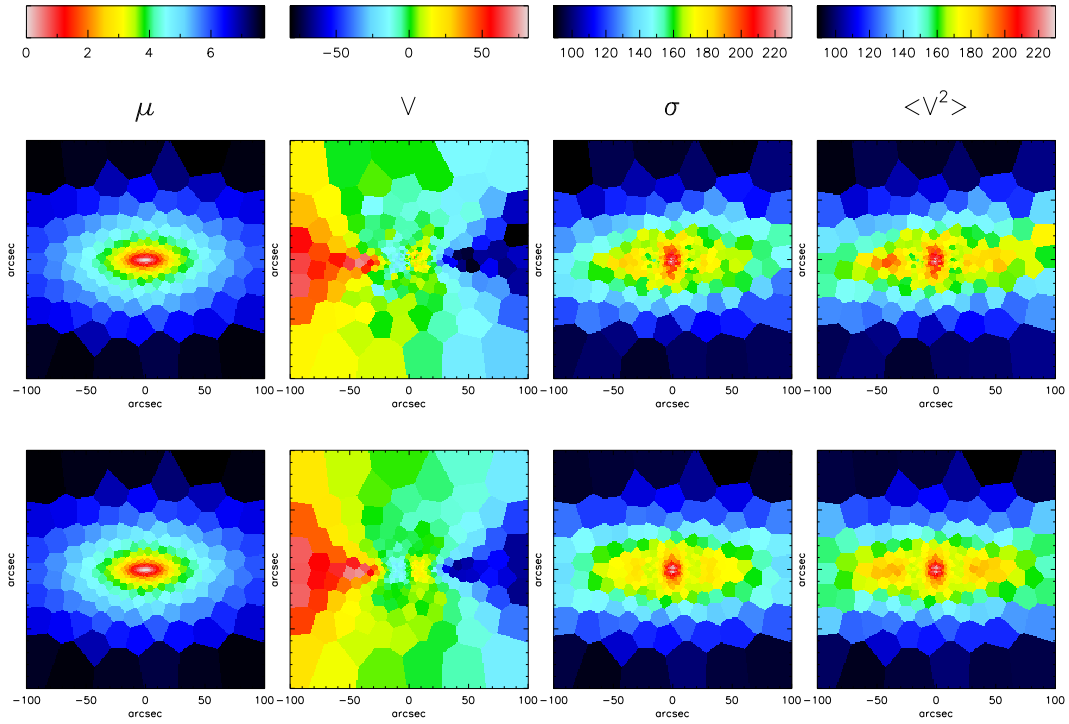

Figure A.2: Same as Figure A.1, but for an extended field-of view of 2 half-mass radii. *First row:* Mock data, *Second row:* Best fit model.

The used simulated elliptical galaxy and the extraction of its mock stellar kinematics is described in detail in Section 2.3.1 (Tsatsi et al. 2015). In order to construct dynamical models, we parametrize the galaxy's projected stellar mass distribution using the MGE model. The intrinsic shape of the remnant's 3D stellar particle distribution is parametrized using an iterative method to obtain the best fitting ellipsoid to the distribution and to extract the eigenvalues of the mass tensor inside this ellipsoid (Macciò et al. 2008). In this way we can estimate the three viewing angles θ, ϕ, ψ and use them as known parameters for the construction of our dynamical models.

The merger remnant's real dark matter halo is parametrized by fitting a spherical NFW profile (Navarro et al. 1996) described in Equation A.1. We find: R_{200}=176 kpc, $c_{real} = R_{200}/R_s = 7.0 \pm 0.2$, and $f_{real} = M^{dm}_{200}/M^{*}_{200} = 9.8 \pm 0.2$, where c_{real} we call the "real" concentration and f_{real} the "real" dark matter fraction of our galaxy.

We construct Triaxial Schwarzschild models for the simulated merger remnant with a 10×10 grid (100 models) of spherical NFW dark matter halo parameters (dark matter fraction f and concentration c), where the mass-to-light ratio and the viewing angles are kept constant and equal to the "real" values: we adopt a $M/L = 4\,M_{\odot}/L_{\odot}$, to construct the mock images and the viewing angles used as an input to deproject the mass distribution are known and kept fixed. Hence we keep all 1+3 parameters fixed to the "real" ones and the only free parameters of the models are the NFW parameters f and c. As a first test, we want to investigate if and how well the method can recover the dark matter

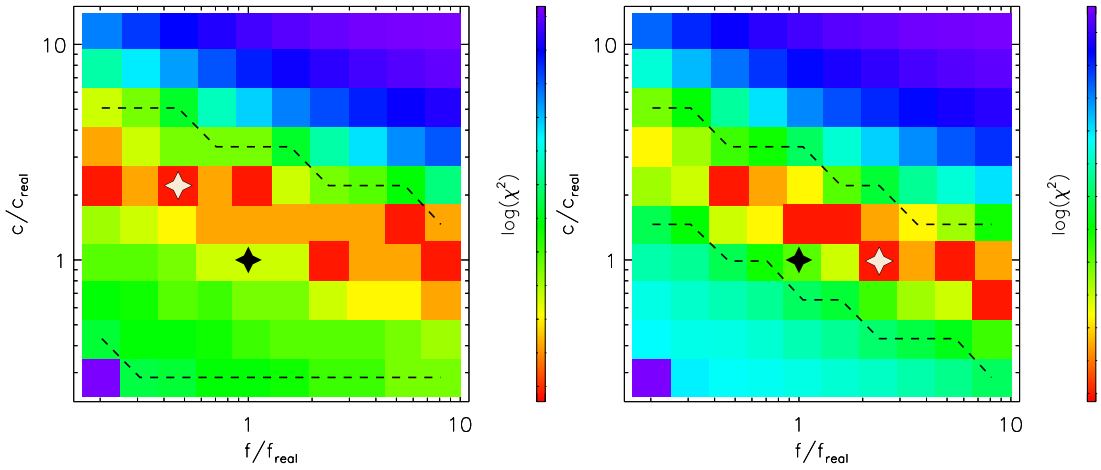

Figure A.3: Recovery of the dark matter distribution of the simulated galaxy: dark matter halo parameters c and f for every Schwarzschild model and their corresponding χ^2 after fitting with the mock kinematics. f_{real} and c_{real} correspond to the values retrieved from an NFW fitted independently to the simulated dark matter halo ("real model"). The white star shows the best-fit Schwarzschild model and the black star the "real model". The black dashed lines indicate the 1σ confidence level. Left: the kinematics field-of-view extends to 1 half-mass radius. Right: the field-of-view is 2 half mass radii.

distribution of the galaxy, and how the recovery depends on the size of the kinematics field of view that we use.

We use 2 different sizes for the LOS kinematics field of view, that extend respectively out to 1 and 2 r_h (half-mass radii) of the galaxy (10×10 kpc^2, 20×20 kpc^2 or 100×100 arcsec^2 and 200×200 arcsec^2).

Figure A.1 and Figure A.2 show the mock data (projected surface brightness μ, stellar line-of-sight velocity (V), velocity dispersion (σ) and second moment ($< V^2 >$) of the galaxy, in comparison with the ones retrieved from the best-fit Schwarzschild models for the two different sizes of the field of view. We see that the best-model matches relatively well the mock observations and can reproduce the observed kinematic peculiarities of this galaxy (e.g. the large-scale KDC in its center).

In order to see how well the models can reproduce the dark matter halo properties of the galaxy, we plot the concentration c and dark matter fraction f parameters used in each of the 100 models, as a function of the retrieved χ^2 after fitting (see Figure A.3).

The best-fitting model (minimum χ^2) is shown in Figure A.3, compared to the "real" model (the one that corresponds to the "real" values c_{real} and f_{real} found from fitting an NFW profile directly to the dark matter halo distribution of the galaxy). For our confidence limit we use the $\Delta\chi^2$ criterion below as a 1σ result (van den Bosch et al. 2008):

$$\Delta\chi^2 < \sqrt{2N_{obs}} \tag{A.2}$$

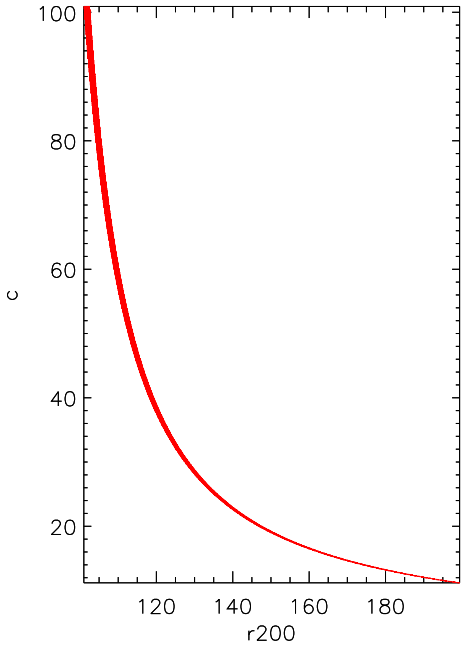

Figure A.4: Numerical solution of Equation A.4, showing the degeneracy between the dark matter concentration c and radius R_{200}, when fitting for the enclosed dark matter halo mass of an NFW profile.

where N_{obs} is the number of observables used in the fitting, which is the number of apertures (bins) multiplied by the number of Gauss–Hermite moments (two in our case, V and σ)[3].

Figure A.3 shows that the parameters c and f are degenerate. That is due to the fact that in the Schwarzschild models the dark matter halo distribution of the galaxy is fitted with an NFW profile, by using tracers that are constrained to a radius which is much less than the scale radius of the NFW profile, while the stellar mass of the galaxy is not fitted. In other words, our kinematics tracers can constrain the *enclosed* dark matter halo mass M_{enc} within the radius R_{enc} of our kinematics field of view. For M_{enc} the NFW profile yields:

$$M_{enc} = 4\pi\rho_o R_s^3 \left(ln(1 + R_{enc}/R_s) - \frac{R_{enc}/R_s}{1 + R_{enc}/R_s} \right) \tag{A.3}$$

where ρ_0 corresponds to the central density of the dark matter halo. The above equation becomes:

$$M_{200} = M_{enc} \frac{ln(1 + c) - \frac{1}{1+c}}{ln(1 + R_{enc}c/R_{200}) - \frac{cR_{enc}}{cR_{enc}+R_{200}}} \tag{A.4}$$

and since R_{enc} and M_{enc} are similar for all models and $M_{200} \propto R_{200}^3$, Equation A.4 yields a relation between R_{200} and c, or f and c, since $f = M_{200}/M_{200}^*$, and the enclosed stellar mass remains almost the same in all models. A numerical solution of Equation A.4 is shown in Figure A.4.

[3]We note here that this confidence limit of the models would be tighter with the inclusion of the higher-order moments h_3 and h_4.

Nevertheless, the models can recover the dark matter parameters c_{real} and f_{real} at least within 1σ for both sizes of the kinematics field-of-view (Figure A.3). Figure 5.1 shows the corresponding enclosed dark matter mass profiles as a function of radius for all the constructed models and the two kinematics field-of-view used.

These results show that the best fit model could lead to a misprediction of a factor of ~2 of the real enclosed dark matter mass of the galaxy, in the case where the kinematic constraints extend out to only 1 half-mass radius. The recovery of the enclosed dark matter mass is more accurate, however, in the case where the stellar kinematic tracers extend beyond 2 half-mass radii of the galaxy.

List of acronyms

BCG: Brightest Cluster Galaxy

B/T: Bulge-to-total ratio

CAHA: Calar Alto Observatory

CALIFA: Calar Alto Legacy Integral Field Area survey

CMO: Central massive object

CMZ: Central molecular zone

CRC: Counter-rotating Core (Component)

DR: Data Release

ETG: Early-type galaxy

FoV: Field-of-view

GC: Globular cluster

HST: Hubble Space Telescope

IFS: Integral-Field Spectroscopy

IFU: Integral-Field Unit

IMBH: Intermediate Mass Black Hole

IRAC: Infrared Array Camera (onboard Spitzer Space Telescope)

KDC: Kinematically Decoupled Core (Component)

LOS: Line-of-sight

LOSVD: Line-of-sight velocity distribution

LTG: Late-type galaxy

M/L: Mass-to-light ratio

MBH: Massive black hole

MGE: Multi-Gaussian Expansion

MaNGA: Mapping Nearby Galaxies at APO (Apache Point Observatory)

MUSE: Multi Unit Spectroscopic Explorer

MW: Milky Way

NB: Nuclear Bulge

NFW: Navarro-Frenk-White

NRR: Non regular rotator

NED: NASA extragalactic database

NGC: New general catalogue

NSC: Nuclear Star Cluster

PA: Position angle

PMAS: Potsdam Multi-Aperture Spectrograph

PPAK: PMAS fiber pack

RR: Regular rotator

SAURON: Spectrographic Areal Unit for Research on Optical Nebulae

SDSS: Sloan Digital Sky Survey

SIMBAD: Set of Identifications, Measurements, and Bibliography for Astronomical Data

SMBH: Supermassive black hole

SN: Signal-to-noise ratio

SPH: Smoothed Particle Hydrodynamics

Bibliography

Aarseth, S. J. & Binney, J. 1978, MNRAS, 185, 227

Abazajian, K. N., Adelman-McCarthy, J. K., Agüeros, M. A., et al. 2009, ApJS, 182, 543

Alfaro-Cuello, M. et al. 2017, in preparation

Amorisco, N. C., Evans, N. W., & van de Ven, G. 2014, Nature, 507, 335

Antonini, F., Capuzzo-Dolcetta, R., Mastrobuono-Battisti, A., & Merritt, D. 2012, ApJ, 750, 111

Arca-Sedda, M., Capuzzo-Dolcetta, R., Antonini, F., & Seth, A. 2015, ApJ, 806, 220

Arnold, J. A., Romanowsky, A. J., Brodie, J. P., et al. 2014, ApJ, 791, 80

Bacon, R., Accardo, M., Adjali, L., et al. 2010, in Proc. SPIE, Vol. 7735, Ground-based and Airborne Instrumentation for Astronomy III, 773508

Bacon, R., Copin, Y., Monnet, G., et al. 2001, MNRAS, 326, 23

Balcells, M. & Quinn, P. J. 1990, ApJ, 361, 381

Balick, B. & Brown, R. L. 1974, ApJ, 194, 265

Barnes, J. E. 1988, ApJ, 331, 699

Barnes, J. E. 1992, ApJ, 393, 484

Barnes, J. E. 2002, MNRAS, 333, 481

Barnes, J. E. 2016, MNRAS, 455, 1957

Barnes, J. E. & Hernquist, L. E. 1991, ApJL, 370, L65

Becklin, E. E. & Neugebauer, G. 1968, ApJ, 151, 145

Bell, E. F., Wolf, C., Meisenheimer, K., et al. 2004, ApJ, 608, 752

Bender, R. 1988, A&A, 202, L5

Bender, R., Doebereiner, S., & Moellenhoff, C. 1988, A&AS, 74, 385

Bendo, G. J. & Barnes, J. E. 2000, MNRAS, 316, 315

Bertola, F. & Galletta, G. 1978, ApJL, 226, L115

Bertola, F., Galletta, G., Capaccioli, M., & Rampazzo, R. 1988, A&A, 192, 24

Bianchini, P., Norris, M. A., van de Ven, G., & Schinnerer, E. 2015, MNRAS, 453, 365

Binggeli, B. & Jerjen, H. 1998, A&A, 333, 17

Binney, J. 1978, Comments on Astrophysics, 8, 27

Binney, J. 1985, MNRAS, 212, 767

Blum, R. D., Ramírez, S. V., Sellgren, K., & Olsen, K. 2003, ApJ, 597, 323

Boehle, A., Ghez, A. M., Schödel, R., et al. 2016, ApJ, 830, 17

Bois, M., Bournaud, F., Emsellem, E., et al. 2010, MNRAS, 406, 2405

Bois, M., Emsellem, E., Bournaud, F., et al. 2011, MNRAS, 416, 1654

Böker, T., Laine, S., van der Marel, R. P., et al. 2002, AJ, 123, 1389

Bundy, K., Bershady, M. A., Law, D. R., et al. 2015, ApJ, 798, 7

Burke, C. & Collins, C. A. 2013, MNRAS, 434, 2856

Caon, N., Capaccioli, M., & D'Onofrio, M. 1993, MNRAS, 265, 1013

Cappellari, M. 2002, MNRAS, 333, 400

Cappellari, M. 2013, ApJL, 778, L2

Cappellari, M. & Copin, Y. 2003, MNRAS, 342, 345

Cappellari, M., Emsellem, E., Bacon, R., et al. 2007, MNRAS, 379, 418

Cappellari, M., Emsellem, E., Krajnović, D., et al. 2011, MNRAS, 413, 813

Capuzzo-Dolcetta, R. 1993, ApJ, 415, 616

Carollo, C. M., Franx, M., Illingworth, G. D., & Forbes, D. A. 1997, ApJ, 481, 710

Carretta, E., Bragaglia, A., Gratton, R. G., et al. 2010, ApJL, 714, L7

Carter, D. 1979, MNRAS, 186

Carter, D., Thomson, R. C., & Hau, G. K. T. 1998, MNRAS, 294, 182

Cavaliere, A. & Fusco-Femiano, R. 1976, A&A, 49, 137

Chatzopoulos, S., Fritz, T. K., Gerhard, O., et al. 2015a, MNRAS, 447, 948

Chatzopoulos, S., Gerhard, O., Fritz, T. K., et al. 2015b, MNRAS, 453, 939

Cole, D. R., Debattista, V. P., Varri, A. L., Hartmann, M., & Seth, A. C. 2016, ArXiv e-prints

Contopoulos, G. 1956, ZAp, 39, 126

Côté, P., Piatek, S., Ferrarese, L., et al. 2006, ApJS, 165, 57

Cox, T. J., Dutta, S. N., Di Matteo, T., et al. 2006, ApJ, 650, 791

Crocker, A. F., Jeong, H., Komugi, S., et al. 2009, MNRAS, 393, 1255

Davies, R. L. & Birkinshaw, M. 1986, ApJL, 303, L45

Davies, R. L. & Birkinshaw, M. 1988, ApJS, 68, 409

Davies, R. L. & Illingworth, G. D. 1986, ApJ, 302, 234

Davies, R. L., Kuntschner, H., Emsellem, E., et al. 2001, ApJL, 548, L33

de Vaucouleurs, G. 1959, Handbuch der Physik, 53, 275

de Zeeuw, P. T., Bureau, M., Emsellem, E., et al. 2002, MNRAS, 329, 513

den Brok, M., Peletier, R. F., Seth, A., et al. 2014, MNRAS, 445, 2385

D'Eugenio, F., Houghton, R. C. W., Davies, R. L., & Dalla Bontà, E. 2013, MNRAS, 429, 1258

Do, T., Kerzendorf, W., Winsor, N., et al. 2015, ApJ, 809, 143

D'Onofrio, M., Capaccioli, M., & Caon, N. 1994, MNRAS, 271, 523

D'Souza, R. & Rix, H.-W. 2013, MNRAS, 429, 1887

Duc, P.-A., Cuillandre, J.-C., Karabal, E., et al. 2015, MNRAS, 446, 120

Ebrová, I. & Łokas, E. L. 2015, ApJ, 813, 10

Eckart, A. & Genzel, R. 1996, Nature, 383, 415

Efstathiou, G., Ellis, R. S., & Carter, D. 1982, MNRAS, 201, 975

Emsellem, E., Cappellari, M., Krajnović, D., et al. 2011, MNRAS, 414, 888

Emsellem, E., Cappellari, M., Krajnović, D., et al. 2007, MNRAS, 379, 401

Emsellem, E., Cappellari, M., Peletier, R. F., et al. 2004, MNRAS, 352, 721

Emsellem, E., Krajnović, D., & Sarzi, M. 2014, MNRAS, 445, L79

Emsellem, E., Monnet, G., & Bacon, R. 1994, A&A, 285, 723

Erwin, P. & Gadotti, D. A. 2012, Advances in Astronomy, 2012, 946368

Faber, S. M., Tremaine, S., Ajhar, E. A., et al. 1997, AJ, 114, 1771

Faber, S. M., Willmer, C. N. A., Wolf, C., et al. 2007, ApJ, 665, 265

Falcón-Barroso, J., Lyubenova, M., van de Ven, G., et al. 2016, ArXiv e-prints

Farrell, S. A., Webb, N. A., Barret, D., Godet, O., & Rodrigues, J. M. 2009, Nature, 460, 73

Fazio, G. G., Hora, J. L., Allen, L. E., et al. 2004, ApJS, 154, 10

Feldmeier, A., Neumayer, N., Seth, A., et al. 2014, A&A, 570, A2

Feldmeier-Krause, A., Neumayer, N., Schödel, R., et al. 2015, A&A, 584, A2

Ferrarese, L., Côté, P., Dalla Bontà, E., et al. 2006, ApJL, 644, L21

Ferrarese, L., van den Bosch, F. C., Ford, H. C., Jaffe, W., & O'Connell, R. W. 1994, AJ, 108, 1598

Finkelman, I., Moiseev, A., Brosch, N., & Katkov, I. 2011, MNRAS, 418, 1834

Fogarty, L. M. R., Scott, N., Owers, M. S., et al. 2014, MNRAS, 443, 485

Franx, M. & Illingworth, G. D. 1988, ApJL, 327, L55

Freitag, M., Gürkan, M. A., & Rasio, F. A. 2006, MNRAS, 368, 141

Fritz, T. K., Chatzopoulos, S., Gerhard, O., et al. 2016, ApJ, 821, 44

Genzel, R., Eckart, A., Ott, T., & Eisenhauer, F. 1997, MNRAS, 291, 219

Genzel, R., Eisenhauer, F., & Gillessen, S. 2010, Reviews of Modern Physics, 82, 3121

Georgiev, I. Y. & Böker, T. 2014, MNRAS, 441, 3570

Georgiev, I. Y., Hilker, M., Puzia, T. H., Goudfrooij, P., & Baumgardt, H. 2009, MNRAS, 396, 1075

Ghez, A. M., Morris, M., Becklin, E. E., Tanner, A., & Kremenek, T. 2000, Nature, 407, 349

Gillessen, S., Eisenhauer, F., Trippe, S., et al. 2009, ApJ, 692, 1075

Gnedin, O. Y. & Ostriker, J. P. 1997, ApJ, 474, 223

Gnedin, O. Y., Ostriker, J. P., & Tremaine, S. 2014, ApJ, 785, 71

Graham, A. W. 2012, MNRAS, 422, 1586

Graham, A. W. & Guzmán, R. 2003, AJ, 125, 2936

Graham, A. W., Spitler, L. R., Forbes, D. A., et al. 2012, ApJ, 750, 121

Gürkan, M. A., Freitag, M., & Rasio, F. A. 2004, ApJ, 604, 632

Hartmann, M., Debattista, V. P., Seth, A., Cappellari, M., & Quinn, T. R. 2011, MNRAS, 418, 2697

Hernquist, L. 1990, ApJ, 356, 359

Hernquist, L. & Barnes, J. E. 1991, Nature, 354, 210

Ho, N., Geha, M., Munoz, R. R., et al. 2012, ApJ, 758, 124

Hopkins, P. F., Cox, T. J., & Hernquist, L. 2008, ApJ, 689, 17

Houghton, R. C. W., Davies, R. L., D'Eugenio, F., et al. 2013, MNRAS, 436, 19

Hubble, E. P. 1927, The Observatory, 50, 276

Hubble, E. P. 1936, Realm of the Nebulae

Husemann, B., Jahnke, K., Sánchez, S. F., et al. 2013, A&A, 549, A87

Ibata, R. A., Gilmore, G., & Irwin, M. J. 1994, Nature, 370, 194

Jedrzejewski, R. & Schechter, P. L. 1989, AJ, 98, 147

Jedrzejewski, R. I. 1987a, MNRAS, 226, 747

Jedrzejewski, R. I. 1987b, in IAU Symposium, Vol. 127, Structure and Dynamics of Elliptical Galaxies, ed. P. T. de Zeeuw, 37–44

Johnson, C. I. & Pilachowski, C. A. 2010, ApJ, 722, 1373

Katkov, I. Y., Sil'chenko, O. K., & Afanasiev, V. L. 2014, MNRAS, 438, 2798

Kelz, A., Verheijen, M. A. W., Roth, M. M., et al. 2006, PASP, 118, 129

Khochfar, S. & Burkert, A. 2005, MNRAS, 359, 1379

Khochfar, S. & Burkert, A. 2006a, A&A, 445, 403

Khochfar, S. & Burkert, A. 2006b, A&A, 445, 403

King, I. R. 1966, AJ, 71, 64

King, I. R. 1978, ApJ, 222, 1

Kormendy, J. & Ho, L. C. 2013, ARAA, 51, 511

Krajnović, D., Bacon, R., Cappellari, M., et al. 2008, MNRAS, 390, 93

Krajnović, D., Cappellari, M., de Zeeuw, P. T., & Copin, Y. 2006, MNRAS, 366, 787

Krajnović, D., Cappellari, M., Emsellem, E., McDermid, R. M., & de Zeeuw, P. T. 2005, MNRAS, 357, 1113

Krajnović, D., Emsellem, E., Cappellari, M., et al. 2011, MNRAS, 414, 2923

Kuntschner, H., Emsellem, E., Bacon, R., et al. 2010, MNRAS, 408, 97

Larson, R. B. 1974, MNRAS, 166, 585

Lauer, T. R., Ajhar, E. A., Byun, Y.-I., et al. 1995, AJ, 110, 2622

Launhardt, R., Zylka, R., & Mezger, P. G. 2002, A&A, 384, 112

Law, D. R., Johnston, K. V., & Majewski, S. R. 2005, ApJ, 619, 807

Łokas, E. L., Ebrová, I., Pino, A. d., & Semczuk, M. 2014, MNRAS, 445, L6

Loose, H. H., Kruegel, E., & Tutukov, A. 1982, A&A, 105, 342

Lyubenova, M., van den Bosch, R. C. E., Côté, P., et al. 2013, MNRAS, 431, 3364

Macciò, A. V., Dutton, A. A., & van den Bosch, F. C. 2008, MNRAS, 391, 1940

Madau, P. & Rees, M. J. 2001, ApJL, 551, L27

Mastrobuono-Battisti, A. & Perets, H. B. 2013, ApJ, 779, 85

Mastrobuono-Battisti, A., Perets, H. B., & Loeb, A. 2014, ApJ, 796, 40

McDermid, R. M., Emsellem, E., Shapiro, K. L., et al. 2006, MNRAS, 373, 906

McLaughlin, D. E. & van der Marel, R. P. 2005, ApJS, 161, 304

Merritt, D. & de Zeeuw, T. 1983, ApJL, 267, L19

Mestschersky, J. 1902, Astronomische Nachrichten, 159, 229

Meylan, G., Mayor, M., Duquennoy, A., & Dubath, P. 1995, A&A, 303, 761

Milosavljević, M. 2004, ApJL, 605, L13

Milosavljević, M. & Merritt, D. 2001, ApJ, 563, 34

Moellenhoff, C. & Bender, R. 1989, A&A, 214, 61

Moellenhoff, C. & Marenbach, G. 1986, A&A, 154, 219

Monnet, G., Bacon, R., & Emsellem, E. 1992, A&A, 253, 366

Moster, B. P., Macciò, A. V., Somerville, R. S., Naab, T., & Cox, T. J. 2011, MNRAS, 415, 3750

Naab, T. & Burkert, A. 2003, ApJ, 597, 893

Naab, T., Burkert, A., & Hernquist, L. 1999, ApJL, 523, L133

Naab, T., Oser, L., Emsellem, E., et al. 2014, MNRAS, 444, 3357

Navarro, J. F., Frenk, C. S., & White, S. D. M. 1996, ApJ, 462, 563

Nguyen, D. D., Seth, A. C., Reines, A. E., et al. 2014, ApJ, 794, 34

Norris, M. A., Van de Ven, G., Schinnerer, E., et al. 2016, ArXiv e-prints

Partridge, R. B. & Peebles, P. J. E. 1967, ApJ, 147, 868

Paumard, T., Genzel, R., Martins, F., et al. 2006, ApJ, 643, 1011

Perets, H. B. & Mastrobuono-Battisti, A. 2014, ApJL, 784, L44

Pérez, E., Cid Fernandes, R., González Delgado, R. M., et al. 2013, ApJL, 764, L1

Pfuhl, O., Fritz, T. K., Zilka, M., et al. 2011, ApJ, 741, 108

Price, D. J. 2007, PASA, 24, 159

Querejeta, M., Eliche-Moral, M. C., Tapia, T., et al. 2015, A&A, 579, L2

Rix, H.-W. & White, S. D. M. 1990, ApJ, 362, 52

Rossa, J., van der Marel, R. P., Böker, T., et al. 2006, AJ, 132, 1074

Roth, M. M., Kelz, A., Fechner, T., et al. 2005, PASP, 117, 620

Rubin, V. C., Graham, J. A., & Kenney, J. D. P. 1992, ApJL, 394, L9

Ryden, B. S., Terndrup, D. M., Pogge, R. W., & Lauer, T. R. 1999, ApJ, 517, 650

Sánchez, S. F., García-Benito, R., Zibetti, S., et al. 2016, ArXiv e-prints

Sánchez, S. F., Kennicutt, R. C., Gil de Paz, A., et al. 2012, A&A, 538, A8

Sandage, A. 1961, The Hubble atlas of galaxies

Schechter, P. L. & Gunn, J. E. 1979, ApJ, 229, 472

Schinnerer, E., Böker, T., Meier, D. S., & Calzetti, D. 2008, ApJL, 684, L21

Schödel, R., Feldmeier, A., Kunneriath, D., et al. 2014, A&A, 566, A47

Schwarzschild, M. 1979, ApJ, 232, 236

Scott, N., Davies, R. L., Houghton, R. C. W., et al. 2014, MNRAS, 441, 274

Scott, N. & Graham, A. W. 2013, ApJ, 763, 76

Sersic, J. L. 1968, Atlas de galaxias australes

Seth, A. C., Blum, R. D., Bastian, N., Caldwell, N., & Debattista, V. P. 2008, ApJ, 687, 997

Seth, A. C., Cappellari, M., Neumayer, N., et al. 2010, ApJ, 714, 713

Seth, A. C., Dalcanton, J. J., Hodge, P. W., & Debattista, V. P. 2006, AJ, 132, 2539

Springel, V. 2005, MNRAS, 364, 1105

Statler, T. S. 1987, ApJ, 321, 113

Toloba, E., Guhathakurta, P., van de Ven, G., et al. 2014, ApJ, 783, 120

Toomre, A. 1977, in Evolution of Galaxies and Stellar Populations, ed. B. M. Tinsley & R. B. G. Larson, D. Campbell, 401

Toomre, A. & Toomre, J. 1972, ApJ, 178, 623

Tremaine, S. D., Ostriker, J. P., & Spitzer, Jr., L. 1975, ApJ, 196, 407

Trujillo, I., Graham, A. W., & Caon, N. 2001, MNRAS, 326, 869

Tsatsi, A., Lyubenova, M., van de Ven, G., et al. 2016b, to be submitted

Tsatsi, A., Macciò, A. V., van de Ven, G., & Moster, B. P. 2015, ApJL, 802, L3

Tsatsi, A., Mastrobuono-Battisti, A., van de Ven, G., et al. 2016, ArXiv e-prints: 1610.01162, MNRAS in press

Turner, M. L., Côté, P., Ferrarese, L., et al. 2012, ApJS, 203, 5

Valdes, F., Gupta, R., Rose, J. A., Singh, H. P., & Bell, D. J. 2004, ApJS, 152, 251

van de Ven, G., de Zeeuw, P. T., & van den Bosch, R. C. E. 2008, MNRAS, 385, 614

van de Ven, G., van den Bosch, R. C. E., Verolme, E. K., & de Zeeuw, P. T. 2006, A&A, 445, 513

van den Bosch, R. C. E. & van de Ven, G. 2009, MNRAS, 398, 1117

van den Bosch, R. C. E., van de Ven, G., Verolme, E. K., Cappellari, M., & de Zeeuw, P. T. 2008, MNRAS, 385, 647

van der Marel, R. P., Cretton, N., de Zeeuw, P. T., & Rix, H.-W. 1998, ApJ, 493, 613

van der Marel, R. P. & Franx, M. 1993, ApJ, 407, 525

van der Marel, R. P., Rossa, J., Walcher, C. J., et al. 2007, in IAU Symposium, Vol. 241, Stellar Populations as Building Blocks of Galaxies, ed. A. Vazdekis & R. Peletier, 475–479

van der Wel, A., Franx, M., van Dokkum, P. G., et al. 2014, ApJ, 788, 28

van Dokkum, P. G., Franx, M., Kriek, M., et al. 2008, ApJL, 677, L5

van Dokkum, P. G., Whitaker, K. E., Brammer, G., et al. 2010, ApJ, 709, 1018

Verheijen, M. A. W., Bershady, M. A., Andersen, D. R., et al. 2004, Astronomische Nachrichten, 325, 151

Verolme, E. K., Cappellari, M., Copin, Y., et al. 2002, MNRAS, 335, 517

Wagner, S. J., Bender, R., & Moellenhoff, C. 1988, A&A, 195, L5

Walcher, C. J., Böker, T., Charlot, S., et al. 2006, ApJ, 649, 692

Walcher, C. J., van der Marel, R. P., McLaughlin, D., et al. 2005, ApJ, 618, 237

Walcher, C. J., Wisotzki, L., Bekeraité, S., et al. 2014, A&A, 569, A1

Walsh, J. L., van den Bosch, R. C. E., Barth, A. J., & Sarzi, M. 2012, ApJ, 753, 79

Wehner, E. H. & Harris, W. E. 2006, ApJL, 644, L17

Weijmans, A.-M., Cappellari, M., Bacon, R., et al. 2009, MNRAS, 398, 561

Wenger, M., Ochsenbein, F., Egret, D., et al. 2000, A&AS, 143, 9

Zirm, A. W., van der Wel, A., Franx, M., et al. 2007, ApJ, 656, 66

Acknowledgements

I would like to express my most sincere gratitude to my main supervisor, Glenn van de Ven, for all his support throughout these 4 years of my graduate studies. The work presented here would not have been possible without his brilliant scientific advice and guidance, his motivation and enthusiasm, but most importantly, without the moral support and encouragement he provided me. Thanks for keeping an eye on me and making sure that I always felt happy! I will always be grateful for that.

This thesis would not have been possible without major contributions and support of Alessandra Mastrobuono-Battisti, Anna Sippel and Mariya Lyubenova. Alessandra, thank you for introducing me to the amazing world of nuclear star clusters, and for being such an amazing person to work with. Anna and Alessandra, thank you both for your thorough review and excellent suggestions for improvement of this thesis, your guidance, and your efforts to lighten the period of my thesis writing. Mariya, thank you for your generous help and contribution to the work presented here, for being always so brilliant, always available and for all your help and support during the last 4 years. Most importantly, I thank you all for being so immensely smart and also kind at the same time!

I would also like to express my warm appreciation to many other people I have worked with during the last few years and contributed significantly to the work presented here. I am very thankful to my second advisor, Andrea Macciò, for his great scientific advice, guidance and support, for introducing me to various aspects of galaxy formation and helped me understand it in a deeper level. I am also thankful to Jiang Chang, for his contribution and help regarding the simulations presented in this work.

I am very grateful to Paolo Bianchini, for his contribution to my work, and for all his help and support throughout the 4 years of my PhD. It goes without saying that I could not have imagined a better place to work at than the Office 217 at MPIA. I owe a very special thanks to Hector Hiss, Hans Baehr, Sven Buder and Tobias Buck, for their support and their very important contributions for improvement of this thesis.

I am deeply thankful to Nadine Neumayer, Arjen van der Wel, Michael Maseda, as well as the CALIFA team and in particular Jesús Falcón-Barroso and Alfonso Aguerri, for the very useful comments they provided me for the work presented here. Special thanks to Marie Martig, for our very important discussions.

I am very grateful to Hubert Klahr, for his kind acceptance to review this thesis, as well as the two examiners of my PhD examination committee, Eva Grebel and Andre Schöning.

Last but not least, I am most deeply grateful to my family, for their endless love and support.

I acknowledge financial support from the DAGAL network from the People Programme (Marie Curie Actions) of the European Union's Seventh Framework Programme FP7/2007- 2013/ under REA grant agreement number PITN-GA-2011-289313.
I acknowledge support from the International Max-Planck Research School for Astronomy and Cosmic Physics at the University of Heidelberg (IMPRS-HD).
This research has made use of the NASA/IPAC Extragalactic Database (NED), which is operated by the Jet Propulsion Laboratory, California Institute of Technology, under contract with the National Aeronautics and Space Administration. This research has made use of the SIMBAD database, operated at CDS, Strasbourg, France, (Wenger et al. 2000). This research has made use of public SDSS data. Funding for the Sloan Digital Sky Survey IV has been provided by the Alfred P. Sloan Foundation, the U.S. Department of Energy Office of Science, and the Participating Institutions. SDSS-IV acknowledges support and resources from the Center for High-Performance Computing at the University of Utah. The SDSS web site is www.sdss.org. SDSS-IV is managed by the Astrophysical Research Consortium for the Participating Institutions of the SDSS Collaboration including the Brazilian Participation Group, the Carnegie Institution for Science, Carnegie Mellon University, the Chilean Participation Group, the French Participation Group, Harvard-Smithsonian Center for Astrophysics, Instituto de Astrofísica de Canarias, The Johns Hopkins University, Kavli Institute for the Physics and Mathematics of the Universe (IPMU) / University of Tokyo, Lawrence Berkeley National Laboratory, Leibniz Institut für Astrophysik Potsdam (AIP), Max-Planck-Institut für Astronomie (MPIA Heidelberg), Max-Planck-Institut für Astrophysik (MPA Garching), Max-Planck-Institut für Extraterrestrische Physik (MPE), National Astronomical Observatory of China, New Mexico State University, New York University, University of Notre Dame, Observatário Nacional / MCTI, The Ohio State University, Pennsylvania State University, Shanghai Astronomical Observatory, United Kingdom Participation Group, Universidad Nacional Autónoma de México, University of Arizona, University of Colorado Boulder, University of Oxford, University of Portsmouth, University of Utah, University of Virginia, University of Washington, University of Wisconsin, Vanderbilt University, and Yale University.

Άιντε εκεί μακρυά,
μακρυά στην Ανδρομέδα,
άιντε πίνουν τσίπουρο
και τρων λακέρδα.

Ah there far away,
far in Andromeda,
they drink tsipouro
and eat lakerda.[4]

[4] *Thanasis Papakonstantinou, "Andromeda"*